HOKKAIDO UNIVERSITY

Title	Effect of moisture and wheel loads on resilient modulus and permanent strain of road subgrade in cold regions
Author(s)	REN, Daoju
Degree Grantor	北海道大学
Degree Name	博士(工学)
Dissertation Number	甲第16045号
Issue Date	2024-06-28
DOI	https://doi.org/10.14943/doctoral.k16045
Doc URL	https://hdl.handle.net/2115/92762
Type	doctoral thesis
File Information	Ren_Daoju.pdf

Hokkaido University Collection of Scholarly and Academic Papers : HUSCAP

Effect of moisture and wheel loads on resilient modulus and permanent strain of road subgrade in cold regions

寒冷地における水分及び輪荷重が道路路床のレジリエントモジュラス及び永久ひずみに及ぼす影響

By

Daoju REN

A thesis submitted in partial fulfilment of the requirements for the degree of Doctor of Philosophy in Engineering

under the guidance and supervision of

Professor Tatsuya ISHIKAWA

Examined by the Doctoral Committee

Professor Tatsuya ISHIKAWA
Professor Satoshi NISHIMURA
Professor Satoru KAWASAKI

May 2024

Laboratory of Analytical Geomechanics
Division of Field Engineering for the Environment
Graduate School of Engineering
Hokkaido University
Sapporo, Hokkaido, Japan

ABSTRACT

Asphalt pavements, typically consisting of the asphalt layer, base course, and subgrade, endure cyclic loads from traffic, which generally leads to fatigue cracking and rutting damage, particularly affecting unbound granular materials. The current Japanese pavement design guide has some limitations such as the exclusion of moisture and freeze-thaw effects, the effect of stress state on elastic moduli, the behavior of rutting over time, the application of traffic loading, rate-hardening, the contribution of the non-subgrade layers to rutting, and principal stress axis rotation (PSAR), etc. To overcome these shortcomings, this study incorporated the concept of resilient modulus (M_r) and the rutting failure model of the Mechanistic-Empirical Pavement Design Guide (MEPDG) based on the previous study and further investigated the dynamic mechanical properties of unbound pavement materials such as subgrade soil and base course.

Resilient modulus (M_r) is a fundamental mechanical property vital for assessing the resistance of pavement structures to cyclic vertical loads. It has played a pivotal role in pavement design and has been instrumental in predicting pavement responses and fatigue life. The M_r of subgrade soil is affected by a multitude of factors, including stress, moisture, and temperature conditions, all of which interact to define the response of the soil. This study investigated the effect of complex climatic conditions on M_r with a particular focus on areas experiencing significant seasonal changes in snowy cold regions like Hokkaido, Japan. Previous studies have proposed predictive models for M_r, incorporating the concept of matric suction, to account for moisture conditions. However, these models have rarely considered hysteresis phenomena in the soil-water characteristic curve (SWCC) or the effects of wheel loading during different seasons. In this study, a series of M_r tests were conducted on two types of subgrade soil under various climatic and wheel loading conditions. The test results promise to enhance our understanding of the complex interplay of climatic and stress conditions on M_r of subgrade soil under suction hysteresis, particularly in regions with significant seasonal variations. Furthermore, three modified semi-empirical M_r predictive models incorporating Bishop's effective stress are combined with three χ estimation models and compared to find the appropriate determination method for χ and discuss their applicability to the wetting path of the SWCC.

On the other hand, cyclic axial loads generated by the traffic significantly affect the deformation characteristics of the base and subgrade materials, which becomes an important factor for the rutting damage of the pavement structure. For a fixed point in the pavement structure, the direction of stress constantly changes during the movement of the wheel load, defined as principal stress axis rotation (PSAR), which also affects the deformation of the pavement structure. Mechanistic-Empirical Pavement Design Guide (MEPDG) proposed a model that combines resilient and permanent deformations to predict the rut depth of unbound granular materials. However, there are some disputes about whether the effect of PSAR has been considered. This study examined the behavior and relation of the resilient strain and permanent strain of crusher-run gravels under the effect of PSAR by multi-ring shear tests and further verified the validity and reliability of the MEPDG permanent axial deformation predictive model.

In this study, the contents are mainly divided into two parts: the estimation of resilient modulus and the estimation of permanent strain. Chapter 1 introduces the background, literature review, objective, and organization of this study. Chapter 2 gives the details of the test apparatus used in this study, including water retention test apparatus and unsaturated freeze-thaw triaxial apparatus. Chapter 3 describes the test materials and test methods used in the water retention tests and resilient modulus tests under different climatic and stress conditions. Chapter 4 shows the results of resilient modulus tests under various test conditions and discusses the effects of complex climatic and wheel loading conditions on M_r. Chapter 5 verifies and compares the applicability of suction stress-based M_r predictive models by combining different χ estimation models. Chapter 6 proposes a modified permanent axial strain predictive model with consideration of the effect of PSAR based on the MEPDG rut depth predictive model to estimate the rutting damage more precisely. Chapter 7 summarizes the findings obtained in this study and the possible assignments in the future.

< This dissertation is a modified and revised form of the following original journals and proceedings>

1. Ren, D., Ishikawa, T., Si, J., Tokoro, T.: Effect of complex climatic and wheel load conditions on resilient modulus of unsaturated subgrade soil. *Transportation Geotechnics*, 45(3):101186 (2024). (DOI: 10.1016/j.trgeo.2024.101186)

2. Si, J., Ishikawa, T., Ren, D., Maruyama, K., Ueno, C.: Response prediction of asphalt pavement in cold region with thermo-hydro-mechanical coupling simulation. *Sustainability*, 15(18):13614 (2023). (DOI: 10.3390/su151813614)

3. Ren, D., Ishikawa, T., Tokoro, T.: Effect of principal stress axis rotation on resilient and permanent axial strains of unbound aggregate materials. *The 9th International Symposium on Environmental Vibration and Transportation Geodynamics*, 2024, Mar. 6-8, Sapporo, Japan.

4. Ren, D., Ishikawa, T., Tokoro, T.: A modified predictive model for resilient modulus of unsaturated subgrade soil with consideration of hysteresis. *The XIV Congress of the International Association for Engineering Geology and the Environment*, 2023, Sep. 21-27, Chengdu, China.

5. Ren, D., Ishikawa, T., Si, J., Tokoro, T.: Effect of hysteresis of SWCC on resilient modulus of subgrade soil under different climatic and stress conditions. *Transportation Research Board 102nd Annual Meeting*, 2023, Jan. 8-12, Washington D.C., USA.

6. Ren, D., Ishikawa, T., Tokoro, T.: Resilient and permanent axial strain of crusher-run materials under the effect of principal stress axes rotation. *57th Japan National Conference on Geotechnical Engineering*, 2022, Jul. 20-23, Niigata, Japan.

ACKNOWLEDGEMENT

I would like to express my deepest gratitude to everyone who has contributed to the completion of this doctoral dissertation. It has been a journey filled with challenges and growth, and I am immensely thankful for the support and guidance I have received along the way.

First and foremost, I extend my heartfelt appreciation to my supervisor, Prof. Tatsuya Ishikawa. His support, guidance, and encouragement have been playing a vital role throughout this research process. His expertise in the field of transportation geotechnics and rigorous attitude to academia have not only shaped this dissertation but have also inspired me to strive for excellence in my academic pursuits.

Special acknowledgment is due to Prof. (Assoc.) Tetsuya Tokoro for generously assisting me in adjusting the test apparatus. His expertise and assistance were invaluable in conducting the experiments essential to this dissertation. His willingness to share knowledge and resources reflects the collaborative spirit of academia.

I am also indebted to my lab mates Dr. Tianshu Lin, Dr. Shoulong Zhang, Dr. Junling Si, Mr. Abhay Kumar, and Mr. Namit Jain for their friendship, collaboration, and valuable insights. The mutually supportive environment in our lab has helped me with my research progress and enriched my research experience immeasurably.

I would like to express my special gratitude to Prof. Satoshi Nishimura for graciously renting me his test apparatus and for inspiring me with his innovative approach to developing test programs and apparatus. His generosity and insights have significantly contributed to the success of this research.

This research was made possible through the financial support of JST SPRING, Grant Number JPMJSP2119.

Finally, I extend my profound gratitude to my parents for their unwavering love, encouragement, and sacrifices. Their endless support has been the cornerstone of my academic journey, and I am forever grateful for their belief in me.

TABLE OF CONTENTS

ABSTRACT I
ACKNOWLEDGEMENT IV
TABLE OF CONTENTS V
LIST OF FIGURES VII
LIST OF TABLES X
1 INTRODUCTION 1
1.1 Background 1
1.2 Literature Review 5
1.2.1 M_r predictive models 5
1.2.2 Rutting failure models 8
1.3 Thesis Objectives 10
1.4 Thesis Organization 11
2 TEST APPARATUS 13
2.1 Water Retention Test Apparatus 13
2.2 Unsaturated Freeze-Thaw Triaxial Apparatus 14
3 TEST MATERIALS AND METHODS 20
3.1 Test Materials 20
3.2 Water Retention Test 22
3.2.1 Test sequence 22
3.2.2 SWCC under suction hysteresis 23
3.3 Resilient Modulus Test 24
3.3.1 Test sequence 24
3.3.2 Cyclic loading condition 25
3.3.3 Moisture condition 27
3.3.4 Wheel loading condition 28
3.3.5 Temperature condition 30
4 EFFECTS OF CLIMATIC AND WHEEL LOADING CONDITIONS ON RESILIENT MODULUS 32
4.1 Results of Resilient Modulus Tests 32
4.2 Effect of Matric Suction 37
4.3 Effect of Wheel Load 38
4.3.1 Effect of wheel load on moisture change 38

4.3.2 Effect of wheel load on resilient modulus 40
4.4 Effect of Freeze-thaw 42
4.4.1 Effect of freeze-thaw on moisture change and frost heave 42
4.4.2 Effect of freeze-thaw on resilient modulus 44
4.5 Effect of Combinations of Wheel Load and Freeze-thaw 46
4.5.1 Effect of wheel load after freeze-thaw 46
4.5.2 Effect of wheel load during frozen season 47
4.6 Summary 48
5 EFFECTS OF SUCTION STRESS ON RESILIENT MODULUS 51
5.1 Effect of Suction Hysteresis of SWCC 51
5.2 Determination of Bishop's Effective Stress Factor 52
5.2.1 Vanapalli model 52
5.2.2 Karube model 54
5.2.3 Khalili & Khabbaz (K&K) model 55
5.3 Proposal of Suction Stress Combined M_r Predictive Model 57
5.4 Applicability and Comparison of M_r Predictive Models 58
5.5 Summary 66
6 EFFECTS OF PRINCIPAL STRESS AXIS ROTATION ON PERMANENT STRAIN 68
6.1 Materials and Method 68
6.2 Test Results and Discussions 72
6.2.1 Resilient strain under PSAR 72
6.2.2 Permanent strain under PSAR 76
6.2.3 Relation between resilient and permanent strains 79
6.3 Summary 85
7 FINDINGS AND ASSIGNMENTS 86
7.1 Findings 86
7.2 Future Assignments 89
LIST OF REFERENCES 90
LIST OF NOTATIONS 96

LIST OF FIGURES

Figure 1-1 Pavement suffering: (a) fatigue cracking; (b) rutting 2

Figure 1-2 Three-layer model for allowable loading number calculation 2

Figure 1-3 Sequence in modified Japanese flexible pavement design guide (Lin et al. 2021) 4

Figure 1-4 Schematic diagram of the definition of M_r 6

Figure 1-5 Flow chart of this study 12

Figure 2-1 Water retention test apparatus by continuous pressurization method 14

Figure 2-2 Unsaturated freeze-thaw cyclic loading triaxial test apparatus: (a) Schematic diagram of test apparatus; (b) Structural design of specimen cap; (c) Structural design of specimen pedestal 16

Figure 2-3 Installation of PTFE and Versapor membrane filters: (a) Specimen cap; (b) Specimen pedestal 18

Figure 2-4 Measurement of AEV of Versapor membrane filter 18

Figure 3-1 Photos of test materials: (a) Toyoura sand; (b) Tomakomai soil 21

Figure 3-2 Grain size distribution curves of Toyoura sand and Tomakomai soil 22

Figure 3-3 Conceptual diagram of air pressurization types: (a) Triangle loading; (b) Trapezoid loading 23

Figure 3-4 SWCC of test materials: (a) Toyoura sand; (b) Tomakomai soil 24

Figure 3-5 Loading waves in one cycle: (a) This study; (b) AASHTO standard 26

Figure 3-6 Pavement structure and wheel loading condition 29

Figure 3-7 Temperature change in the freeze-thaw process 30

Figure 3-8 Copper pipe used during the wheel loading process in the FWT test 31

Figure 4-1 Results of U tests: (a) Toyoura sand; (b) Tomakomai soil 33

Figure 4-2 Results of UW tests: (a) Toyoura sand; (b) Tomakomai soil 34

Figure 4-3 Results of FT tests: (a) Toyoura sand; (b) Tomakomai soil 35

Figure 4-4 Results of FTW tests: (a) Toyoura sand; (b) Tomakomai soil 36

Figure 4-5 Results of FWT tests: (a) Toyoura sand; (b) Tomakomai soil 37

Figure 4-6 Water drainage during the wheel loading process (UW test) 39

Figure 4-7 Resilient modulus ratio of UW/U tests 41

Figure 4-8 Water drainage and frost heave during the freeze-thaw process (FT test): (a) Toyoura sand; (b) Tomakomai soil 43

Figure 4-9 Resilient modulus ratio of FT/U tests 46

Figure 4-10 Resilient modulus ratio: (a) FTW/U tests; (b) FTW/UW tests 47

Figure 4-11 Resilient modulus ratio of FWT/FT tests 48

Figure 5-1 Variation of χ and σ_s with the S_r using the Vanapalli model: (a) Toyoura sand; (b) Tomakomai soil 54

Figure 5-2 Variation of χ and σ_s with the S_r using the Karube model: (a) Toyoura sand; (b) Tomakomai soil 55

Figure 5-3 Variation of χ and σ_s with the S_r using the Khalili & Khabbaz model: (a) Toyoura sand; (b) Tomakomai soil 56

Figure 5-4 Comparison between tested and fitted M_r by different combinations with the modified MEPDG model: (a) Vanapalli model; (b) Karube model; (c) K&K model 60

Figure 5-5 Comparison between tested and fitted M_r by different combinations with the Heath model with: (a) Vanapalli model; (b) Karube model; (c) K&K model..... 60

Figure 5-6 Comparison between tested and fitted M_r by different combinations with the modified Ng model: (a) Vanapalli model; (b) Karube model; (c) K&K model 61

Figure 5-7 R-square values by different combinations of models: (a) Toyoura sand; (b) Tomakomai soil 64

Figure 5-8 MSE values by different combinations of models: (a) Toyoura sand; (b) Tomakomai soil 65

Figure 6-1 Schematic diagram of the multi-ring shear apparatus (Ishikawa et al. 2011) 69

Figure 6-2 Pavement structure and traffic load conditions of multi-ring shear tests: (a) cross section; (b) longitudinal section 70

Figure 6-3 Loading waveforms of each cycle in multi-ring shear tests 72

Figure 6-4 Resilient strain under different degrees of saturation: (a) C-9.5, (b) RC-9.5 73

Figure 6-5 Relationship between resilient axial strains in FL and ML tests 74

Figure 6-6 Effect of degree of saturation on resilient axial strain: (a) C-9.5, (b) RC-9.5 75

Figure 6-7 Permanent strain under different degrees of saturation: (a) C-9.5, (b) RC-9.5 77

Figure 6-8 Relationship between the increasing rate of permanent axial strain in FL and ML tests 78

Figure 6-9 Effect of degree of saturation on the increasing rate of ε_p: (a) C-9.5, (b) RC-9.5 79

Figure 6-10 Ratio of permanent strain to resilient strain and fitting curves by Equation 6-1: (a) C-9.5, (b) RC-9.5 81

Figure 6-11 Ratio of permanent strain to resilient strain fitted by Equation 6-3: (a) C-9.5, (b) RC-9.5 85

LIST OF TABLES

Table 2-1 Specification of filters 19

Table 3-1 Physical properties of Toyoura sand and Tomakomai soil 21

Table 3-2 Test sequence for M_r tests 25

Table 3-3 Loading steps in M_r tests 27

Table 3-4 S_r and ψ used to investigate the effect of suction hysteresis 28

Table 4-1 Regression analysis results of U tests 38

Table 4-2 Water content and density change by wheel load 40

Table 4-3 Regression analysis results of UW tests 41

Table 4-4 Resilient strain and M_r change during the wheel loading process 41

Table 4-5 Density change after freeze-thaw action 43

Table 4-6 Regression analysis results of FT tests 45

Table 5-1 Fitting parameters of different models 62

Table 5-2 Fitting errors of different models 63

Table 6-1 Test conditions for multi-ring shear tests (FL/ML) 71

Table 6-2 Average resilient axial strain under different test conditions 82

Table 6-3 Parameters related to water content in Equation 6-1 82

Table 6-4 Regression parameters and results by Equation 6-1 83

Table 6-5 Regression parameters and results by Equation 6-3 85

1 INTRODUCTION

1.1 Background

Asphalt pavements, typically including the asphalt layer, base course, and subgrade, suffer the cyclic loads generated by the traffic during the service life. As a typical type of flexible pavement, fatigue cracking and rutting damage caused by cyclic loads have become the major factor that affects its fatigue life, with unbound granular materials such as base course and subgrade being the most affected. As shown in Figure 1-1, the pavement suffers fatigue cracking and rutting damages under various climatic conditions during different seasons such as unsaturated drying and wetting cycles and freeze-thaw action. In areas with significant seasonal changes in snowy cold regions such as Hokkaido, a northern island in Japan, the effect of complex climatic and stress conditions cannot be ignored (Ishikawa et al. 2019; Lin et al. 2022). Japanese design guide (Japan Road Association 2006) calculates the allowable loading number of fatigue cracking (N_{fa}) and rutting (N_{fs}) under an equivalent 49-kN wheel load by Equations 1-1 and 1-2, which is based on the AI model (Asphalt Institute 1982) using a simplified three-layer model as shown in Figure 1-2.





Figure 1-1 Pavement suffering: (a) fatigue cracking; (b) rutting

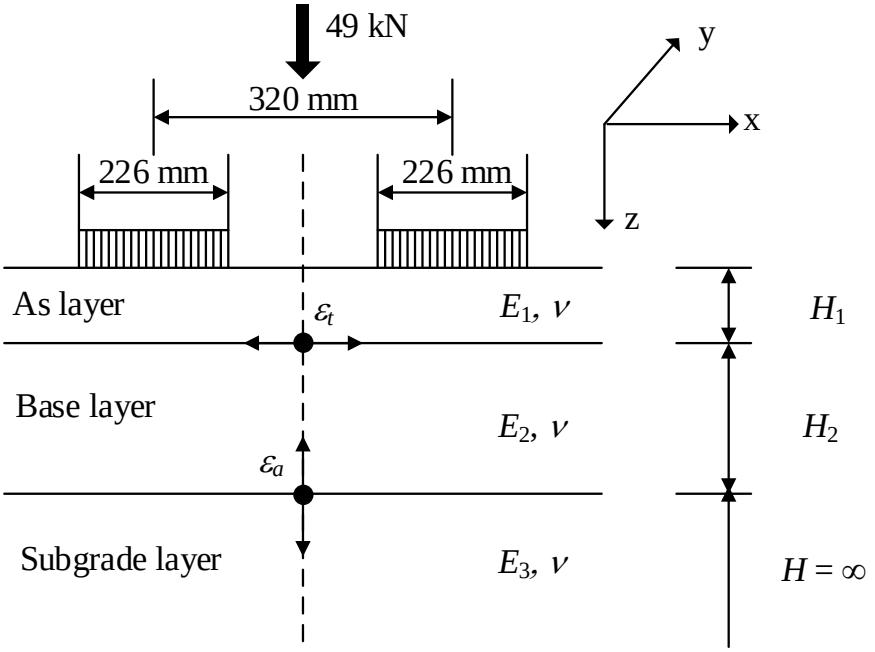


Figure 1-2 Three-layer model for allowable loading number calculation

$$N_{fa} = \beta_{a1} \cdot C_a \cdot \left\{6.167 \times 10^{-5} \cdot {\varepsilon_t}^{-3.291 \cdot \beta_{a2}} \cdot {E_1}^{-0.854 \cdot \beta_{a3}}\right\} \quad (1\text{-}1.1)$$

$$C_a = 10^M \quad (1\text{-}1.2)$$

$$M = 4.84 \times \left(\frac{VFA}{100} - 0.69\right) \quad (1\text{-}1.3)$$

$$\beta_{a1} = K_a \cdot \beta_{a1}' \tag{1-1.4}$$

$$K_a = \begin{cases} \frac{1}{8.27\times10^{-11}+7.83e^{-0.11H_a}}, & H_1 < 0 \\ 1 \quad\quad\quad\quad\quad\quad\quad\quad , & H_1 \geq 0 \end{cases} \tag{1-1.5}$$

$$\beta_{a1}' = 5.229 \times 10^4 \tag{1-1.6}$$

$$\beta_{a2} = 1.314 \tag{1-1.7}$$

$$\beta_{a3} = 3.018 \tag{1-1.8}$$

$$N_{fs} = \beta_{s1} \cdot \left\{1.365 \times 10^9 \cdot {\varepsilon_a}^{-4.477 \cdot \beta_{s2}}\right\} \tag{1-2.1}$$

$$\beta_{s1} = 2134 \tag{1-2.2}$$

$$\beta_{s2} = 0.819 \tag{1-2.3}$$

where β_{s1}, β_{s2}, β_{a1}, β_{a2}, and β_{a3} are the compensation rates for AI failure criteria based on the actual situation of Japanese pavement; C_a is the material parameter; M is a factor relates the *VFA* to C_a; *VFA* is Voids Filled with Asphalt; K_a is a correction factor, which relates to the thickness of asphalt mixture, H_1; ε_a is the compressive strain on the top surface of the subgrade layer; ε_t is the tensile strain on the lower surface of the asphalt layer.

There are several serious drawbacks that limit the applicability and accuracy of this fatigue failure criterion. For example, only elastic moduli of the base and subgrade layer are used while the effect of stress states on layer stiffness is not considered. Furthermore, the effects of moisture content and freeze-thaw action, greatly influence the stiffness of the base and subgrade layer (Berg et al. 1996; Cole et al. 1981; Johnson et al. 1978; Simonsen and Isacsson 2001; Simonsen et al. 2002), are also not considered. On the other hand, the rutting failure criterion is also limited in that it provides no indication of such as the behavior of rutting over time, the application of traffic loading, rate-hardening, the contribution of the non-subgrade layers to rutting, and principal stress axis rotation (PSAR). To overcome these shortcomings, the concept of resilient modulus (M_r) with the consideration of the effects of moisture content and freeze-thaw action is incorporated in the fatigue failure criterion, and the modified UIUC model with the consideration of PSAR is incorporated in the rutting failure criterion as shown in Figure 1-3 (Lin et al. 2021; Lin et al. 2022).

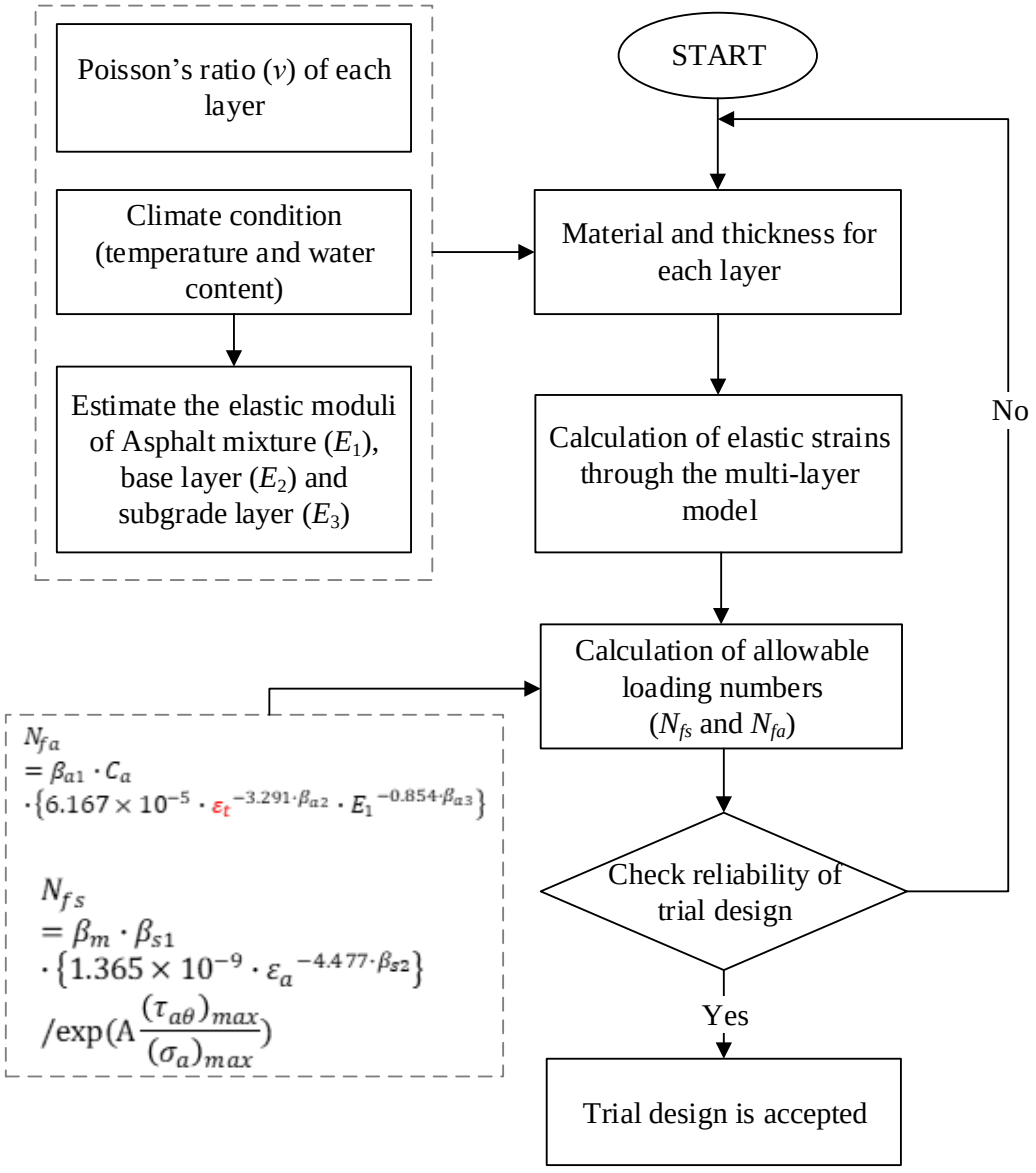


Figure 1-3 Sequence in modified Japanese flexible pavement design guide (Lin et al. 2021)

The current Mechanistic-Empirical Pavement Design Guide (MEPDG) utilizes a universal model for predicting M_r under different stress conditions and considers the effect of moisture fluctuation by estimating the ratio of M_r to M_r at optimum moisture content (AASHTO 2020; NCHRP 2004). Many researchers also proposed M_r predictive models by incorporating the concept of matric suction based on the universal model of MEPDG to capture the effect of moisture conditions (Gupta et al. 2007; Khoury et al. 2009; Liang et al. 2008; Lytton 1995; Ng et al. 2013; Oh et al. 2012; Sahin et al. 2013). In addition, MEPDG also estimates the climatic effects on pavement materials, responses, and distress of climate using the Enhanced Integrated Climatic Model (EICM) in an integrated manner (AASHTO 2020). However, as this model only

estimates the climatic effects by adjusting the overall magnitude of the universal M_r predictive model, it lacks theoretical explanations for the effects of freeze-thaw action. Therefore, the comprehensive effect of the complex climatic conditions on the M_r of subgrade soils needs to be further studied. To investigate the effect of climatic conditions including moisture and temperature changes, Lin et al. (2022) conducted M_r tests under different combinations of the conditions and proposed a modified M_r predictive model able to capture the effects of moisture and freeze-thaw action comprehensively based on the Ng model (Ng et al. 2013). However, the behavior of frost-susceptible soil under freeze-thaw action and the difference between the drying and wetting paths caused by the hysteresis of the SWCC were not considered, and the effects of wheel loads during different seasons also need to be further understood.

On the other hand, researchers proposed predictive models for permanent axial deformation of unbound granular materials mainly in terms of shear strength or resilient strain to evaluate the rutting damage (AASHTO 2020; Chow et al. 2014; Korkiala-Tanttu 2009; Tseng and Lytton 1989). However, there are some disputes about whether these models consider the effect of principal stress axis rotation (PSAR), a phenomenon caused by moving wheel loads and greatly amplified the permanent deformation of the base and subgrade layer (Arthur et al. 1980; Ishikawa et al. 2011; Lekarp et al. 2000a, 2000b; Lin et al. 2019). To evaluate the effect of PSAR on the permanent deformation of unbound granular material under moving wheel loads, Ishikawa et al. (2011) examined the relationship between the axial strain with and without PSAR and proposed a parameter $(R_S)_{ave}$ reflecting the average ratio between them. Furthermore, Lin et al. (2019) combined $(R_S)_{ave}$ with the UIUC model (Chow et al. 2014) and modified the allowable loading number equation against rutting by incorporating the MEPDG rut depth predictive model and $(R_S)_{ave}$. However, since the UIUC model is based on the shear strength, the permanent axial deformation model based on resilient strain such as the MEPDG rut depth predictive model with consideration of the effect of PSAR still needs to be further studied.

1.2 Literature Review

1.2.1 M_r predictive models

Resilient modulus (M_r), as shown in Figure 1-4, originally defined as the ratio of the cyclic deviator stress to the resilient axial strain during cyclic loading by Seed et al.

(1955), is a crucial mechanical characteristic used to assess the resistance of pavement structures to cyclic vertical loads. It has been widely used in pavement design works since the publication of the *AASHTO Guide for Design of Pavement Structures* (AASHTO 1986) and plays a major role in determining pavement responses and fatigue life (Brown 1996; Kim and Kim 2007; Li and Selig 1994). Furthermore, the M_r of subgrade soil is affected by many factors, including stress, moisture, and temperature conditions, which comprehensively interact to define the response of the soil (Berg et al. 1996; Cole et al. 1981; Johnson et al. 1978; Simonsen and Isacsson 2001; Simonsen et al. 2002).

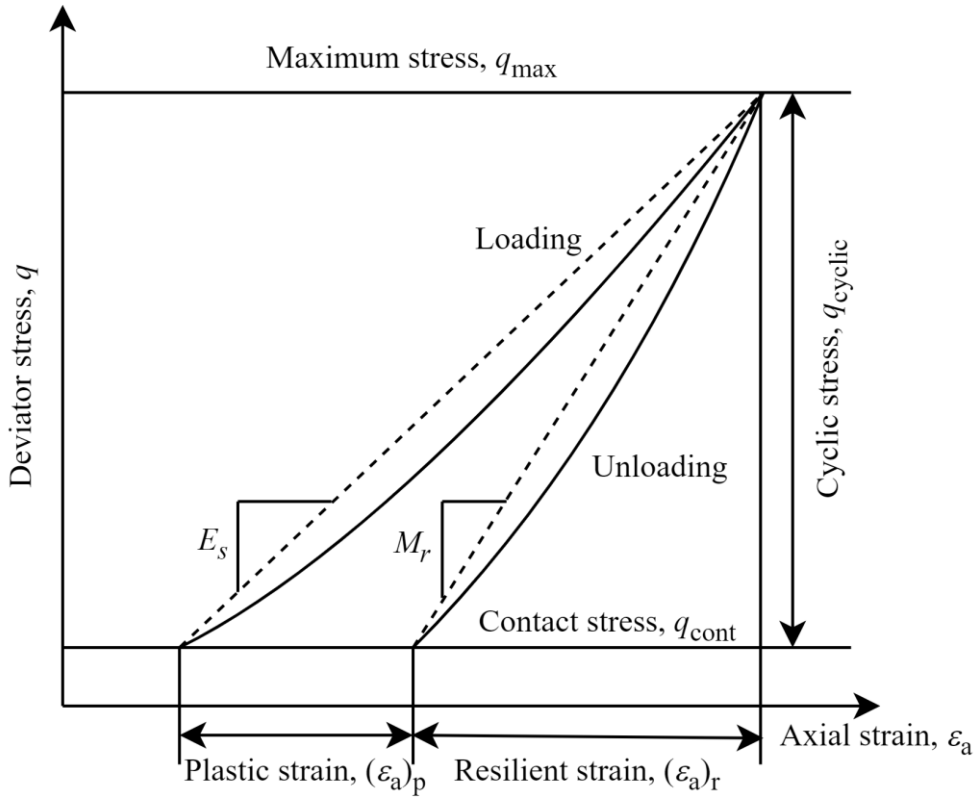


Figure 1-4 Schematic diagram of the definition of M_r

MEPDG (AASHTO 2020) recommends the test protocol of the AASHTO T-307 (AASHTO 2017) to measure the M_r and fit the results by the generalized predictive model shown as follows:

$$M_r = k_1 p_a \left(\frac{\theta}{p_a}\right)^{k_2} \left(\frac{\tau_{oct}}{p_a} + 1\right)^{k_3} \quad (1\text{-}3.1)$$

$$\theta = \sigma_1 + \sigma_2 + \sigma_3 \quad (1\text{-}3.1)$$

$$\tau_{oct} = \frac{1}{3}\sqrt{(\sigma_1 - \sigma_2)^2 + (\sigma_1 - \sigma_3)^2 + (\sigma_2 - \sigma_3)^2} \quad (1\text{-}3.3)$$

where k_1, k_2, and k_3 are regression parameters; σ_1, σ_2, and σ_3 are major principal stress, intermediate principal stress, and minor principal stress, respectively; p_a is atmospheric pressure and set as 101 kPa in this study; θ is bulk stress; τ_{oct} is octahedral stress.

Guide for Mechanistic-Empirical Design of New and Rehabilitated Pavement Structures reported the estimation method for the effect of changing moisture content as shown in the following equation (NCHRP 2004):

$$\log\frac{M_r}{M_{ropt}} = a + \frac{b-a}{1+EXP\left[\ln\left(-\frac{b}{a}\right)+k_m(S-S_{opt})\right]} \quad (1\text{-}4)$$

where S is the degree of saturation in decimals; S_{opt} is the degree of saturation at optimum moisture content in decimals; a is the minimum of log (M_r/M_{ropt}); b is the maximum of log (M_r/M_{ropt}); k_m is regression parameter.

However, Equation 1-4 lacks the mechanical explanation of unsaturated soil, and its applicability to other regions may not be good because the empirical equation is based on the field data in the USA. Han and Vanapalli (2016) summarized a series of predictive models for unsaturated subgrade soils and indicated that the Ng model (Ng et al. 2013) shown in Equation 1-5 has a relatively high accuracy:

$$M_r = k_1 p_a \left(\frac{\theta}{p_a}\right)^{k_2} \left(\frac{\tau_{oct}}{p_a} + 1\right)^{k_3} \left(\frac{\psi}{\sigma_{net}} + 1\right)^{k_4} \quad (1\text{-}5)$$

where k_4 is regression parameter; σ_{net} is net mean stress, defined as (θ/3-u_a); ψ is matric suction. It should be noted that the octahedral shear stress τ_{oct} is used in Equation 1-5 instead of the cyclic deviator stress q_{cyc} in the original form of the Ng model. According to the definition of octahedral shear stress, when $\sigma_2 = \sigma_3$, $\tau_{oct} = \left(\sqrt{2}/3\right)(\sigma_1 - \sigma_3)$. Considering the regression parameters, using the octahedral shear stress or the deviator stress does not affect the fitting result. Furthermore, since MEPDG uses octahedral shear stress in its predictive model, the Ng model is converted to the current form to keep the consistency.

Based on Equation 1-5, Lin et al. (2022) proposed a modified model to capture both the effects of moisture content and freeze-thaw action by incorporating a new parameter F_{clim} multiplying k_1 to k_4:

$$M_r = F_{clim} \cdot k_1 p_a \left(\frac{\theta}{p_a}\right)^{F_{clim}\cdot k_2} \left(\frac{\tau_{oct}}{p_a} + 1\right)^{F_{clim}\cdot k_3} \left(\frac{\psi}{\sigma_{net}} + 1\right)^{F_{clim}\cdot k_4} \quad (1\text{-}6)$$

where F_{clim} is the climatic factor. This model not only captures the effect of freeze-thaw action on the overall magnitude of the M_r surface in the σ_d-σ_c-M_r 3D space but also reflects the change of the surface shape, which will be employed to investigate the effect of complex climatic and stress conditions on M_r in the later sections of this paper.

1.2.2 Rutting failure models

To evaluate the rutting damage, researchers proposed predictive models for permanent axial deformation of unbound granular materials mainly in terms of shear strength or resilient strain (AASHTO 2020; Chow et al. 2014; Korkiala-Tanttu 2009; Tseng and Lytton 1989). In practice, based on the Tseng-Lytton model (Tseng and Lytton 1989), the Mechanistic-Empirical Pavement Design Guide (MEPDG) (AASHTO 2020) proposed a rut depth predictive model for unbound pavement sublayers such as the base course and subgrade layer in terms of resilient strain as shown in Equation 1-7, which is widely used in pavement design works in the USA. The rut depth predictive model (MEPDG model) adopts the relation between permanent strain and resilient strain by the mechanistic-empirical method. The relation was established based on the laboratory repeated load permanent deformation tests and calibrated with the LTPP (Long-Term Pavement Performance) database to adapt to field conditions.

$$\Delta_{p(soil)} = \beta_1 k_{s1} \varepsilon_v h_{soil} \left(\frac{\varepsilon_0}{\varepsilon_r}\right) exp\left[-\left(\frac{\rho}{N_c}\right)^{\beta}\right] \tag{1-7.1}$$

$$\left(\frac{\varepsilon_0}{\varepsilon_r}\right) = \frac{\left(e^{(\rho)\beta}\cdot a_1 \cdot E^{b_1}\right)+\left(e^{\left(\frac{\rho}{10^9}\right)^{\beta}}\cdot a_9 \cdot E^{b_9}\right)}{2} = \frac{\left(0.15\cdot e^{(\rho)\beta}\right)+\left(20\cdot e^{\left(\frac{\rho}{10^9}\right)^{\beta}}\right)}{2} \tag{1-7.2}$$

$$\log \beta = -0.61119 - 0.017638 W_c \tag{1-7.3}$$

$$\rho = 10^9 \left(\frac{C_0}{1-(10^9)^{\beta}}\right)^{\frac{1}{\beta}} \tag{1-7.4}$$

$$C_0 = \ln\left(\frac{a_1 \cdot E^{b_1}}{a_9 \cdot E^{b_9}}\right) = -4.89285 \tag{1-7.5}$$

where $\Delta_{p(soil)}$ is permanent or plastic deformation for the base course or subgrade layer; N_c is the number of axle-loading cycles; ε_0 is intercept determined from laboratory repeated load permanent deformation tests; ε_r is resilient strain imposed in laboratory repeated load permanent deformation tests to obtain material properties ε_0, β, and ρ; ε_v is the average vertical resilient or elastic strain in the base course or subgrade layer; h_{soil} is the thickness of the unbound base course or subgrade layer; k_{s1} is global calibration

coefficients: k_{s1}=1.673 for granular materials and 1.35 for fine-grained materials; β_1 is local calibration constant for the rutting in the unbound layers, and the local calibration constant was set to 1.0 for the global calibration effort; a_1, a_9, b_1, b_9 are regression constants, a_1=0.15, a_9=20.0, b_1=b_9=0; E is resilient modulus, which does not affect the predictive result according to Equation 1-7.5; W_c is water content.

However, there are some disputes about whether these models consider the effect of principal stress axis rotation (PSAR). The application of PSAR to engineering works was originally proposed by Arthur et al. (1980) with an example of the foundation soil of offshore structures subjected to cyclic loading from waves. Lekarp et al. (2000a, 2000b) extended this concept to the response of unbound aggregates under moving wheel loads in pavement structures and illustrated the change of stress states. The effect of PSAR exists in the field condition under the cyclic moving wheel load from the traffic, but it is implicitly considered by the calibrations of the MEPDG model as shown in Equation 1-7. To evaluate the effect of PSAR on the permanent deformation of unbound granular material under moving wheel loads, Ishikawa et al. (2011) examined the relationship between the axial strain with and without PSAR and proposed a parameter $(R_S)_{ave}$ reflecting the average ratio between them. Furthermore, Lin et al. (2019) combined $(R_S)_{ave}$ with the UIUC model as shown in Equation 1-8 (Chow et al. 2014) and proposed the modified UIUC model considering the effect of PSAR as shown in Equation 1-9:

$$\varepsilon_p(N_c) = AN_c{}^B\sigma_d{}^C\left(\frac{\tau_f}{\tau_{max}}\right)^D \tag{1-8.1}$$

$$\tau_f = \sqrt{(\sigma_d/2)^2 - [\sigma_f - (\sigma_3 + \sigma_d/2)]^2} \tag{1-8.2}$$

$$\sigma_f = \frac{2\sigma_3(1+tan^2\phi)+\sigma_d(1+tan^2\phi)-\sqrt{\sigma_d{}^2tan^2\phi(1+tan^2\phi)}}{2(1+tan^2\phi)} \tag{1-8.3}$$

$$\tau_{max} = c + \sigma_f tan\phi \tag{1-8.4}$$

$$\varepsilon_p(N_c) = AN_c{}^B(\sigma_a)_{max}{}^C\left(\frac{p_a}{\tau_{max}}\right)^D(R_S)_{ave} \tag{1-9.1}$$

$$(R_S)_{ave} = exp\left(E\frac{(\tau_{a\theta})_{max}}{(\sigma_a)_{max}}\right) \tag{1-9.2}$$

where $\varepsilon_p(N_c)$ is the permanent strain corresponding to N_c-load cycles; σ_d is applied deviator stress; τ_f is mobilized shearing resistance acting on failure plane; σ_f is normal stress acting on failure plane; σ_a is applied axial stress; $\tau_{a\theta}$ is applied shear stress; τ_{max}

is available shear strength obtained through Mohr-Coulomb failure criteria; *A* to *D* are regression parameters; p_a is the atmospheric pressure, equal to 101 kPa in this study; *A* to *E* are regression parameters.

1.3 Thesis Objectives

In this study, a series of M_r tests for two types of subgrade soil with different frost susceptibility under different climatic and wheel loading conditions were conducted to investigate the effect of complex climatic and stress conditions on the M_r of subgrade soils, especially under the effect of suction hysteresis. Furthermore, most of the existing models considering Bishop's effective stress factor did not explain or verify the application on the wetting path of SWCC, and there are also some disputes about the factors in the equations or the determination of χ. To verify the applicability on the wetting path of SWCC and find the appropriate determination method for χ, three modified M_r predictive models incorporating Bishop's effective stress factor were combined with three χ estimation models and verified by the test results.

The modified UIUC model shows better accuracy in predicting the permanent strain of unbound granular materials under repeated moving wheel loads as compared with the UIUC model. To improve the applicability of the MEPDG model like the UIUC model, this study examines the effect of PSAR on the resilient axial strain and permanent axial strain of unbound aggregate materials and clarifies the meaning of the calibration factor in the MEPDG model, which implicitly considers the effect of PSAR. In this study, a series of laboratory cyclic loading tests of unbound granular materials under the constant maximum axial stress and different maximum shear stresses using a multi-ring shear apparatus is conducted. It is noted that since the PSAR is closely related to the cyclic shear stress caused by the moving wheel loads in the multi-ring shear tests, the existence of PSAR corresponds to whether the shear stress exists or not, and that the maximum shear stress during a loading cycle affects the rotational angle of PSAR. Then, the test results with and without considering PSAR are compared, and fitted by the MEPDG model to verify and discuss the applicability in predicting the permanent strain under the effect of PSAR.

1.4 Thesis Organization

Figure 1-5 illustrates the flowchart of this study to show the relation among all chapters. Besides Chapter 1 and Chapter 7, the contents of this study are mainly divided into two parts: Chapters 2-5 related to the estimation of resilient modulus; and Chapter 6 related to the estimation of rutting damage. Chapter 1 introduces the background, literature review, objective, and organization of this study. Chapter 2 gives the details of the test apparatus used in this study, including water retention test apparatus and unsaturated freeze-thaw triaxial apparatus. Chapter 3 describes the test materials and test methods used in the water retention tests and resilient modulus tests under different climatic and stress conditions. Chapter 4 shows the results of resilient modulus tests under various test conditions and discusses the effects of complex climatic and wheel loading conditions on M_r. Chapter 5 verifies and compares the applicability of suction stress-based M_r predictive models by combining different χ estimation models. Chapter 6 proposes a modified permanent axial strain predictive model with consideration of the effect of PSAR based on the MEPDG rut depth predictive model to estimate the rutting damage more precisely. Chapter 7 summarizes the conclusions obtained in this study and the possible assignments in the future.

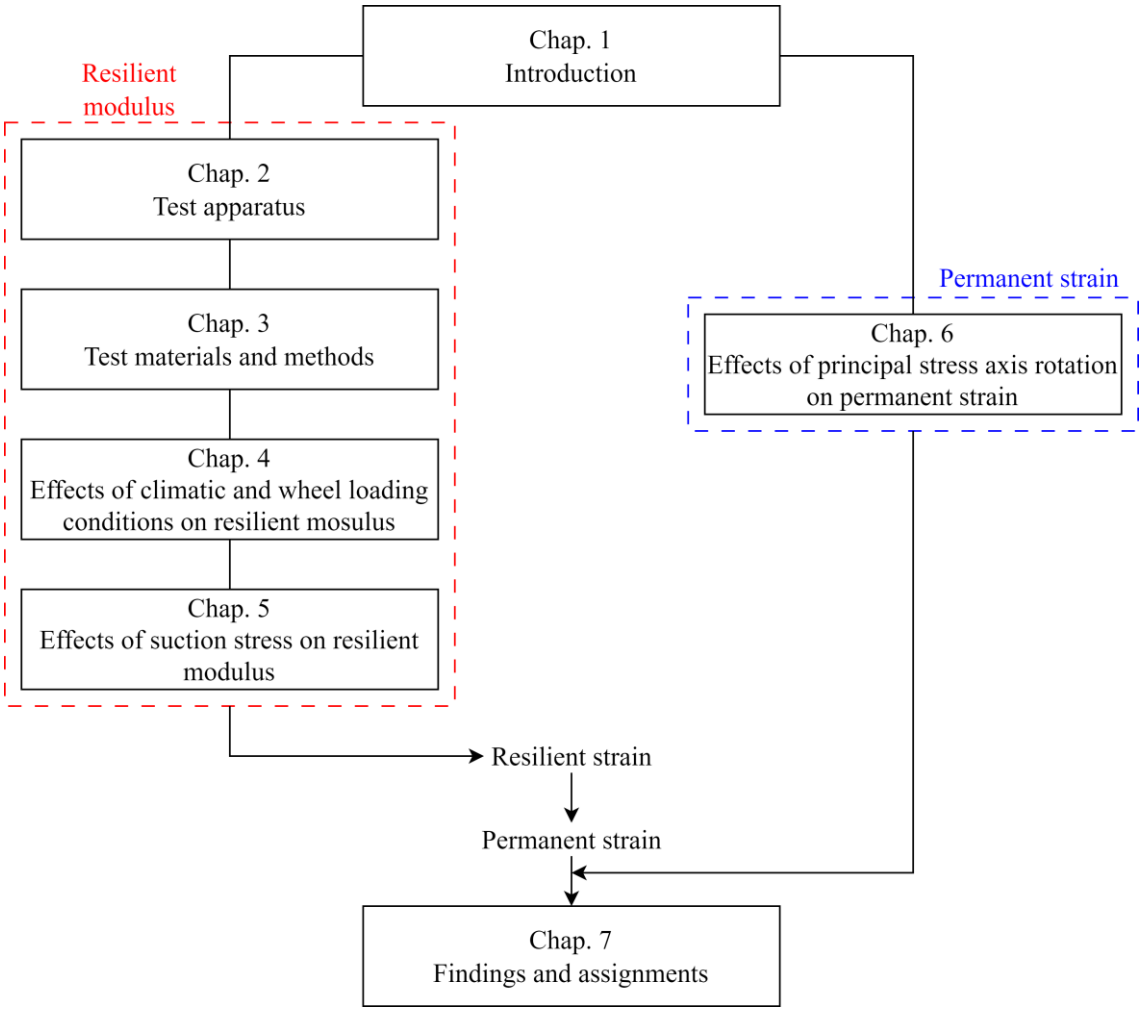


Figure 1-5 Flow chart of this study

2 TEST APPARATUS

2.1 Water Retention Test Apparatus

The water retention test using the pressure plate method is conducted in this study to obtain the soil-water characteristic curve (SWCC) of the test materials. Traditionally, the testing time is very long to obtain both the drying path and wetting path of the SWCC by the staged pressurization method. To improve the experimental efficiency, a continuous pressurization water retention test method developed by Hatakeyama et al. (2015) as shown in Figure 2-1 was used in this study. This apparatus is based on the axis-translation method (Hilf 1956) and has been confirmed by studies to have the same accuracy as the traditional stage pressurization method (Alowaisy et al. 2020; Kato et al. 2015; Kim et al. 2021).

In the continuous pressurization method, the pore air pressure is continuously changed, and the suction is determined by measuring the pore water pressure in the specimen during the test with a micro-tensiometer placed inside the specimen. The water content of the specimen is then measured by recording the drainage volume simultaneously, and the SWCC can be drawn from the relationship between the suction and the water content of the soil. Unlike conventional water retention tests such as the staged pressurization method, this method is characterized by its ability to draw a continuous SWCC and relatively high experimental efficiency.

As shown in Figure 2-1, The size of the specimen is 70mm in diameter and 30mm in height. There are two water paths on the pedestal at the bottom of the specimen: one for water entry when preparing the specimen; and another for water drainage when conducting the water retention test. A ceramic disk that is water-permeable but air-impermeable is installed on the water drainage path to ensure no air will be drained during the test. The drainage water enters a double burette, and the volume is measured by a differential pressure gauge. At the top, the air pressure enters through the cap of the apparatus from above, which is provided by the pressure regulator and controlled automatically by the EP. Besides, a micro-tensiometer consisting of a pore water pressure gauge and a porous cup is installed at the center of the cap to measure the pore water pressure during the test.

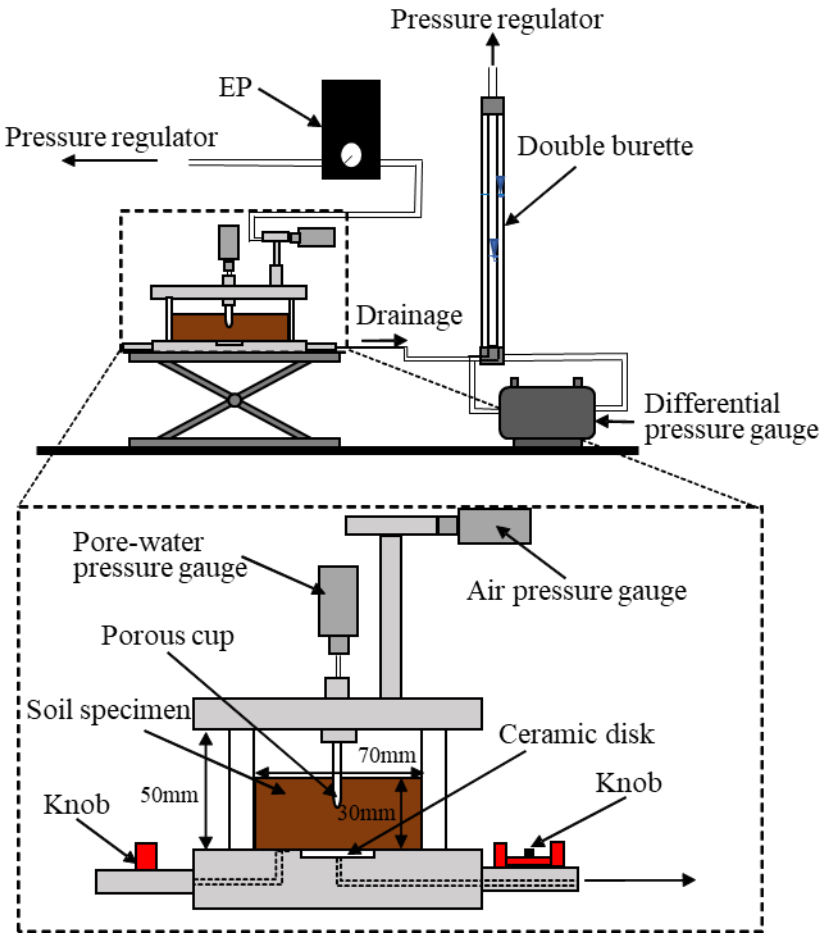


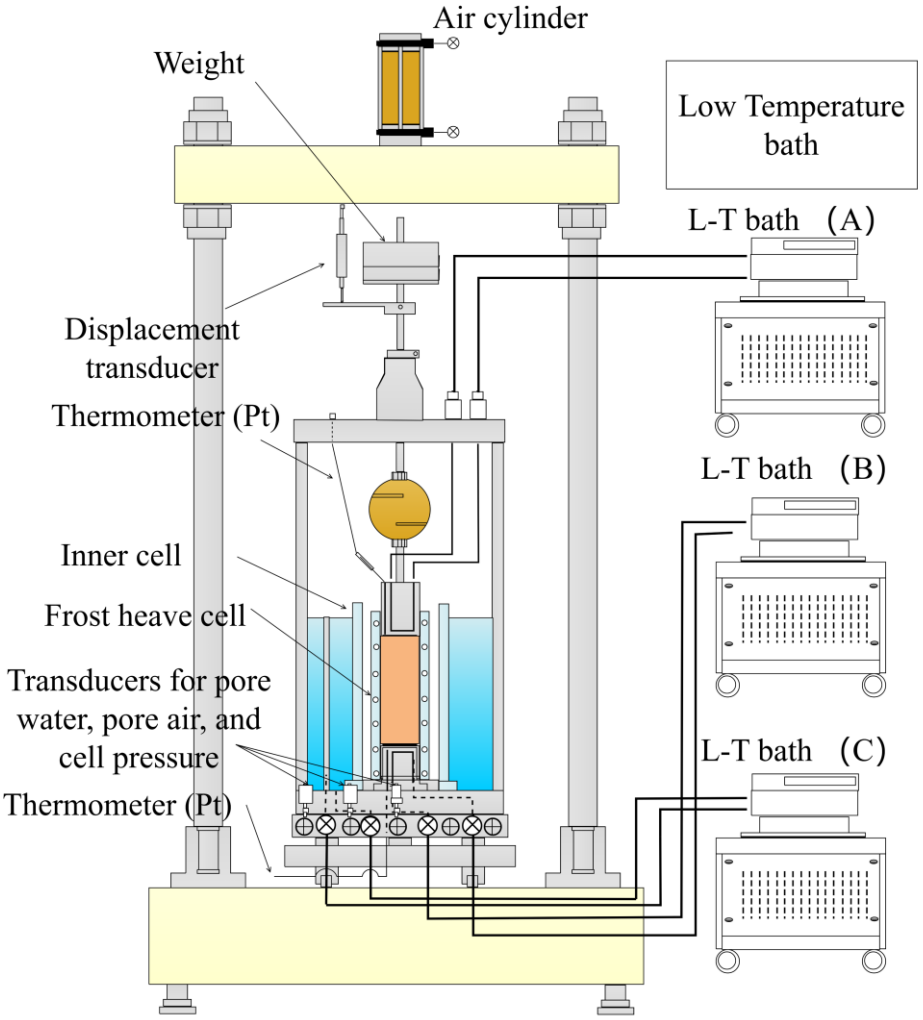
Figure 2-1 Water retention test apparatus by continuous pressurization method

2.2 Unsaturated Freeze-Thaw Triaxial Apparatus

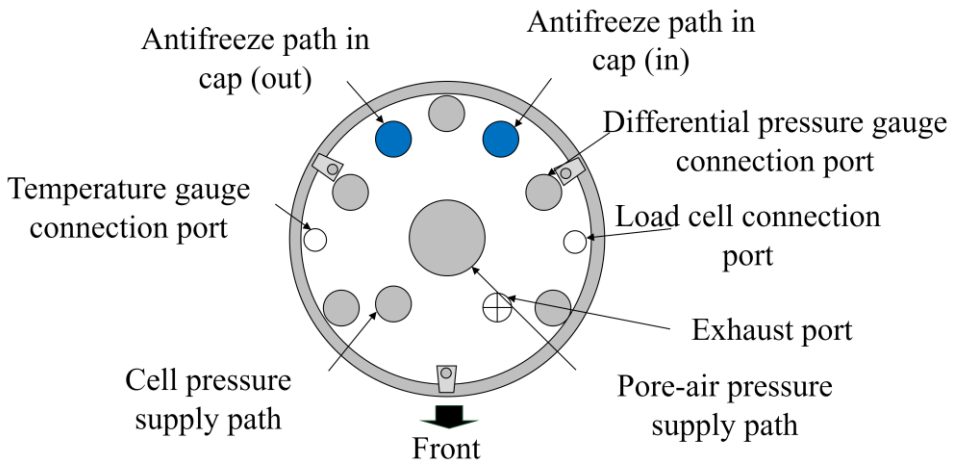
As shown in Figure 2-2, an unsaturated freeze-thaw cyclic loading triaxial apparatus is used to measure the resilient modulus under different climatic conditions. The main body of this apparatus is similar to the conventional triaxial compression apparatus, consisting of a reaction frame, a confining pressure cell, a specimen pedestal, and a loading cap. However, unlike applying a constant strain rate in triaxial compression tests, a periodic waveform load with amplitude varying over time is required in the measurement of the M_r. Therefore, a Bellofram-type air cylinder is employed as the loading output component in this apparatus, which can apply cyclic axial load through computer control.

As shown in Figure 2-2 (a), three low-temperature baths are employed to control the temperature during the freeze-thaw process in this study. The L-T bath (A) connected to the loading cap, the L-T bath (B) connected to the pedestal, and the L-T

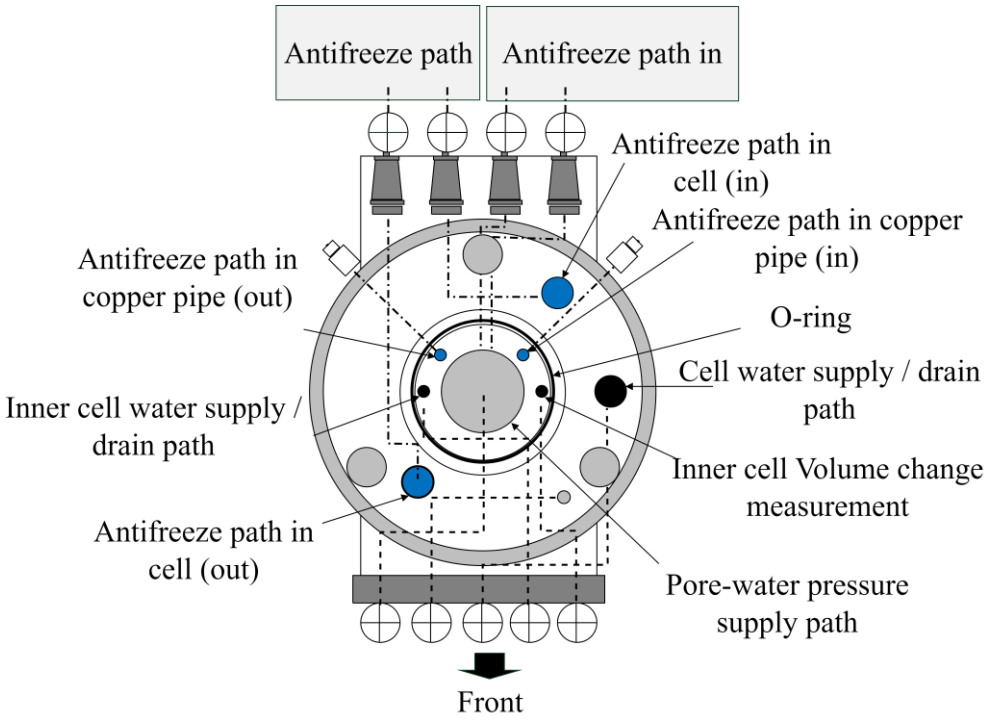
bath (C) connected to the cell controls the temperature at the top of the specimen, the temperature at the bottom of the specimen, and the environmental temperature around the specimen, respectively. Besides, two Platinum thermometers are employed to monitor the temperatures at the top and bottom of the specimen.



(a) Schematic diagram of test apparatus



(b) Structural design of cap

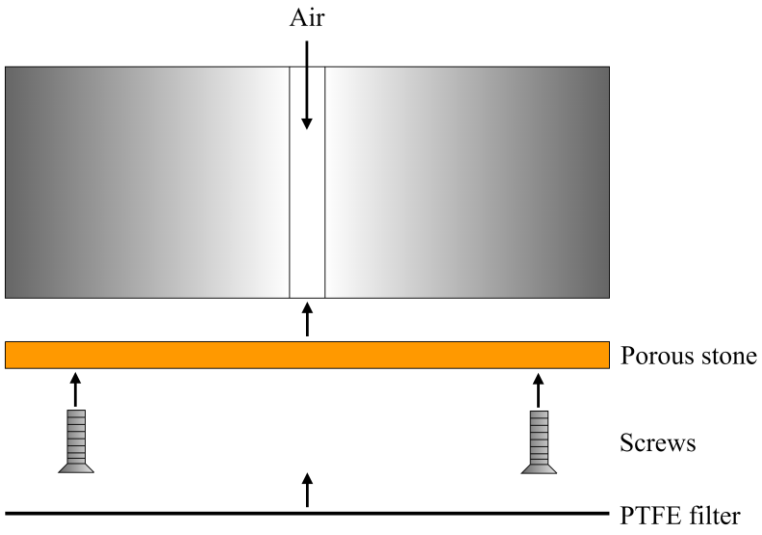


(c) Structural design of pedestal

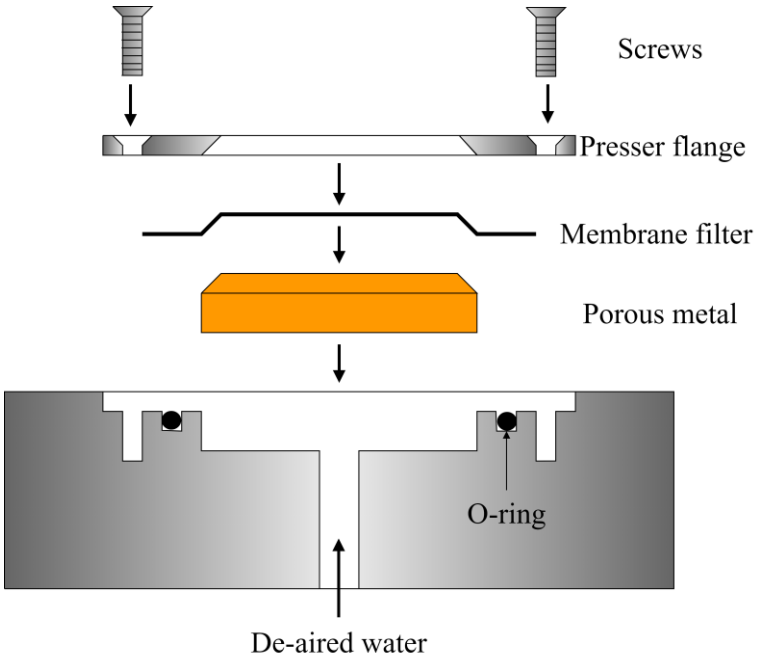
Figure 2-2 Unsaturated freeze-thaw cyclic loading triaxial test apparatus: (a) Schematic diagram of test apparatus; (b) Structural design of specimen cap; (c) Structural design of specimen pedestal

To keep the suction constant in different stages, the axis-translation technique is employed in this study, which was originally introduced by Hilf (1956) and widely used in unsaturated soil tests. As shown in Figure 2-3, a Versapor membrane filter that is water-permeable but air-impermeable is installed at the bottom of the specimen, while

a PTFE filter that is air-permeable but water-impermeable is installed at the top of the specimen. In this way, a certain suction can be determined and controlled by adjusting the pore air pressure and pore water pressure. However, the air-impermeability of the Versapor membrane filter is limited below a specific pressure threshold called “Air Entry Value (AEV)”, exceeding which the air starts to penetrate. To evaluate the AEV of the Versapor membrane filter, a preliminary test of the drainage change with the increasing air pressure is conducted. As shown in Figure 2-4, it can be found that the drainage starts to increase rapidly when air pressure exceeds 80 kPa and has a sudden change at 100 kPa. Therefore, the AEV of the Versapor membrane is determined as 100 kPa, but better to be lower than 80% of the AEV if considering long experimental durations. The specifications of the filters are shown in Table 2-1.



(a) Specimen cap



(b) Specimen pedestal

Figure 2-3 Installation of PTFE and Versapor membrane filters: (a) Specimen cap; (b) Specimen pedestal

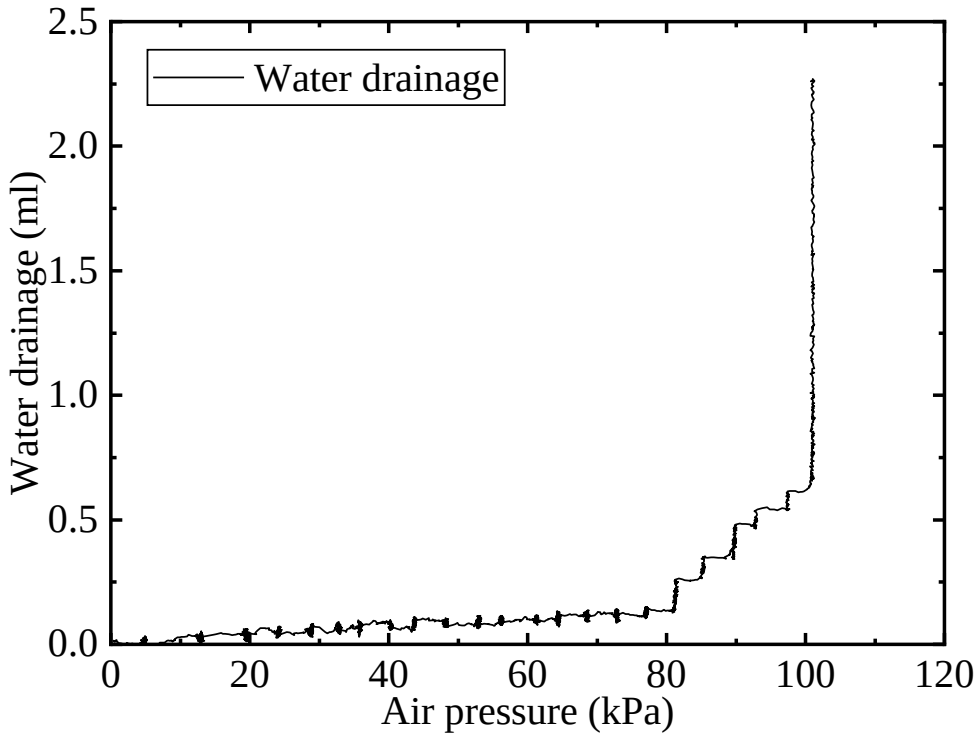


Figure 2-4 Measurement of AEV of Versapor membrane filter

Table 2-1 Specification of filters

	Material	AEV (kPa)	Thickness (μm)	Pore size (μm)
Versapor membrane filter	Acrylic copolymer	100	94	0.45
PTFE filter	PTFE	-	135	3

3 TEST MATERIALS AND METHODS

3.1 Test Materials

As shown in Figure 3-1, two types of soils are utilized in this study: Toyoura sand (Japanese standard sand) and subgrade soil sampled from the site. The subgrade soil is sampled from the Tomakomai Winter Test Track, an experimental road constructed by the Civil Engineering Research Institute for Cold Region (CERI), which is located at Tomakomai, Hokkaido, Japan. This subgrade soil is a kind of volcanic soil with a relatively small density, hereinafter referred to as Tomakomai soil. According to the Unified Soil Classification System of ASTM (2017), Toyoura sand is classified as SP, poorly graded sand; and Tomakomai soil is classified as SM, silty sand. The physical properties and the grain size distribution curves are shown in Table 3-1 and Figure 3-2, respectively. It should be noted that according to the standard of AASHTO T 307-99 (AASHTO 2017), the particles exceeding 25% of the available largest mold diameter should be removed in this study to fit the test apparatus size. The specimens were compacted to reach a degree of compaction of 95%, corresponding to a dry density of 1.54 g/cm3 for Toyoura sand and 1.21 g/cm3 for Tomakomai soil to satisfy the quality control of the subgrade layer in asphalt pavement provided by Japan Road Association (2019). To check the crushability, the grain size test of Tomakomai soil after compaction is conducted. As shown in Figure 3-2, the grain size distribution curves of Tomakomai soil before and after compaction are nearly the same, which indicates that the effect of compaction on the grain size distribution of Tomakomai soil is small. Tomakomai soil is a type of frost susceptible soil, also named SFG subgrade material. According to the frost susceptibility test of JGS 0172 (Japanese Geotechnical Society 2018), the frost susceptibility of Tomakomai soil is at a medium level (Yasuoka et al. 2021). On the other hand, Toyoura sand is non-frost susceptible.

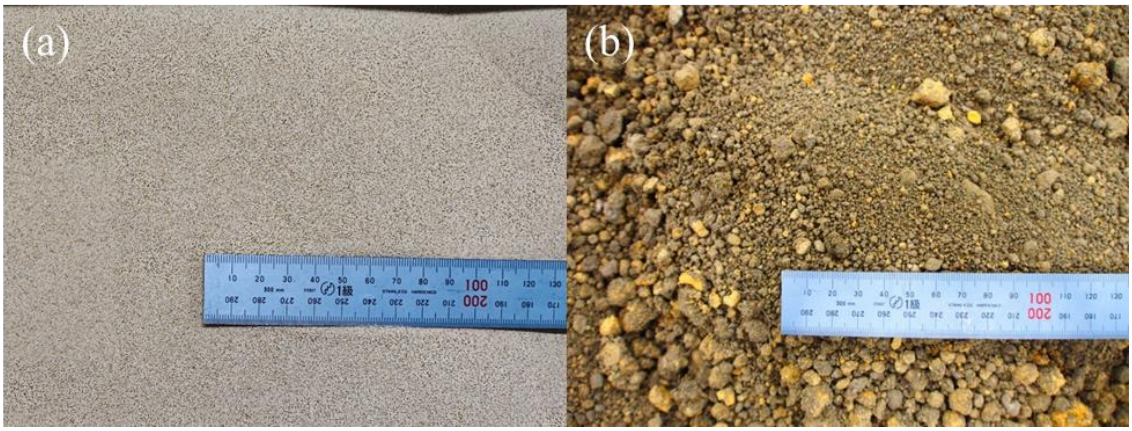


Figure 3-1 Photos of test materials: (a) Toyoura sand; (b) Tomakomai soil

Table 3-1 Physical properties of Toyoura sand and Tomakomai soil

Material	Soil particle density (g/cm^3)	Maximum dry density (g/cm^3)	Optimum water content (%)	Mean particle size (mm)	Fine fraction content (%)
Toyoura sand	2.65	1.62	14.0	0.19	0.7
Tomakomai soil	2.64	1.27	32.0	0.68	21.0

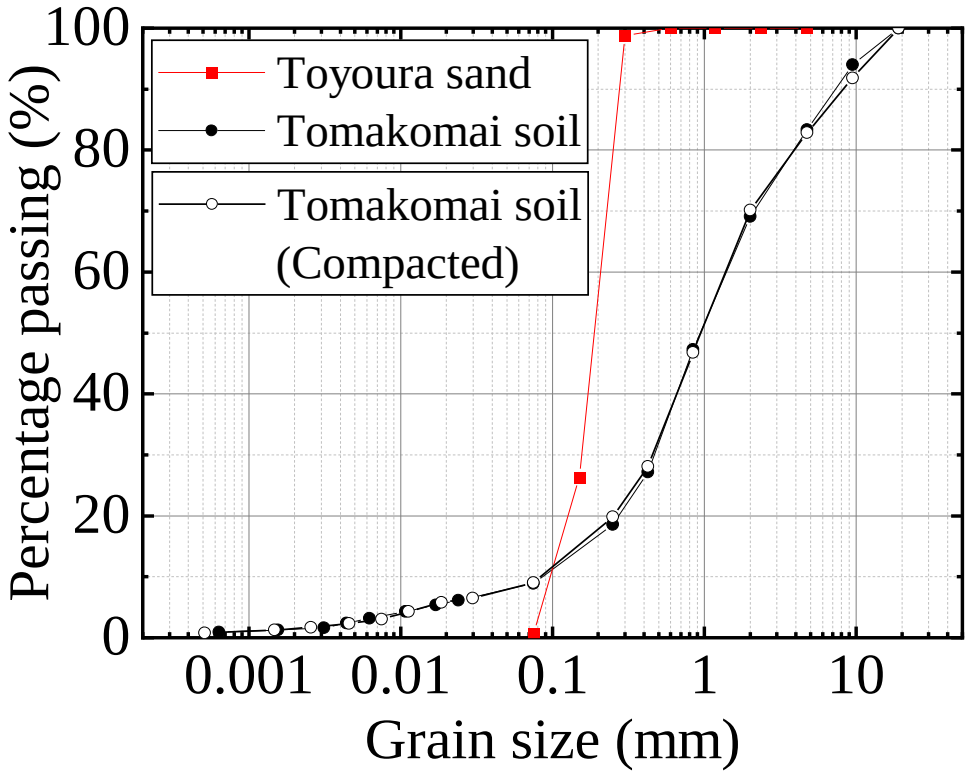
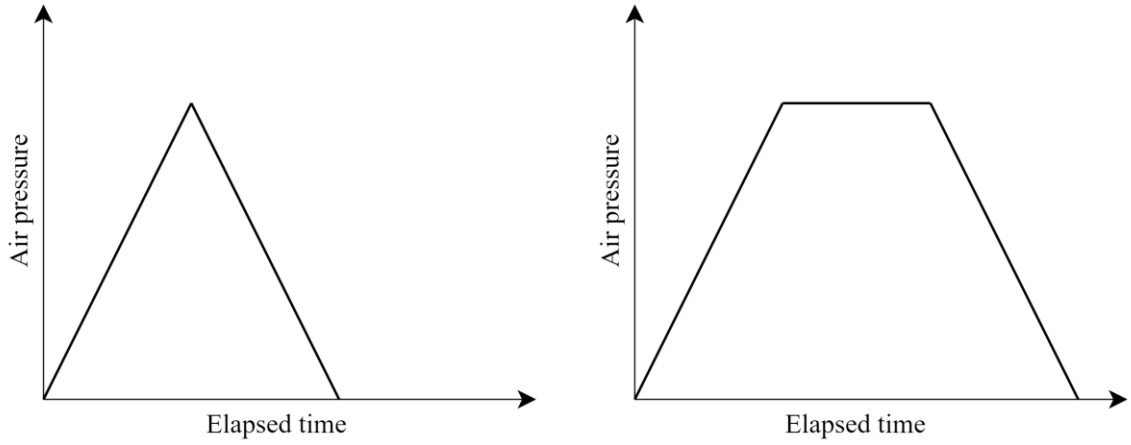


Figure 3-2 Grain size distribution curves of Toyoura sand and Tomakomai soil

3.2 Water Retention Test

3.2.1 Test sequence

The air pressurization types in the continuous pressurization method are divided into “triangle loading” and “trapezoid loading” as shown in Figure 3-3 (Hatakeyama et al. 2015). Generally, the triangle loading method is appropriate for materials with low water retention ability and with no drainage lag in response to air pressure loading, such as sandy soils with low fine fraction content. However, for clays or sandy soils with high fine fraction content, the water drainage lag may occur since the dissipation of the excess pore water pressure is slower than the increment of pore air pressure. As a result, although the trapezoid loading method keeping a specific air pressure is relatively time-consuming compared with the triangle loading method, it can catch the dissipation of the excess pore water pressure and obtain more accurate SWCC, which is appropriate for clays or sandy soils with high fine fraction. Before the formal test, the specimen is prepared by compacting in three layers to reach the 95% degree of compaction and saturated by applying a pressure of -90 kPa in the degassed water. During the test process, the pore-air pressure was increased with a constant speed (0.06 kPa/min for Toyoura sand; 0.03 kPa/min for Tomakomai soil) from 0 kPa to a specific maximum pressure and was decreased with the same speed back to 0 kPa after keeping the maximum pressure constant for 25 hours. Meanwhile, the pore water pressure and the volume of water drainage were simultaneously recorded to calculate the matric suction and the degree of saturation.

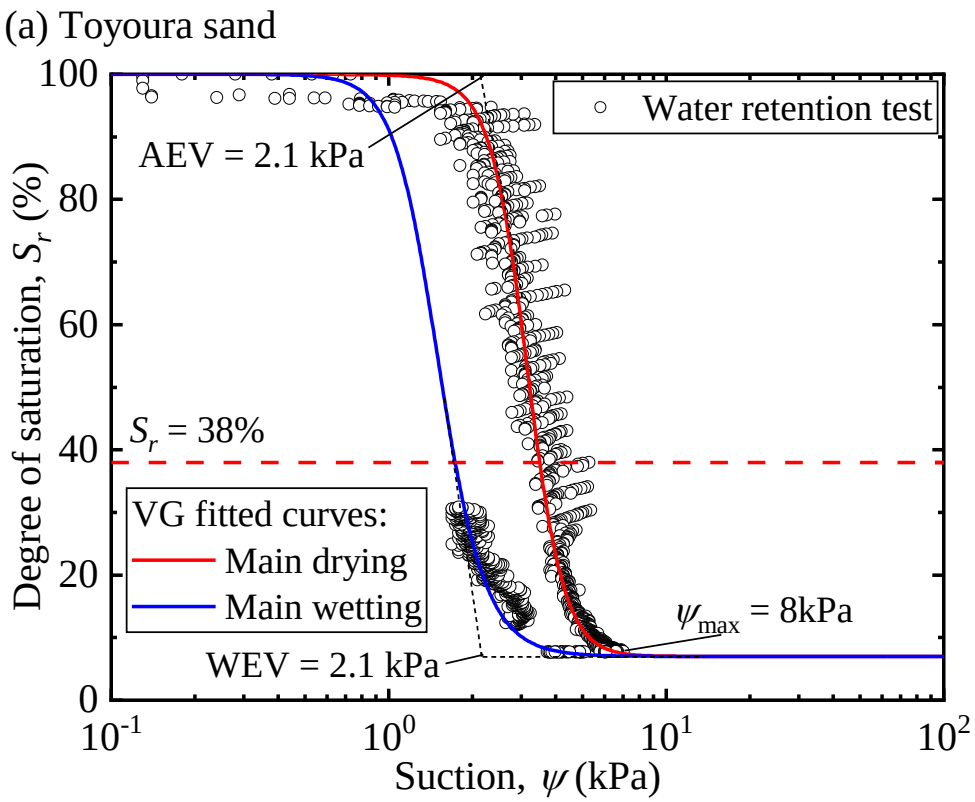


(a) Triangle loading (b) Trapezoid loading

Figure 3-3 Conceptual diagram of air pressurization types: (a) Triangle loading; (b) Trapezoid loading

3.2.2 SWCC under suction hysteresis

Figure 3-4 shows the SWCCs of Toyoura sand and Tomakomai soil, which are fitted by the VG mode (VanGenuchten 1980). It can be found that the drying and wetting paths of SWCCs are different, namely "suction hysteresis", which is due to the 'ink bottle effect' induced by the differences in pore sizes of soils (Fredlund et al. 2012; Lu and Likos 2004). Besides, for one certain suction value, the degree of saturation S_r differs along different scanning curves. Therefore, the drying and wetting paths of the SWCC are separately measured in this study. However, for Tomakomai soil, the field SWCC may have experienced complicated drying and wetting cycles in history. To find the path closest to the current field condition, several scanning curves shown in Figure 3-4(b) are measured in this study to compare with the moisture condition of the field tests. More details about the SWCC and moisture conditions utilized in this study are explained in Section 3.3.3.



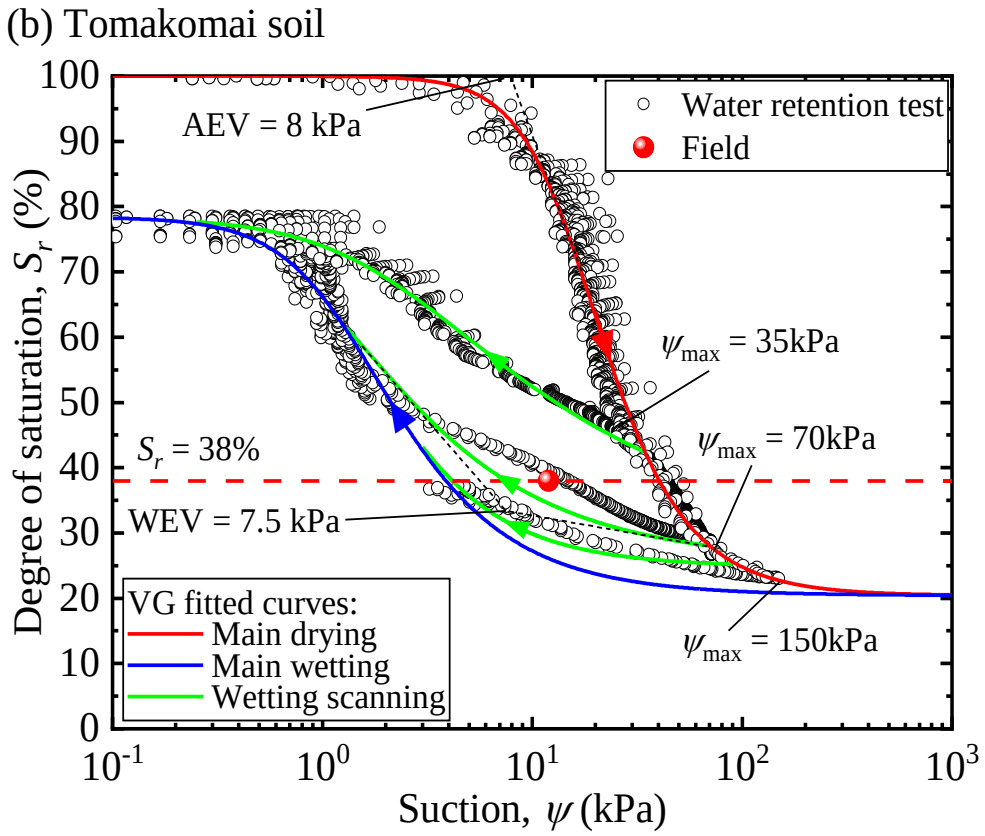


Figure 3-4 SWCC of test materials: (a) Toyoura sand; (b) Tomakomai soil

3.3 Resilient Modulus Test

3.3.1 Test sequence

The M_r tests in this study consist of five types under both saturated and unsaturated conditions: unfrozen test (hereinafter referred to as 'U test'), unfrozen wheel loading test (hereinafter referred to as 'UW test'), freeze-thaw test (hereinafter referred to as 'FT test'), Freeze-thaw-wheel loading test (hereinafter referred to as 'FTW test'), and Freeze-wheel loading-thaw test (hereinafter referred to as 'FWT test'), which are considered as the regular condition, condition after wheel loading, condition after freeze-thaw action, condition after freeze-thaw-wheel loading, and condition after freeze-wheel loading-thaw, respectively. Moreover, to investigate the effect of the suction hysteresis of SWCC, the unsaturated tests are divided into the drying path and the wetting path. The tests went through the following processes as shown in Table 3-2 after the specimen was saturated by applying a back pressure of 200kPa to reach a B value of greater than 0.96.

Table 3-2 Test sequence for M_r tests

	Consolidation process		Suction process	Freezing process		Wheel loading process		Thawing process		Wheel loading process		MR test	
U	→	○	→	○/×	→	×	→	×	→	×	→	×	→	○
UW	→	○	→	○/×	→	×	→	×	→	×	→	○	→	○
FT	→	○	→	○/×	→	○	→	×	→	○	→	×	→	○
FTW	→	○	→	○/×	→	○	→	×	→	○	→	○	→	○
FWT	→	○	→	○/×	→	○	→	○	→	○	→	×	→	○

Note: ○ means Applied this progress; × means Skipped this progress.

3.3.2 Cyclic loading condition

The loading steps were conducted referring to the AASHTO standard T307-99 (AASHTO 2017). Figure 3-5 shows the loading waves utilized in this study and in the AASHTO standard, where q_{max} is the maximum deviator stress applied to the specimen including the contact deviator stress and cyclic deviator stress in one cycle, q_{cont} is the contact deviator stress to maintain positive contact between the specimen cap and the specimen, and q_{cyclic} is the difference between q_{max} and q_{cont}. However, as shown in Figure 3-5 (a) and (b), the loading frequency in this study is 0.2 Hz due to the limitation of the test apparatus, which is different from the loading frequency of 10 Hz in the AASHTO standard. For the details, Lin et al. (2022) discussed the estimation of this limited loading frequency. However, since more study on the effect of loading frequency is necessary, the M_r results under the loading frequency of 0.2 Hz in this test are directly used without conversion. According to the AASHTO standard, there are 11 steps from MR-0 to MR-10. MR-0 is the pre-loading step to make sure the cap completely reaches the top end of the specimen. In this study, the loading number of MR-0 is determined as 2000 cycles to get a stable residual strain. Besides, since the maximum deviator stresses in MR-4, 5, 9, and 10 are larger than the field condition in Japan (Kishikawa et al. 2017), this study skips MR-4, 5, 9, and 10 and inserts MR-1.5, 2.5, 6.5, and 7.5 to keep the total number of loading steps as 11. To obtain accurate M_r values, the average deformation of the last 5 cycles in 100 repetitions of the cyclic axial stress is recorded. Table 3-3 shows the detailed loading steps and conditions in this study. It is noted that the σ_c in Table 3-3 is defined as the effective stress, that is, the

total confining stress should be plus 200 kPa based on the initial pore water pressure as explained in Section 3.3.1.

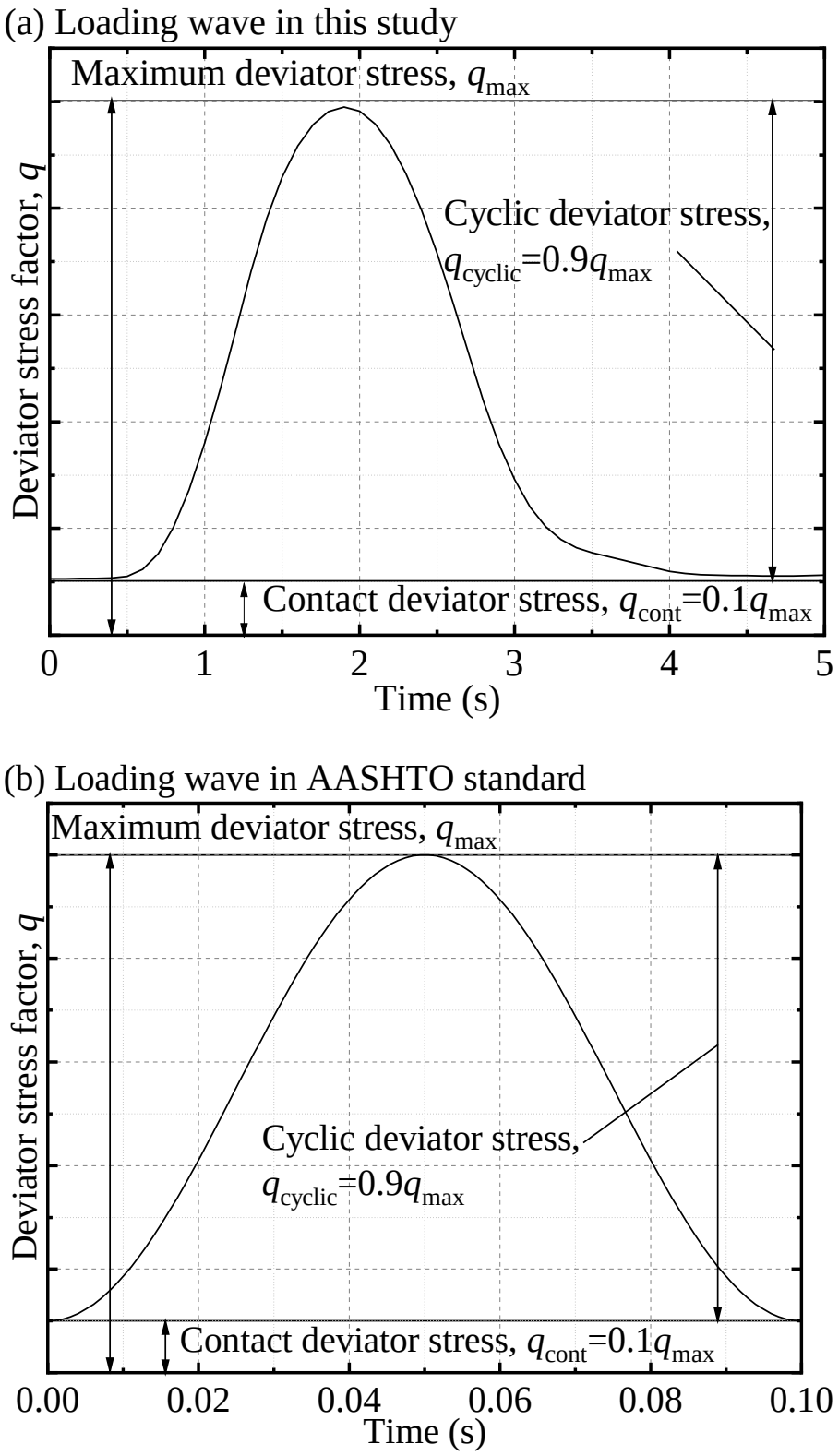


Figure 3-5 Loading waves in one cycle: (a) This study; (b) AASHTO standard

Table 3-3 Loading steps in M_r tests

	σ_c (kPa)	q_{max} (kPa)	q_{cont} (kPa)	q_{cyclic} (kPa)	N_c
MR-0	41.4	27.6	2.76	24.84	2000
MR-1	41.4	13.8	1.38	12.42	100
MR-1.5	41.4	20.7	2.07	18.63	100
MR-2	41.4	27.6	2.76	24.84	100
MR-2.5	41.4	34.5	3.45	31.05	100
MR-3	41.4	41.4	4.14	37.26	100
MR-6	27.6	13.8	1.38	12.42	100
MR-6.5	27.6	20.7	2.07	18.63	100
MR-7	27.6	27.6	2.76	24.84	100
MR-7.5	27.6	34.5	3.45	31.05	100
MR-8	27.6	41.4	4.14	37.26	100

Note: σ_c is confining pressure; N_c is the number of loading cycles.

3.3.3 Moisture condition

According to the long-term field measurement data (Ishikawa et al. 2019), the average S_r of the subgrade soil is 38%. Furthermore, by calculating the corresponding suction of the base course (C-40), the estimated groundwater level at the site is approximately 2 m (Lin et al. 2021). Considering the thickness of the pavement surface and base course layers, the suction at the subgrade soil surface is approximately 12 kPa. For Tomakomai soil, it can be found that the wetting scanning curve with the maximum suction $\psi_{\max}$ of 70 kPa agrees well with the field condition as shown in Figure 3-4(b). As a result, this curve is employed in this study to represent the wetting SWCC of the Tomakomai soil. For Toyoura sand, the main drying and main wetting paths are used because the SWCC reaches the residual state when $\psi_{\max}$ = 8 kPa based on the fitting by the VG model (VanGenuchten 1980). In this case, ψ = 3.75 kPa corresponding to S_r = 38% along the drying path is selected as the field condition for Toyoura sand to keep the consistency of the previous study (Lin et al. 2022).

By utilizing the axis translation technique, a specific suction can be obtained and maintained during the unsaturated triaxial tests. As mentioned in Section 3.3.1, since the initial pore air and pore water pressure are 200 kPa after the specimen is saturated, the suction can be controlled by adjusting the pore water pressure to a certain value and

keeping the pore air pressure at 200 kPa. Furthermore, corresponding S_r and ψ along drying and wetting paths as shown in Table 3-4 are selected to investigate the effect of suction hysteresis on M_r. As a result, four groups of unsaturated U tests along both drying and wetting paths are conducted. It is noted that the difference of the S_r between the triaxial test and SWCC may be ± 2% ~ 4% due to the random error and the different apparatus. Additionally, it is noted that only the smaller suction values (Toyoura sand: 3.75 kPa; Tomakomai soil: 15 kPa) along the drying and wetting paths were adopted for other moisture conditions besides U tests.

Table 3-4 S_r and ψ used to investigate the effect of suction hysteresis

	ψ (kPa)	S_r (%)	Path
Toyoura sand	3.75	38	Drying
		10	Wetting
	6.10		Drying
		6	Wetting
Tomakomai soil	15	75	Drying
		38	Wetting
	50		Drying
		28	Wetting

3.3.4 Wheel loading condition

The wheel loading condition in the UW, FTW, and FWT tests and the temperature condition in the FT, FTW, and FWT tests of the previous study (Lin et al. 2022) were adopted in this study. As shown in Figure 3-6, the wheel load on the subgrade layer is caused by a 49-kN wheel load on a typical pavement structure in the Japanese design guide (Japan Road Association 2019). When applying the standard 49-kN wheel load to the surface of the pavement, the stress transmitted to the surface of the subgrade is the cyclic deviatoric stress q_{cyclic} that should be applied in the wheel-loading process in the experiment, while the stress caused by the gravity of the pavement structure above the subgrade is the constant deviatoric stress q_{cont}. The cyclic deviatoric stress caused by the wheel load was calculated by the General Analysis of Multi-layered Elastic Systems (GAMES), a software to analyze the stress and strain in multi-layered pavements developed by Maina and Matsui (2004). As for the boundary conditions, the bottom is set as a fixed constraint boundary, while the left and right sides are set as

roller constraint boundaries, respectively. Because the subgrade layer is a semi-infinite body where the distal strain of the bottom should converge to zero, while the left and the right sides of the whole pavement structure are also infinite where the horizontal distal strain should converge to zero but free in the vertical direction. q_{cont} and q_{cyclic} were determined as 9.6 and 26.2 kPa in the thawing season, and 9.6 and 24.5 kPa in the frozen season. The loading frequency and waveform were the same as in the M_r test, and the loading number was 1000.

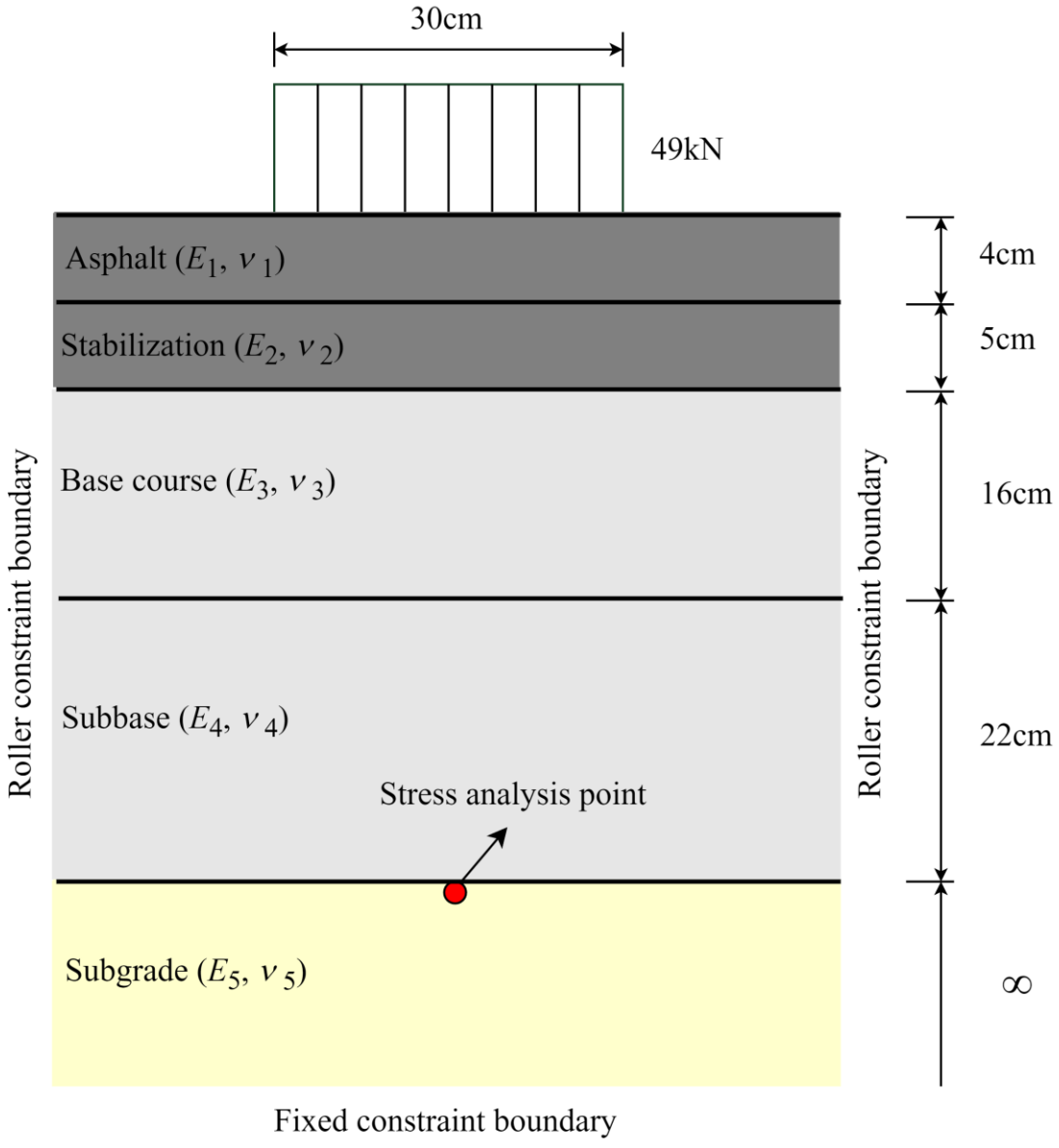


Figure 3-6 Pavement structure and wheel loading condition

3.3.5 Temperature condition

According to the Japanese standard JGS 0172 (Japanese Geotechnical Society 2018), a one-dimensional freeze-thaw action was conducted in an open system with axial stress of 10 kPa for the FT, FTW, and FWT tests. The temperature change of the specimen cap and pedestal in the freeze-thaw process is shown in Figure 3-7. The specimen is frozen at a temperature drop rate of 1.64 ℃/hour as in the previous study (Lin et al. 2022). After the frozen state is maintained for 5 hours, the specimen is thawed by increasing the temperature of the cap and pedestal at a rate of 1.64 ℃/hour. In this study, the temperature gradient in the specimen is kept constant by controlling the temperature of both the cap and pedestal, enabling open freezing that allows water supply and drainage during freezing and thawing. However, confining pressure is required when applying the wheel load during the FWT test, but the L-T bath (C) cannot be used simultaneously with the confining pressure due to the apparatus structure. Therefore, the temperatures of both the specimen cap and pedestal are controlled at -5 ℃, and the surrounding temperature of the specimen is maintained by a copper pipe around the specimen as shown in Figure 3-8 during the wheel loading process in the FWT test.

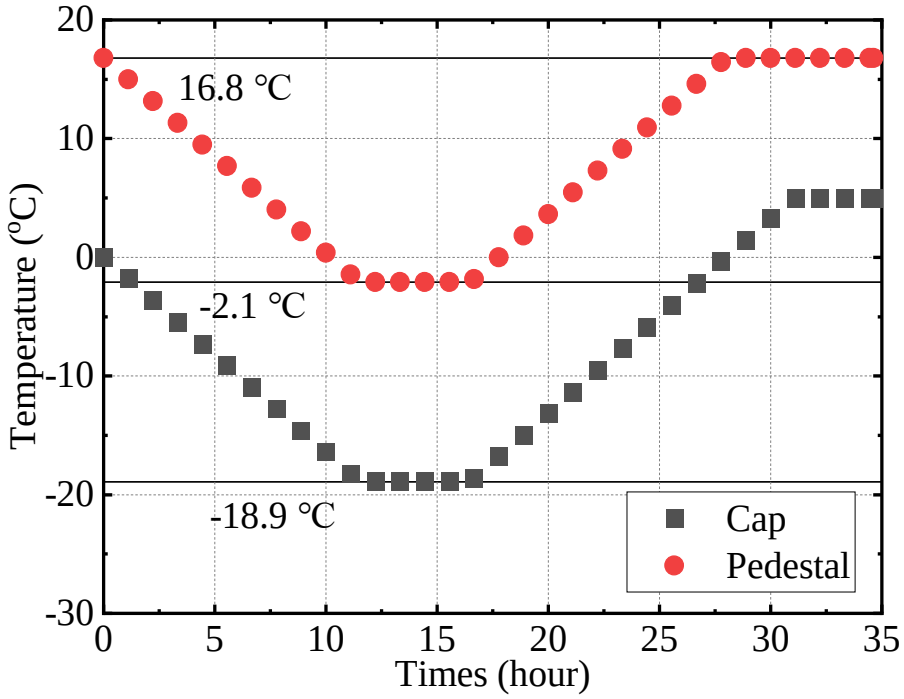


Figure 3-7 Temperature change in the freeze-thaw process

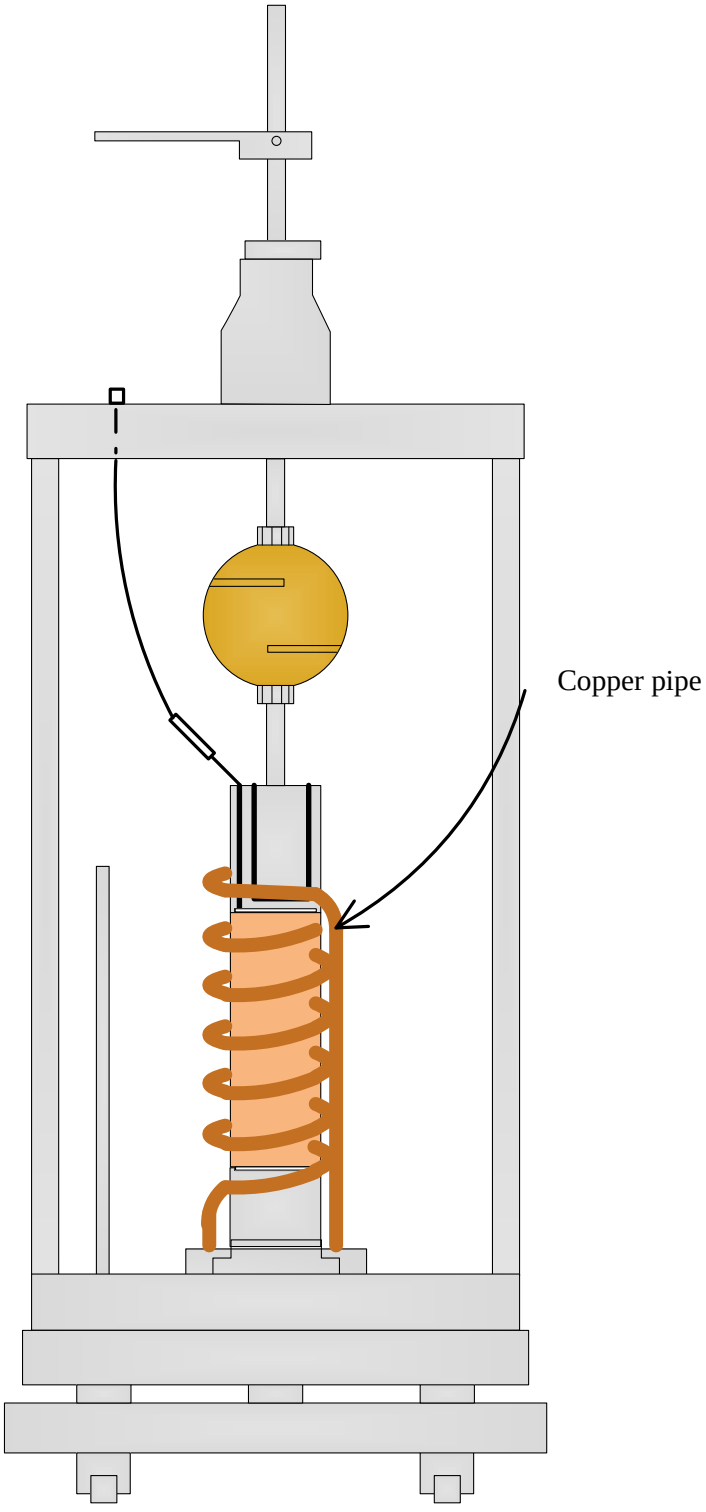


Figure 3-8 Copper pipe used during the wheel loading process in the FWT test

4 EFFECTS OF CLIMATIC AND WHEEL LOADING CONDITIONS ON RESILIENT MODULUS

4.1 Results of Resilient Modulus Tests

By conducting the M_r tests under different moisture, temperature, and wheel loading conditions using the unsaturated freeze-thaw cyclic loading triaxial apparatus, the resilient moduli under complex climatic and wheel loading conditions can be obtained. As explained in the test sequence in Chapter 3, the U tests, UW tests, FT tests, FTW tests, and FTW tests correspond to the normal season without wheel loading, wheel loading during normal season, thawing season without wheel loading, wheel loading during thawing season, and wheel loading during frozen season, respectively. All tests are conducted under different moisture conditions including saturated, unsaturated drying path, and unsaturated wetting path to parallelly investigate the effect of degree of saturation and suction hysteresis. Figure 4-1 to Figure 4-5 show the measured resilient moduli of the saturated and unsaturated conditions under different degrees of saturation S_r and matric suction ψ for the U tests, UW tests, FT tests, FTW tests, and FWT tests, respectively. The X-axis is the peak deviator stress applied to the specimen during the loading process, the Y-axis is the confining pressure, and the Z-axis is the measured M_r. To compare the test results and analyze the effects under different climatic and wheel load conditions, all the test results are fitted by regression analysis through Lin's climatic Ng model shown in Equation 1-6. It can be found that generally, M_r increases with the increment of the confining pressure and the matric suction but decreases with the increment of the deviator stress. For different temperature conditions, the freeze-thaw action generally decreases the M_r of the materials due to the deformation of the soil skeleton by the frost heave. Furthermore, the effect of the wheel loading process during the normal season and the thawing season is more complicated because the change of M_r may differ in different materials. More details about the effects of the suction, freeze-thaw, and wheel load conditions will be discussed in the later sections.

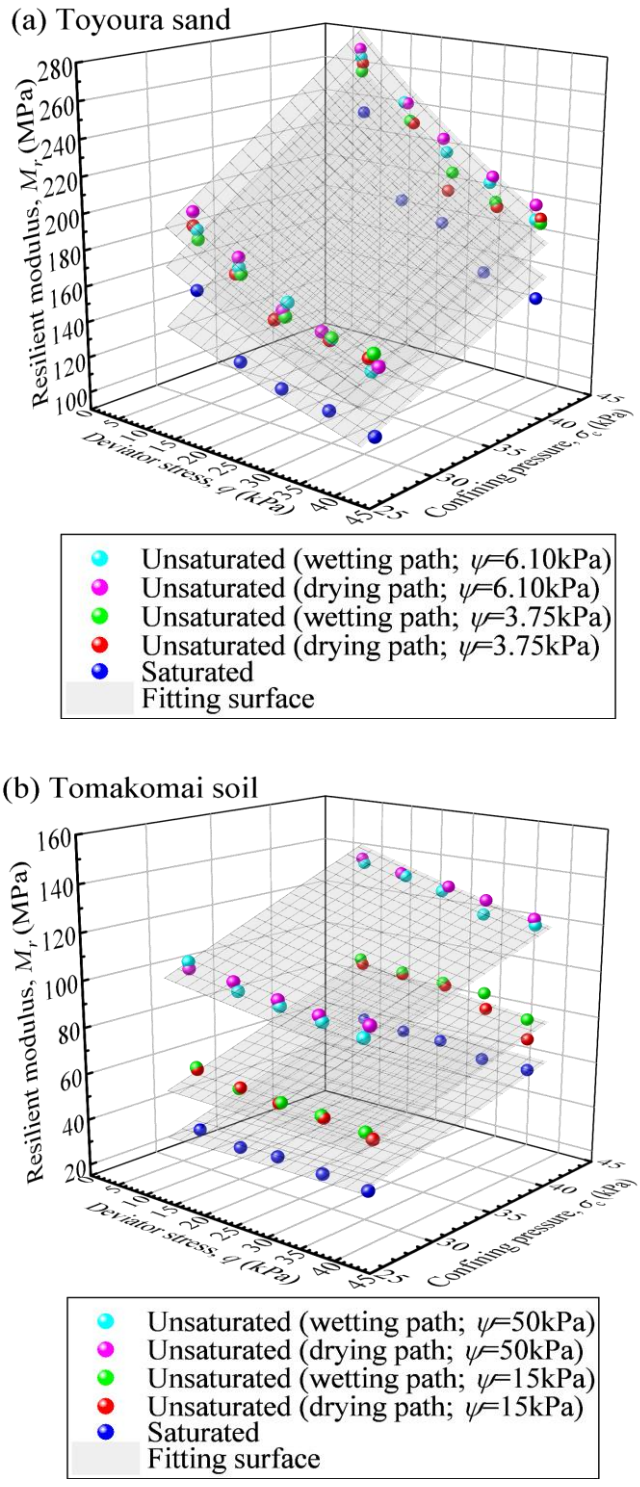


Figure 4-1 Results of U tests: (a) Toyoura sand; (b) Tomakomai soil

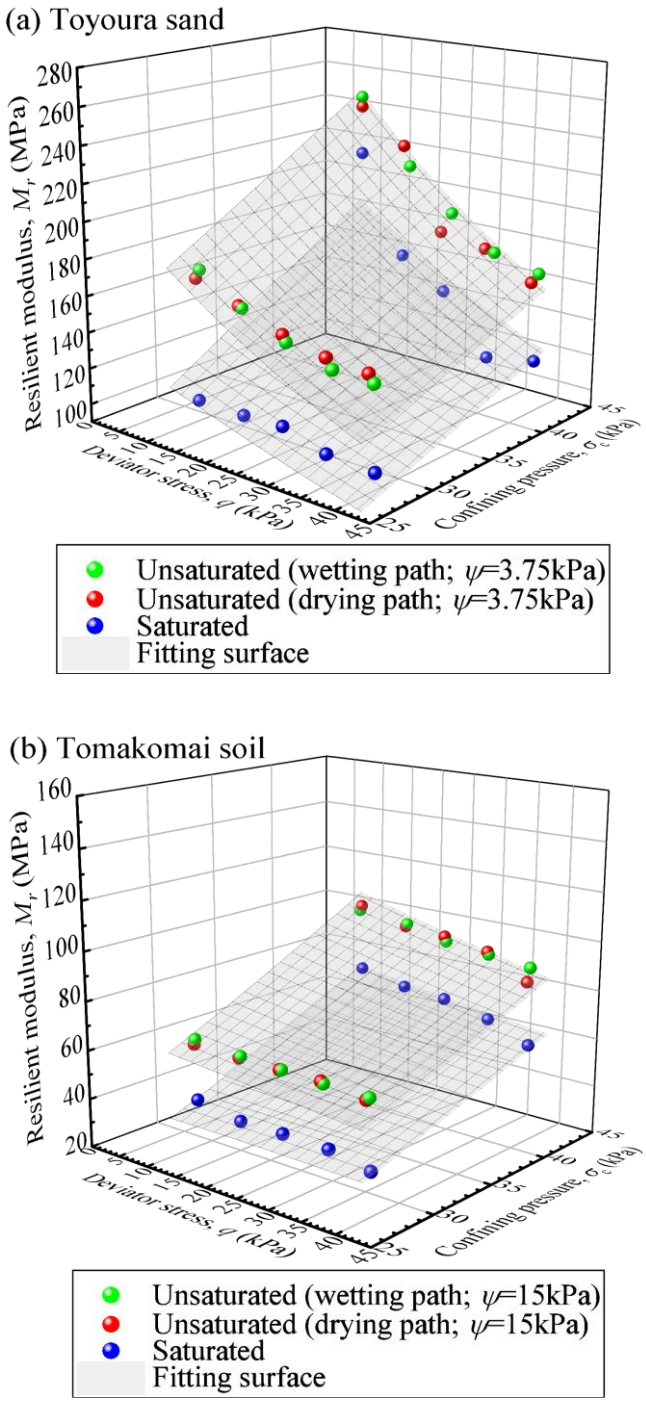


Figure 4-2 Results of UW tests: (a) Toyoura sand; (b) Tomakomai soil

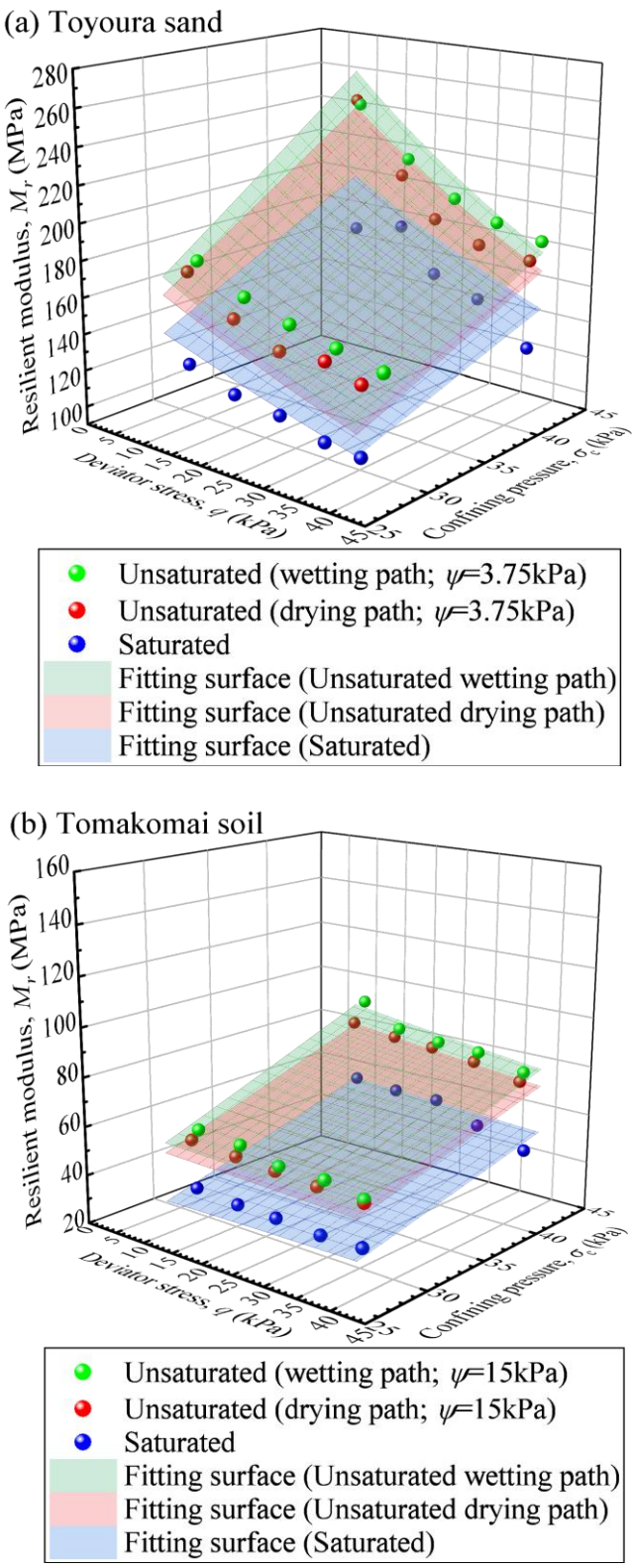


Figure 4-3 Results of FT tests: (a) Toyoura sand; (b) Tomakomai soil

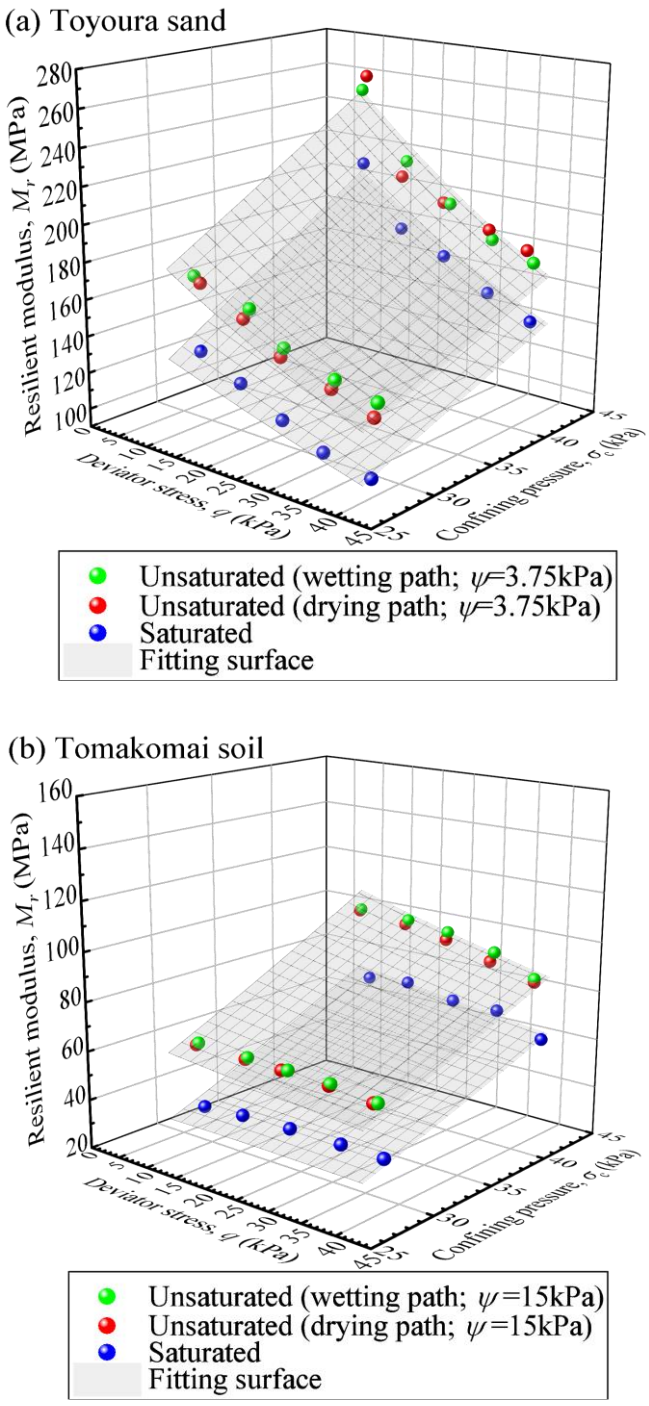


Figure 4-4 Results of FTW tests: (a) Toyoura sand; (b) Tomakomai soil

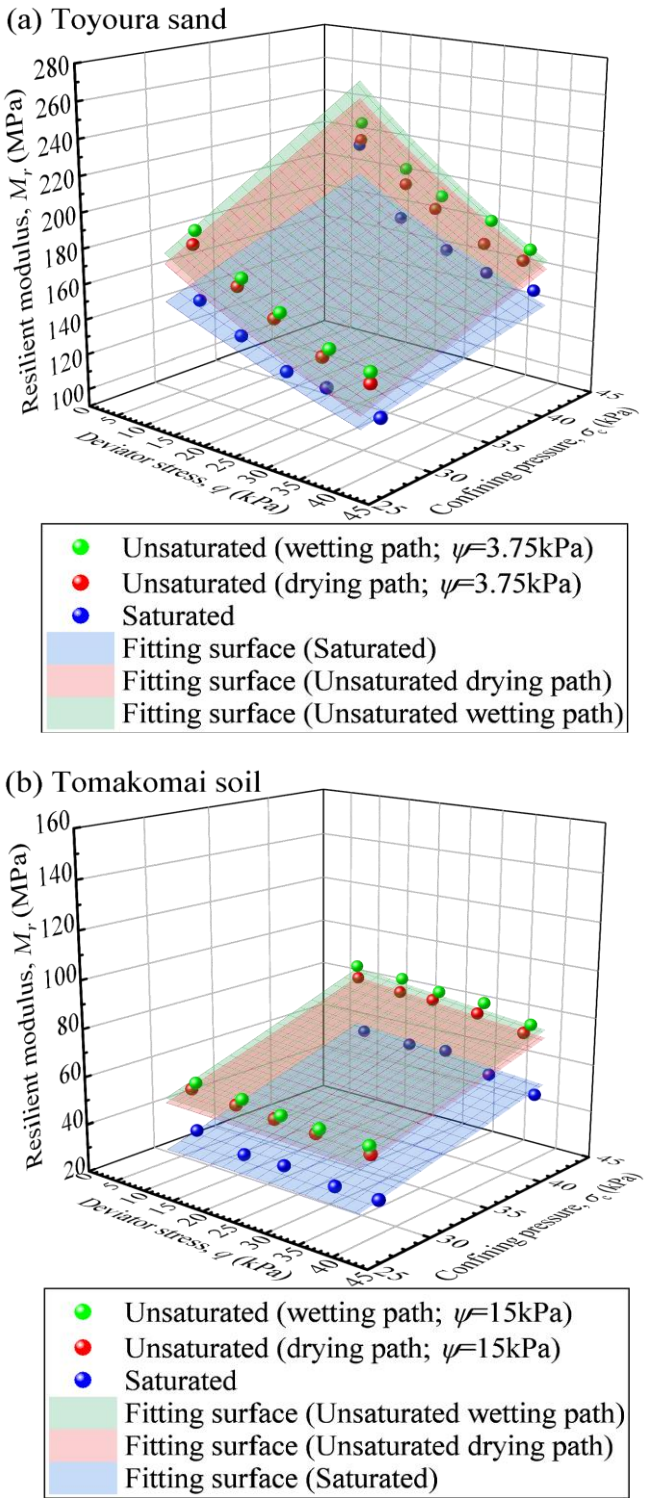


Figure 4-5 Results of FWT tests: (a) Toyoura sand; (b) Tomakomai soil

4.2 Effect of Matric Suction

To compare the test results and discuss the effects under different matric suction values ψ and degrees of saturation S_r, the test results are fitted by regression analysis

through Lin's climatic Ng model shown in Equation 1-6. When the climatic factor F_{clim} is equal to 1, the form of Lin's climatic Ng model becomes the same as the original Ng model. That is, Lin's climatic Ng model is equivalent to the original Ng model when applied to the normal season. It should be noted that all the test results under different suction values are fitted together so that one set of parameters could represent various moisture conditions. Taking the U tests as an example here, the test results with fitting surfaces and parameters of regression analysis are shown in Figure 4-1 and Table 4-1, respectively. It can be found that although the degrees of saturation under the same matric suction differ along the drying and wetting paths, the measured resilient moduli are very close. That is, the resilient moduli along the drying and wetting paths can be fitted together with respect to the same matric suction. This is also consistent with the fact that the Ng model only considers the matric suction ψ but not the degree of saturation S_r as the parameter to predict the resilient modulus of partly saturated soils (Ng et al. 2013). For most of the unsaturated conditions during the normal season, the Ng model can predict the M_r well because the range of changes in matric suction is relatively small. However, it is also known that not only the matric suction but also the moisture content affects the strength of unsaturated soils, especially when the moisture content is significantly low. More details about the comprehensive effect of moisture content and matric suction will be discussed in the next chapter.

Table 4-1 Regression analysis results of U tests

	F_{clim}	k_1	k_2	k_3	k_4	R^2
Toyoura sand	1	2.089	1.057	-4.437	1.692	0.948
Tomakomai soil	1	0.526	1.293	-2.650	1.008	0.988

4.3 Effect of Wheel Load

4.3.1 Effect of wheel load on moisture change

To discuss the effect of traffic load on the different results in Toyoura sand and Tomakomai soil, the water drainage that reflects the volumetric change of the soil sample during the wheel loading process is recorded. Figure 4-6 plots the water drainage after every loading cycle during the wheel loading process for Toyoura sand and Tomakomai soil. It can be found that the water drainage curves are close to typical consolidation curves, and the amount of water drainage differs in different materials

and different moisture conditions. The overall water drainage of Tomakomai soil is greater than that of Toyoura sand. This is because the plastic deformation of Toyoura sand is greater than that of Tomakomai soil due to the greater overall stiffness of Toyoura sand than that of Tomakomai soil. For different moisture conditions in both Toyoura sand and Tomakomai soil, the water drainage tends to be greater when the water content is greater. In the case of Tomakomai soil, for example, the water drainage of the saturated condition is the highest, that of the unsaturated drying path with low water content is lower, and that of the unsaturated wetting path with the lowest water content is the lowest. It is similar in the case of Toyoura sand but the water drainage under the unsaturated conditions is not significant because the overall water drainage of Toyoura sand is relatively small compared with Tomakomai soil.

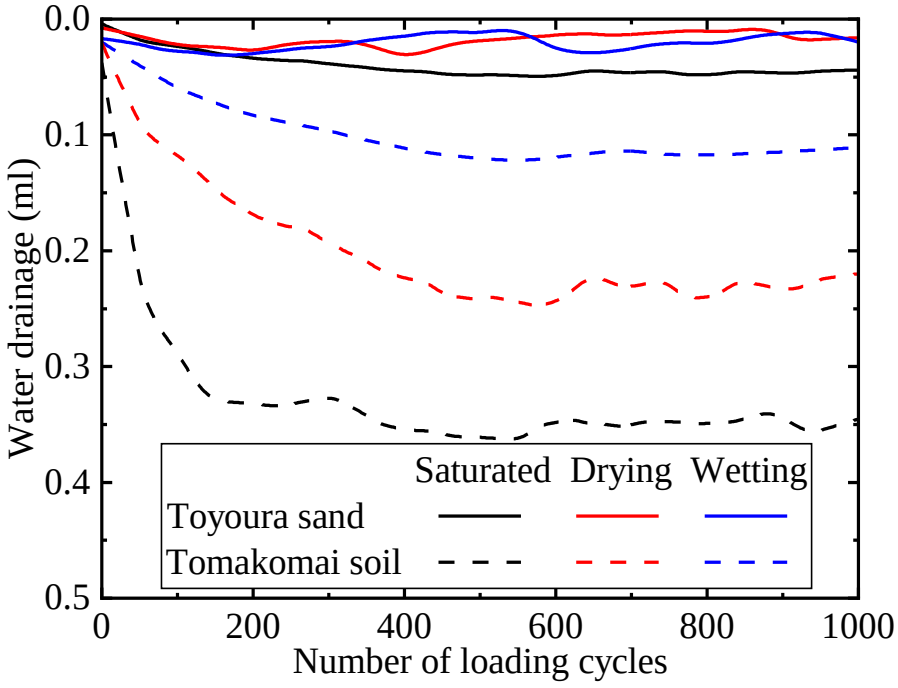


Figure 4-6 Water drainage during the wheel loading process (UW test)

Table 4-2 Water content and density change by wheel load

	Moisture condition	Water drainage (ml)	Water content change ratio (%)	Density change ratio (%)
Toyoura sand	Saturated	0.040	0.015	0.0061
	Drying path	0.009	0.015	0.0014
	Wetting path	0.003	0.073	0.0005
Tomakomai soil	Saturated	0.308	0.098	0.0471
	Drying path	0.199	0.083	0.0304
	Wetting path	0.091	0.091	0.0139

4.3.2 Effect of wheel load on resilient modulus

Similar to the results of the U tests, the results of the UW tests with Lin's climatic Ng model fitted surfaces and parameters of regression analysis are shown in Figure 4-2 and Table 4-3, respectively. To compare the resilient moduli of the U test and UW test, the resilient moduli of the UW/U test for both Toyoura sand and Tomakomai soil are shown in Figure 4-7. It can be found that all the plots of the Toyoura sand are below the 1:1 line but those of the Tomakomai soil are upon the 1:1 line, which indicates that the wheel loading process may increase the M_r of the Tomakomai soil but decreases that of the Toyoura sand.

To explain the reason for the difference in the effect of wheel load on Toyoura sand and Tomakomai soil, the axial strain and M_r during the 1000-cycle wheel loading process are investigated. Table 4-4 shows the average resilient strains and resilient moduli in the initial and final 100 cycles during the wheel loading process. It can be found that the resilient strain changes after the 1000-cycle wheel loading process and directly causes the changes in M_r according to the definition of M_r. In the case of Toyoura sand, the increment in resilient strain causes the decrement of M_r for 9.30% ~ 18.86%. On the contrary, the decrement in resilient strain in Tomakomai soil causes the increment of M_r for 3.74% ~ 7.47%. The possible reason for that is the difference in fine fraction content. Since Toyoura sand is much more poorly graded than Tomakomai soil as shown in Figure 3-2, the soil skeleton may be disturbed by the wheel loading process due to the lack of fine fraction, which leads to a decrement of the resilient modulus. This kind of decrement in resilient modulus caused by wheel loads is also

explained as the disturbance of soil particle skeleton structure uniformity by Lin et al. (2022).

Table 4-3 Regression analysis results of UW tests

	F_{clim}	k_1	k_2	k_3	k_4	R^2
Toyoura sand	1	1.750	1.088	-4.916	3.639	0.905
Tomakomai soil	1	0.568	1.541	-3.658	1.258	0.985

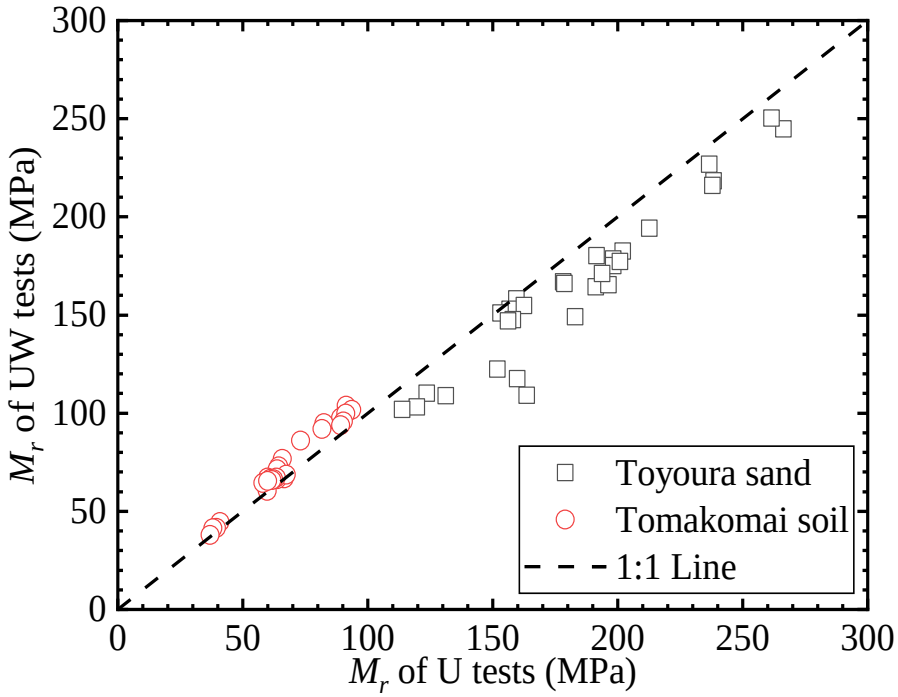


Figure 4-7 Resilient modulus ratio of UW/U tests

Table 4-4 Resilient strain and M_r change during the wheel loading process

	Moisture condition	$(\varepsilon_a)_r^i$ (%)	M_r^i (MPa)	$(\varepsilon_a)_r^f$ (%)	M_r^f (MPa)	Change ratio of Mr (%)
Toyoura sand	Saturated	0.0175	204.92	0.0208	172.41	18.86
	Drying path	0.0152	235.89	0.0166	215.82	9.30
	Wetting path	0.0153	234.08	0.0169	211.32	10.77
Tomakomai soil	Saturated	0.0544	65.87	0.0503	71.18	-7.47
	Drying path	0.0472	75.79	0.0455	78.73	-3.74
	Wetting path	0.0476	75.23	0.0449	79.66	-5.56

Note: $(\varepsilon_a)_r^i$, $(\varepsilon_a)_r^f$ are average resilient strains in the initial/final 100 cycles; M_r^i, M_r^i are average resilient moduli in the initial/final 100 cycles.

4.4 Effect of Freeze-thaw

4.4.1 Effect of freeze-thaw on moisture change and frost heave

Figure 4-8 shows the water drainage and frost heave during the freeze-thaw process. From Figure 4-8, it can be found that although the water content changes during the freeze-thaw process, especially in the saturated specimens, the final change returns to approximately zero. In the unsaturated tests along drying and wetting paths, the change in the water during the freeze-thaw process is not significant because the water content of the specimen is small. It is noted that the water drainage cannot directly reflect the volumetric change of the specimen during freeze-thaw because of the phase change of water. During the freeze-thaw process, the change in height can directly reflect the volumetric change because the lateral direction is constrained. Table 4-5 shows the change in specimen height and density by freeze-thaw compared to the initial states. The density change caused by the freeze-thaw action of Tomakomai soil is more significant than Toyoura sand and also affected by the water content. In general, the change in the water content caused by the freeze-thaw is negligible. However, the frost heave is significantly affected by the initial water content. In the case of the saturated condition, the specimen had a significant frost heave and absorbed or drained water during the freezing process and finally had a residual axial displacement, which indicates that the frost heave phenomenon is significant. On the other hand, in the case of unsaturated conditions, especially in the case of the wetting path, the frost heave is not obvious compared with the saturated one. This is because the volume of the water to be frozen decreases with the decrement of the S_r, which weakens the effect of frost heave.

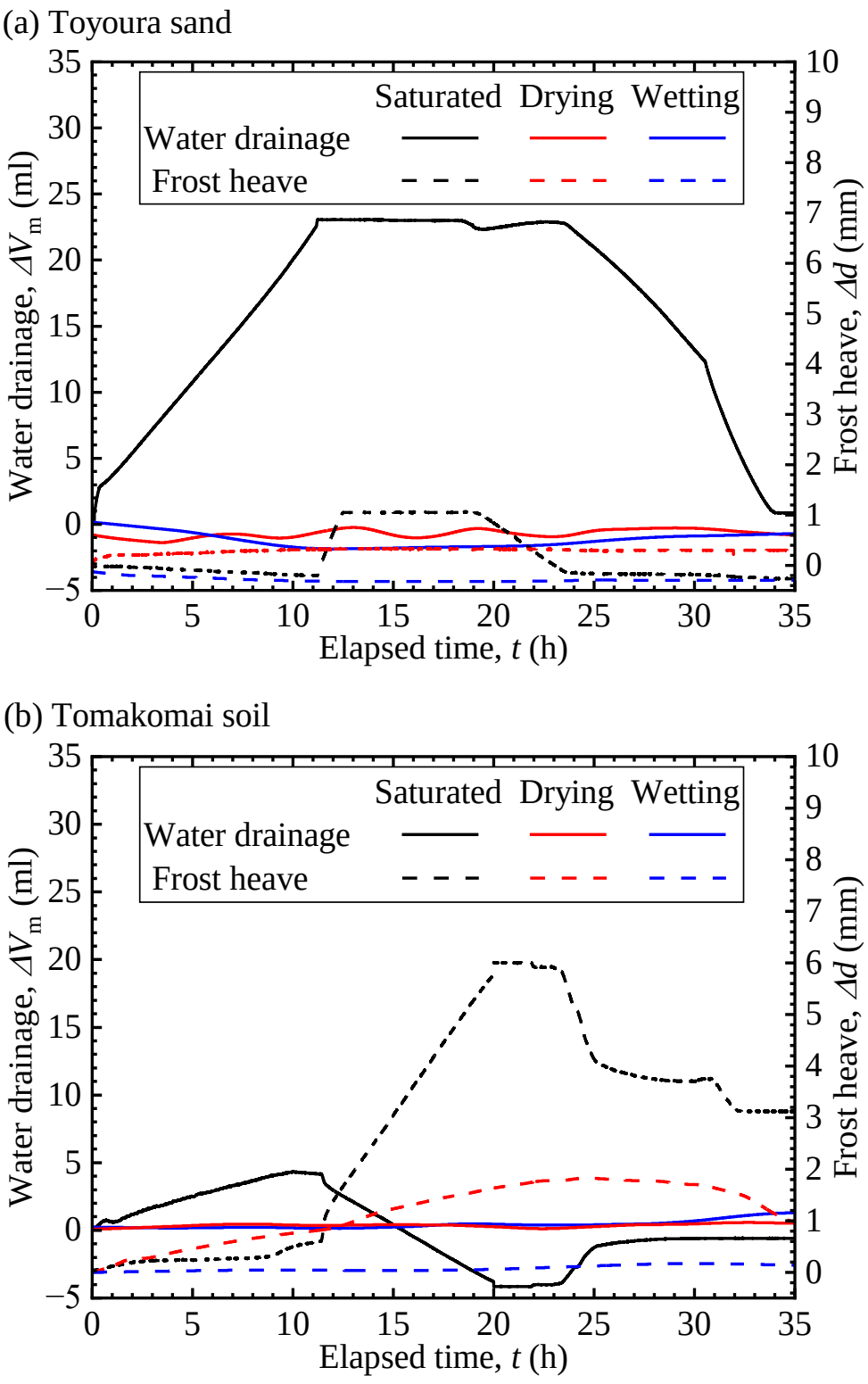


Figure 4-8 Water drainage and frost heave during the freeze-thaw process (FT test): (a) Toyoura sand; (b) Tomakomai soil

Table 4-5 Density change after freeze-thaw action

	Moisture condition	Degree of saturation (%)	Height change (mm)	Density change ratio (%)
Toyoura sand	Saturated	38	-0.28	0.165
	Drying path	10	0.29	-0.170
	Wetting path	6	-0.17	0.100
Tomakomai soil	Saturated	75	3.12	-1.802
	Drying path	38	0.61	-0.358
	Wetting path	28	0.14	-0.082

4.4.2 Effect of freeze-thaw on resilient modulus

As shown in Figure 4-3, the results along the drying and wetting paths are significantly different in the case of FT tests. This is because different moisture contents, although the matric suction is the same, will cause different freeze-thaw effects, as shown in Figure 4-8, where it can be found that the frost heave decreases with the decrement of the water content. In addition, the frost susceptibility of Tomakomai soil is significantly greater than Toyoura sand. Therefore, the FT test results under different water contents and frost heave amounts are separately fitted by regression analysis using Lin's climatic Ng model. It is noted that to keep the consistency of the tests with and without the freeze-thaw process, the FT test utilized the same regression parameters of k_1 to k_4 as the U test. Table 4-6 shows the regression analysis results of FT tests for Toyoura sand and Tomakomai soil. As shown in Figure 4-9, it can be found that the freeze-thaw process generally decreases the M_r, which is obvious because the formation of ice disturbs the original soil skeleton. In the case of Toyoura sand, the decreasing ratio caused by the freeze-thaw action is 0.50% ~ 26.35%; in the case of Tomakomai soil, the decreasing ratio is 0.28% ~ 18.78%, and the decreasing rate is significantly affected by the water content. Furthermore, the parameter F_{clim} decreases with the decrement of moisture content and is affected by the water content, which also indicates that the effect of freeze-thaw action on resilient modulus is positively correlated with water content. As shown in Figure 4-8, the axial strain will increase, and the specimen will drain or absorb a certain amount of water during the freezing process. Meanwhile, the axial strain and the amount of absorbed water are also affected by the water content of the specimen. After thawing, the axial strain will decrease but not restore to the original height, which leads to a rearrangement of the soil skeleton. Furthermore, many researchers have observed changes in soil structure caused by freeze-thaw actions at

the microscopic level using methods such as X-ray (Leuther and Schlüter 2021; Starkloff et al. 2017; Wang et al. 2018). Although the frost heave differs a lot, the average decreasing rates of M_r of Toyoura sand and Tomakomai soil are 6.8% and 5.6%, respectively. The possible reason why the M_r of Toyoura sand has a greater decreasing rate than Tomakomai soil is that as a poorly graded sand, the soil skeleton of Toyoura sand is more susceptible to disturbance.

Table 4-6 Regression analysis results of FT tests

Material	Moisture condition		F_{clim}	k_1	k_2	k_3	k_4	R^2
Toyoura sand	Saturated		0.810	2.089	1.057	-4.437	1.692	0.941
	Unsaturated	Drying path	0.939	2.089	1.057	-4.437	1.692	0.928
		Wetting path	0.997	2.089	1.057	-4.437	1.692	0.876
Tomakomai soil	Saturated		0.908	0.526	1.293	-2.650	1.008	0.961
	Unsaturated	Drying path	0.962	0.526	1.293	-2.650	1.008	0.984
		Wetting path	0.992	0.526	1.293	-2.650	1.008	0.968

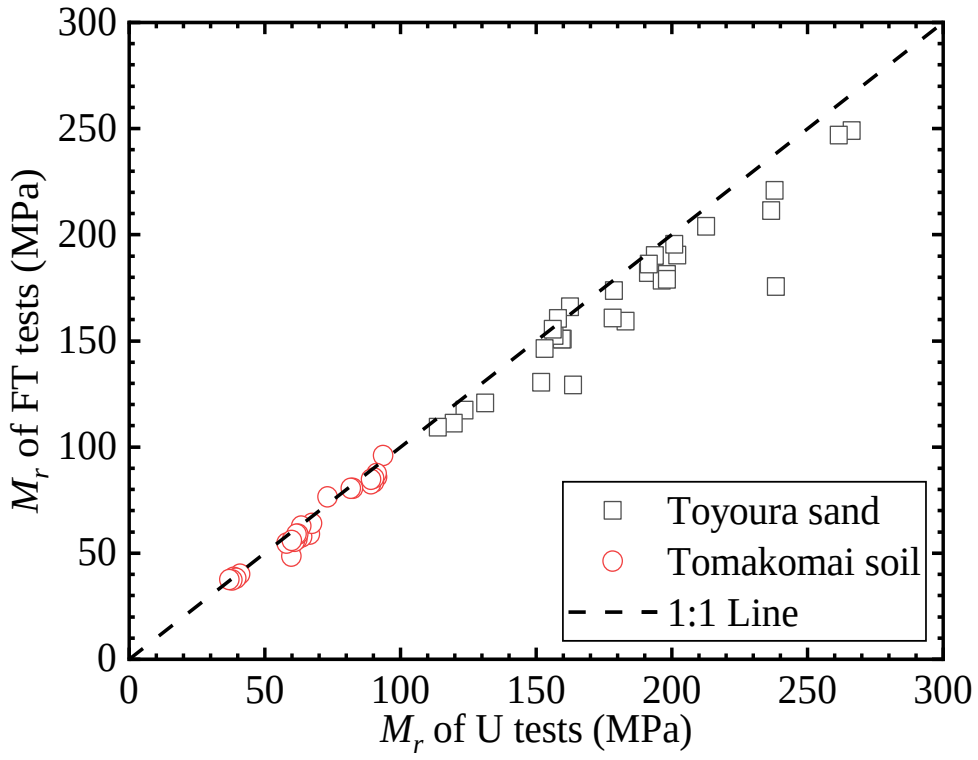
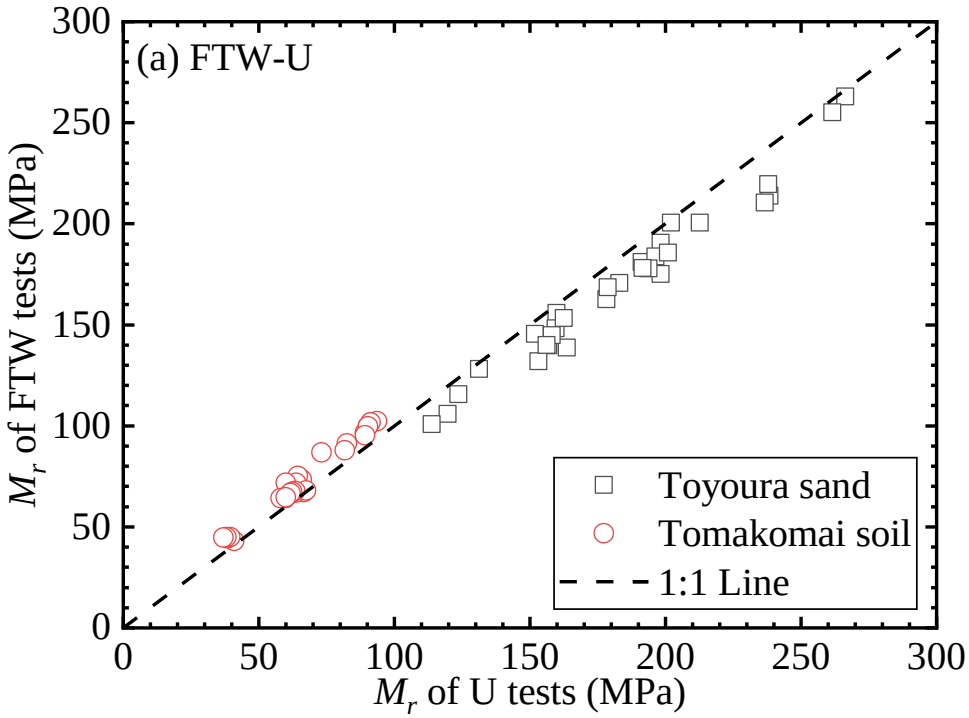


Figure 4-9 Resilient modulus ratio of FT/U tests

4.5 Effect of Combinations of Wheel Load and Freeze-thaw

4.5.1 Effect of wheel load after freeze-thaw

The results of FTW tests for Toyoura sand and Tomakomai soil are shown in Figure 4-4. Figure 4-10 shows the M_r ratio of FTW/U and FTW/UW, which indicates that there are certain relationships between the U/UW test and the FTW test. However, in the comparison between the FTW and U tests in Figure 4-10 (a), the plots of Toyoura sand and Tomakomai soil are located at different sides of the 1:1 line, making it difficult to determine whether the 'freeze-thaw-wheel loading' process increases or decreases the resilient modulus. On the other hand, in the comparison between the FTW and UW tests in Figure 4-10 (b), the 1:1 line is located at the center of the scatters of both Toyoura sand and Tomakomai soil, indicating that the results of FTW tests are close to the UW tests. The possible reason for this is similar to the UW test: the consolidation plays a leading role in increasing the resilient modulus after freeze-thaw in the case of Tomakomai soil, but the disturbance of the soil skeleton plays a leading role in decreasing the resilient modulus in the case of Toyoura sand.



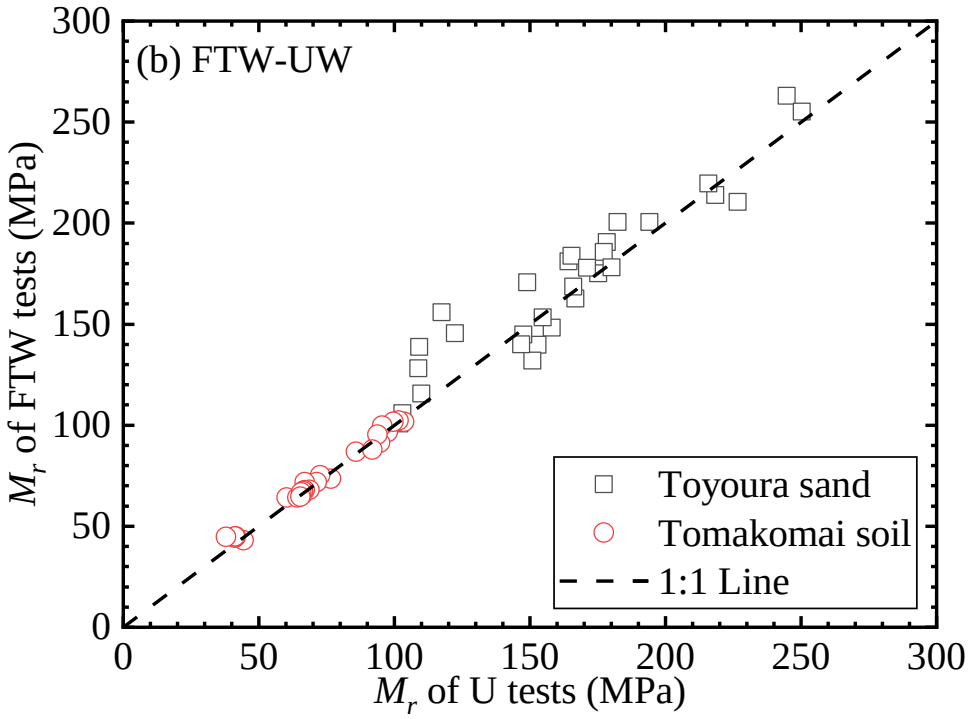


Figure 4-10 Resilient modulus ratio: (a) FTW/U tests; (b) FTW/UW tests

4.5.2 Effect of wheel load during frozen season

Figure 4-5 shows the results of FWT tests for Toyoura sand and Tomakomai soil. Compared with the results of FT tests shown in Figure 4-3, it can be found that the results of FWT tests and FT tests are nearly identical. As shown in Figure 4-11, the 1:1 line is located at the center of the scatters of both Toyoura sand and Tomakomai soil, also indicating that the resilient moduli of FWT and FT tests are similar. From these results, it can be inferred that the effect of the wheel loading process during the frozen season may be minimal because of the extremely high stiffness of the soil compared to normal seasons due to the freezing of water. Lin et al. (2022) have also compared the secant Young's moduli and axial strains of the frozen season and the thawing season during the wheel loading processes and found that the secant Young's modulus of the frozen season is far greater than that of the thawing season, whereas the permanent axial strain and the maximum axial strain of the frozen season are both far less than those of the thawing season.

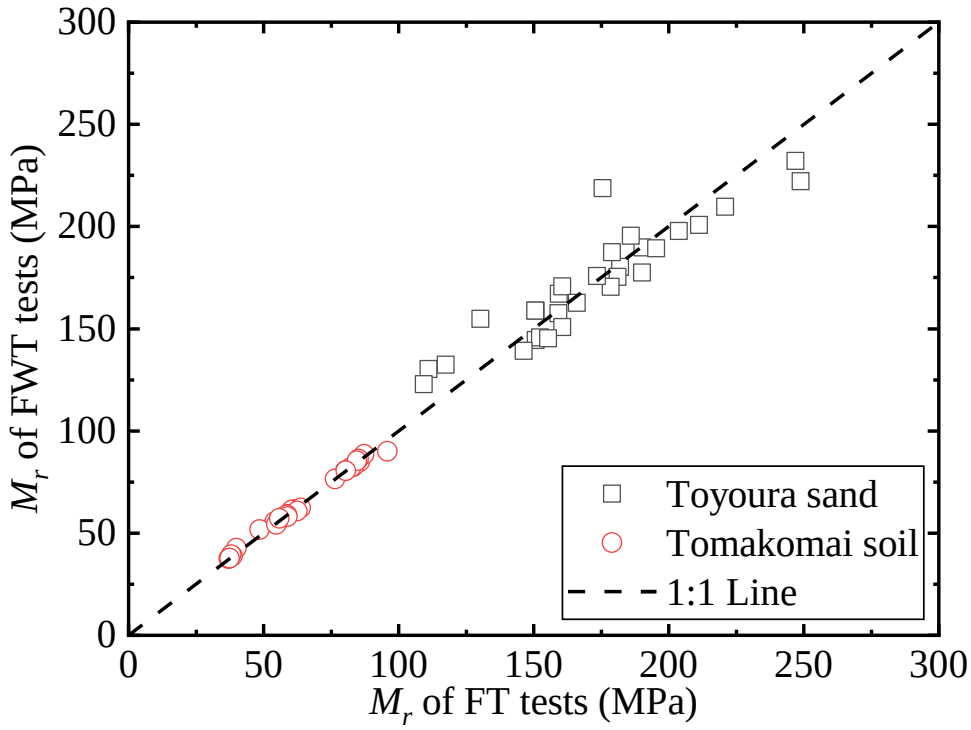


Figure 4-11 Resilient modulus ratio of FWT/FT tests

4.6 Summary

The resilient modulus of pavement subgrade soil in the site is affected by various factors such as moisture, freeze-thaw, and wheel loading conditions. By conducting the M_r tests under different moisture, temperature, and wheel loading conditions using the unsaturated freeze-thaw cyclic loading triaxial apparatus, the resilient moduli under complex climatic and wheel loading conditions can be obtained. According to the test results and discussions, the main findings of this chapter are as follows:

1. Generally, M_r increases with the increment of the confining pressure and the matric suction but decreases with the increment of the deviator stress. Although the degrees of saturation under the same matric suction differ along the drying and wetting paths, the measured resilient moduli are very close. That is, the resilient moduli along the drying and wetting paths can be fitted together for the same matric suction for most of the unsaturated conditions during the normal season unsaturated conditions during the normal season because the range of changes in matric suction is relatively small. However, since the moisture content also affects the strength of unsaturated soils, especially when the moisture content is

significantly low, more details about the comprehensive effect of moisture content and matric suction will be discussed in the next chapter.

2. During the normal season, the effect of wheel load may differ in different materials. The UW test results indicate that the wheel loading process may increase the M_r of the Tomakomai soil by 3.74% ~ 7.47% but decrease that of the Toyoura sand by 9.30% ~ 18.86%. In the case of Tomakomai soil, the decrement of the resilient strain increases the soil strength, which leads to an increment in the M_r. However, the resilient strain of Toyoura sand during the wheel loading process increases, which indicates that the wheel loads lead to a decrement in the M_r. Furthermore, since Toyoura sand is much more poorly graded, the soil skeleton may be disturbed by the wheel loading process due to the lack of fine fraction, which leads to a decrement of the M_r.

3. During the thawing season, since although the matric suction is the same, different moisture contents will cause different freeze-thaw effects, the M_r along the drying and wetting paths are significantly different. The freeze-thaw process generally decreases the M_r by 0.50% ~ 26.35% in the case of Tomakomai soil and by 0.28% ~ 18.78% in the case of Toyoura sand, which is obvious because the formation of ice disturbs the original soil skeleton. Furthermore, the effect of freeze-thaw action on resilient modulus is positively correlated with moisture content. Although the frost heave differs a lot, the average decreasing rates of M_r of Toyoura sand and Tomakomai soil are 6.8% and 5.6%, respectively, with no significant difference. It also indicates that the greatest harm of the freeze-thaw action to frost-susceptible soils is the structural damage to the pavement due to the significant frost heave.

4. The effect of combinations of freeze-thaw action and wheel load is more complicated, which comprehensively depends on the wheel loading sequence and material properties. On the one hand, the results of FTW tests are close to the UW tests. The possible reason is similar to the UW test: the consolidation plays a leading role in increasing the resilient modulus after freeze-thaw in the case of Tomakomai soil, but the disturbance of the soil skeleton plays a leading role in decreasing the resilient modulus in the case of Toyoura sand. On the other hand, the results of FWT and FT tests are similar. It can be inferred that the effect of the wheel loading process during the frozen season may be minimal because of the extremely high stiffness of the soil compared to normal seasons due to the freezing

of water. Therefore, using the same predicting parameters as the UW tests for FTW tests and the same predicting parameters as the FT tests for FWT tests is reasonable.

5 EFFECTS OF SUCTION STRESS ON RESILIENT MODULUS

5.1 Effect of Suction Hysteresis of SWCC

Although the Ng model focuses on matric suction as the main factor controlling the M_r in varying moisture conditions, it is confirmed that other factors such as water content can also have an impact on M_r to some degree. In fact, the test results of Ng et al. (2013) also demonstrated that the M_r along the wetting path is slightly greater than that along the drying path, even under the same matric suction. Khoury et al. (2011) obtained similar results and believed that the hardening by cyclic suction and the possible water lubrication may be the dominant reason for this difference in drying and wetting paths. Elkady et al. (2017) observed a positive influence of suction on the resilient characteristics of lime-treated specimens under a particular threshold suction magnitude, beyond which the effect of suction is deemed to be negligible. The abovementioned phenomena can be further explained using Bishop's principle of effective stress and the principle of suction stress (Bishop 1959; Lu and Griffiths 2004; Lu and Likos 2006). Suction stress σ_s is narrowly defined as the product of Bishop's effective stress factor χ and matric suction ψ, which can simultaneously reflect the effect of the water content and matric suction under various moisture conditions. Subsequently, M_r predictive models suitable for different matric suction and degrees of saturation can be further derived. According to Bishop's principle of effective stress, the effective stress in saturated and partly saturated soils is expressed in the following form as shown in Equation 5-1 (Bishop 1959):

$$\sigma' = (\sigma - u_a) + \chi(u_a - u_w) = (\sigma - u_a) + \chi\psi \quad (5\text{-}1)$$

where σ' is effective stress; σ is total stress; χ is Bishop's coefficient of effective stress; u_a and u_w are pore air and pore water pressure. The (σ-u_a) is also defined as net normal stress, whereas the (u_a-u_w) is matric suction ψ. The coefficient of effective stress χ is a parameter that reflects the proportion of matric suction that contributes to effective stress in unsaturated soil and is dependent on the S_r for various soils. Moreover, it should be noted that the u_a terms can be eliminated because all the stress states in this research are equivalent to the stress state of u_a = 0 kPa based on the axis translation technique and effective stress principle.

5.2 Determination of Bishop's Effective Stress Factor

(Bishop and Blight 1963) obtained some nonlinear relationships between effective stress coefficient χ and degree of saturation S_r through experiments for failure strength of saturated and partly saturated soils. However, it is impossible to directly measure and is difficult to quantify the χ both experimentally and theoretically due to the macroscopic concept of the effective stress approach (Khalili and Khabbaz 1998; Lu and Griffiths 2004). Researchers proposed some χ estimation models in various forms (Karube et al. 1996; Khalili and Khabbaz 1998; Vanapalli et al. 1996), generally divided into water content-based type and suction ration-based type. Generally, the existing M_r predictive models incorporating Bishop's effective stress factor determine χ by different equations or directly by regression parameters and rarely discuss the application of different χ determining methods. Furthermore, most of them did not explain or verify the application to the wetting path of SWCC. To compare the applicability of different χ estimation models on different M_r predictive models, three χ estimation models will be employed and combined with three selected M_r predictive models in the following sections.

5.2.1 Vanapalli model

Vanapalli et al. (1996) proposed a χ estimation model based on the normalized volumetric water content, and Garven and Vanapalli (2006) further established a relationship between κ and plastic index I_p by the statistical method as shown in Equations 5-2.1 and 5-2.2, respectively:

$$\chi = \Theta^{\kappa} = \left(\frac{\theta}{\theta_s}\right)^{\kappa} \tag{5-2.1}$$

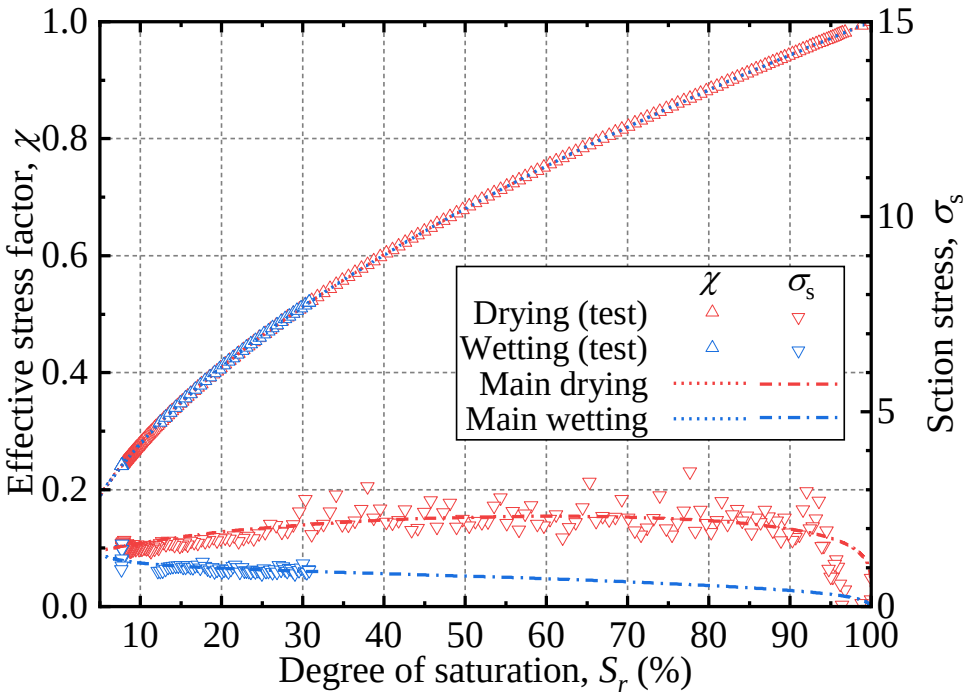
$$\kappa = -0.0016{I_p}^2 + 0.0975I_p + 1 \tag{5-2.2}$$

where Θ is normalized volumetric water content; θ is volumetric water content; θ_s is volumetric water content at a saturation of 100%; κ is a fitting parameter; and I_p is the plastic index.

It should be noted that the κ estimation is an area centered on the curve corresponding to Equation 5-2.2, with a 68% confidence interval. That is, the estimated value could be $\kappa \pm$ standard deviation. Since the Tomakomai soil and Toyoura sand are non-plastic with $I_p = 0$, a κ value of 0.555 to 1.445 can be applied to Equation 5-2.1.

Additionally, it is also found that the best-fit χ value is achieved when κ = 0.555 in this study. Therefore, a κ value of 0.555 is used in the later sections to discuss the applicability of this model. Based on the SWCCs as shown in Figure 3-4, the Variation of χ and σ_s with the S_r using the Vanapalli model can be obtained as shown in Figure 5-1.

(a) Toyoura sand



(b) Tomakomai soil

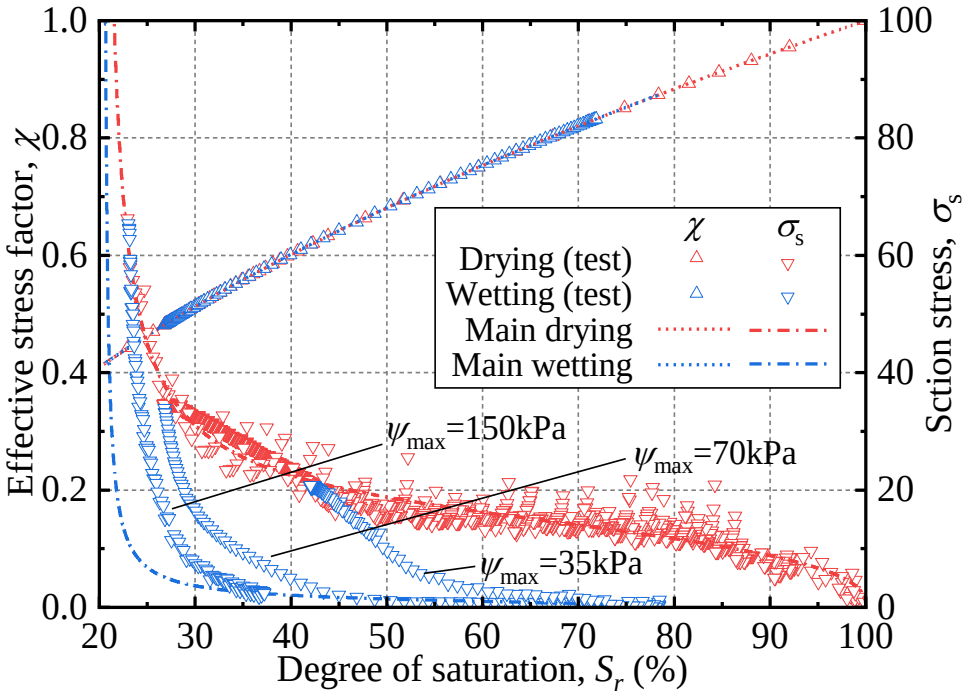


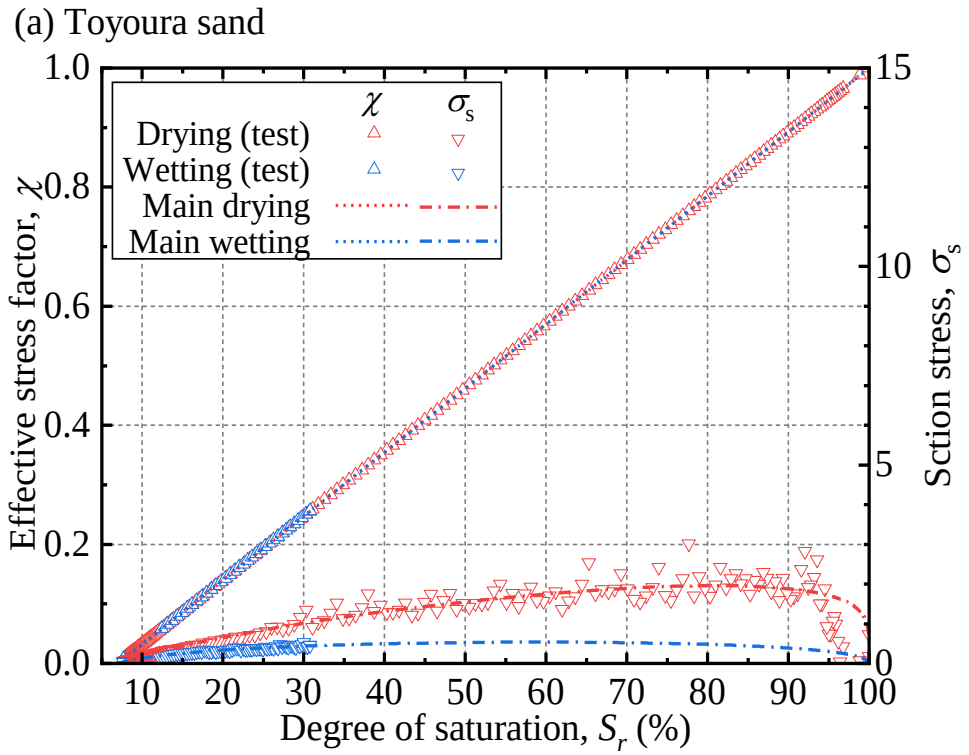
Figure 5-1 Variation of χ and σ_s with the S_r using the Vanapalli model: (a) Toyoura sand; (b) Tomakomai soil

5.2.2 Karube model

Another χ estimation model based on the water content is also widely used (Karube et al., 1996; Vanapalli et al., 1996):

$$\chi = \frac{\theta_w - \theta_r}{\theta_s - \theta_r} = \frac{S_r - S_0}{1 - S_0} \tag{5-3}$$

where θ_w is volumetric water content; θ_s is saturated volumetric water content; θ_r is residual volumetric water content; S_r is degree of saturation; S_0 is residual degree of saturation. This model is also equivalent to the effective degree of saturation which is widely used in many SWCC models. Figure 5-2 shows the variation of χ and σ_s with the S_r using the Karube model. It can be found that the relationship between χ and S_r in this model is linear because χ is literally the effective degree of saturation.



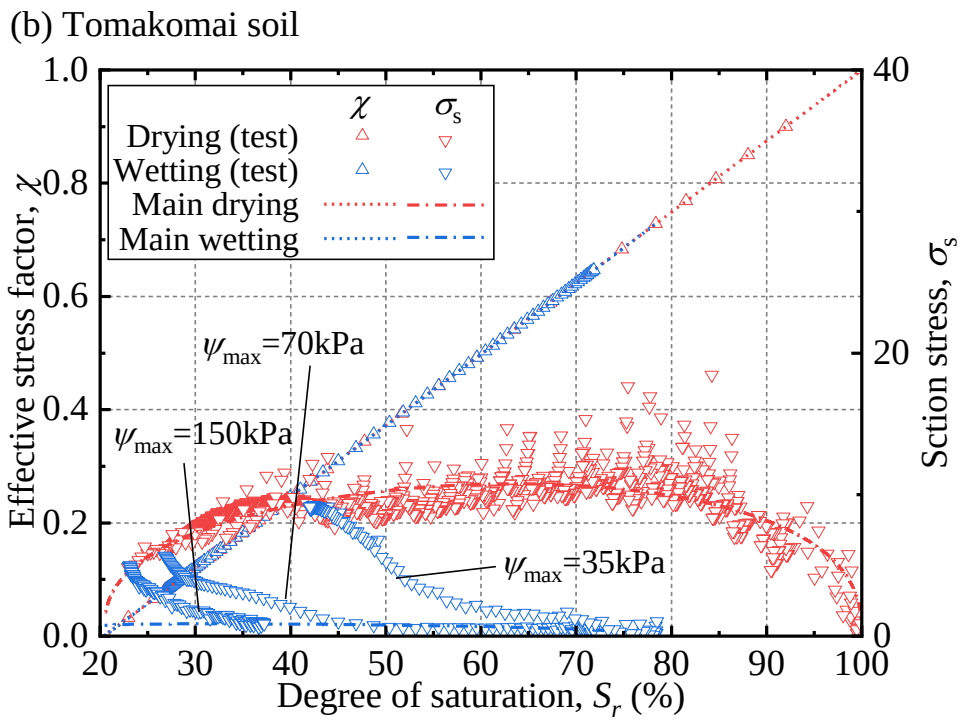


Figure 5-2 Variation of χ and σ_s with the S_r using the Karube model: (a) Toyoura sand; (b) Tomakomai soil

5.2.3 Khalili & Khabbaz (K&K) model

Different from the abovementioned two models based on water content, Khalili and Khabbaz (1998) proposed a χ estimation model based on the suction ratio:

$$\chi = \left[\frac{(u_a - u_w)}{(u_a - u_w)_b}\right]^{\kappa} \tag{5-4}$$

where $(u_a\text{-}u_w)$ is matric suction; $(u_a\text{-}u_w)_b$ is the air entry value of the SWCC; κ is a fitting parameter. It should be noted that similar to the determination of κ in Equation 5-2, the fitting parameter κ in Equation 5-4 also varies by taking different fitting curves, where -0.55 corresponds to the best fit in all samples according to the fitting result obtained by Khalili and Khabbaz (1998). In the cases of Tomakomai soil and Toyoura sand, -0.4 corresponding to the upper bound is proved to be a better fit in this study. Furthermore, to reflect the effect of suction hysteresis, the air entry value (AEV) of the drying path and the water entry value (WEV) of the wetting path is taken as the $(u_a\text{-}u_w)_b$ in the drying and wetting paths, respectively. Figure 5-3 shows the variation of χ and σ_s with the S_r using the K&K model. It can be found that the χ values along SWCCs with different maximum suction in this model are significantly different compared to the other two models.

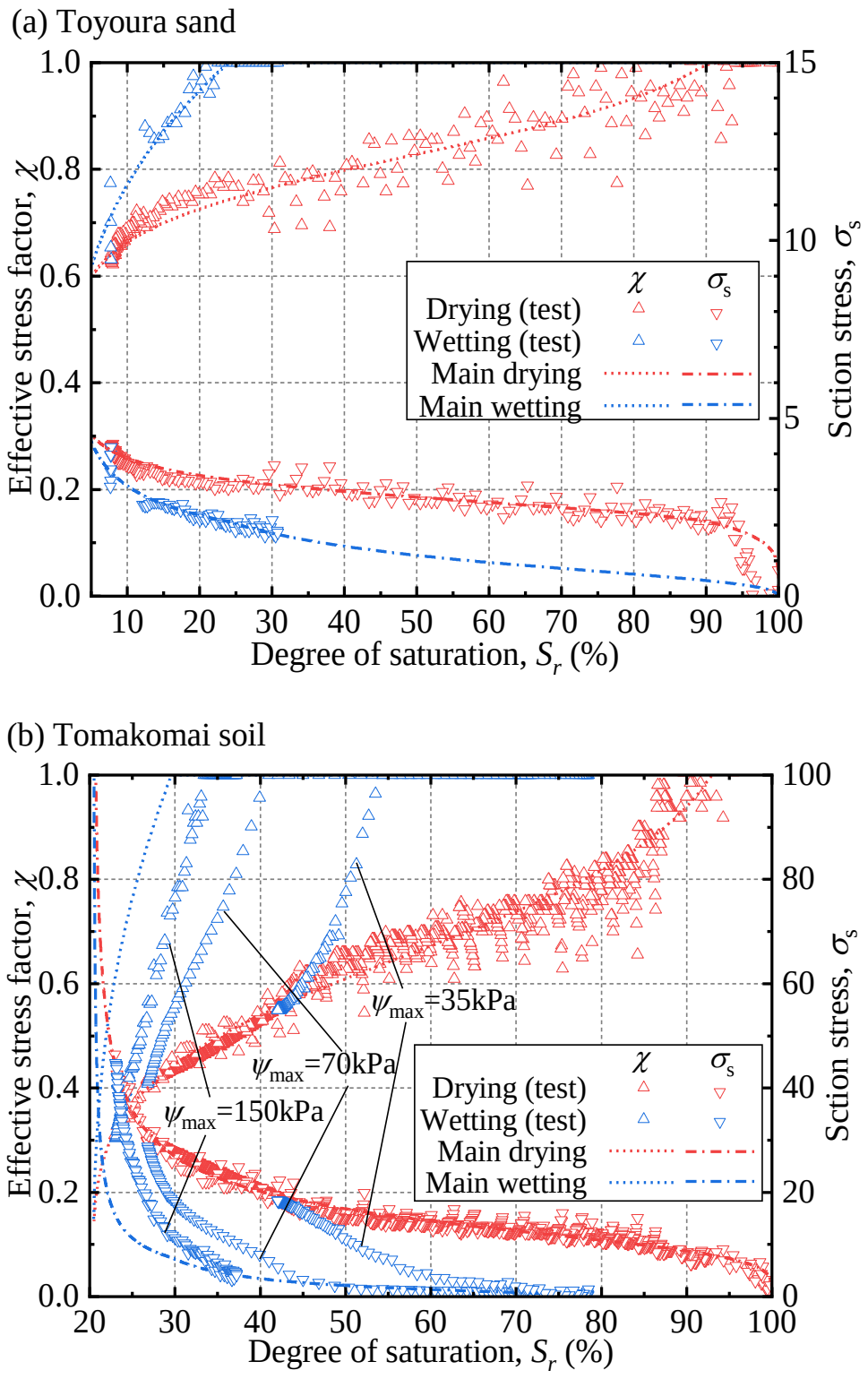


Figure 5-3 Variation of χ and σ_s with the S_r using the Khalili & Khabbaz model: (a) Toyoura sand; (b) Tomakomai soil

5.3 Proposal of Suction Stress Combined M_r Predictive Model

Yang et al. (2005) proposed the following equation based on deviatoric stress σ_d and Bishop's effective stress factor χ:

$$M_r = k_1(\sigma_d + \chi\psi)^{k_2} \quad (5\text{-}5)$$

However, the considered factors of this equation are small. It was confirmed by Han and Vanapalli (2016) that the fitting effect of this equation is relatively low compared to other models.

Liang et al. (2008) proposed Equation 5-6 by combining the MEPDG resilient modulus predictive model with Bishop's effective stress factor χ as shown in the following form:

$$M_r = k_1 p_a \left(\frac{\theta+\chi\psi}{p_a}\right)^{k_2} \left(\frac{\tau_{oct}}{p_a} + 1\right)^{k_3} \quad (5\text{-}6)$$

However, there are some disputes about the factor used in this equation. According to the definition of the bulk stress θ, which is equal to the first invariant of the stress tensor $J_1=(\sigma_1+\sigma_2+\sigma_3)$, every principal stress term should combine with a suction stress term. That is, the factor before the $\chi\psi$ term should be 3.

Therefore, by substituting Bishop's effective stress in Equation 5-1 into the universal model of MEPDG shown in Equation 1-3, the modified MEPDG, which incorporates the concept of effective stress to capture the effect of χ and ψ, can be expressed in the following form as shown in Equation 5-7:

$$M_r = k_1 p_a \left(\frac{\theta+3\chi\psi}{p_a}\right)^{k_2} \left(\frac{\tau_{oct}}{p_a} + 1\right)^{k_3} \quad (5\text{-}7)$$

On the one hand, unlike the factor k_4 in the Ng model is an independent parameter, the factor χ in Equation 6-3 is related to k_2, which may decrease the fitting efficiency. On the other hand, although the Ng model shows good accuracy in fitting the M_r under most moisture conditions, the accuracy may decrease under a significantly low water content because the effect of suction decreases due to the decrement of χ. Furthermore, the Ng model cannot capture the effect of suction hysteresis of SWCC, especially when there is a significant difference in M_r along the drying and wetting paths. Therefore, the Ng model shown in Equation 1-5 can also be modified by substituting the θ term with (θ + 3$\chi\psi$) to overcome the abovementioned shortcomings. It should be noted that because the net normal stress σ_{net} = θ/3 – u_a, and the pore air pressure in this test is

equivalent to 0 kPa based on the axis translation technique and effective stress principle, the modified equation can be expressed as the following form as shown in Equation 5-8.1:

$$M_r = k_1 p_a \left(\frac{\theta+3\chi\psi}{p_a}\right)^{k_2} \left(\frac{\tau_{oct}}{p_a}+1\right)^{k_3} \left(\frac{\psi}{\frac{\theta+3\chi\psi}{3}}+1\right)^{k_4} \quad (5\text{-}8.1)$$

and can be further simplified as Equation 5-8.2:

$$M_r = k_1 p_a \left(\frac{\theta+3\chi\psi}{p_a}\right)^{k_2} \left(\frac{\tau_{oct}}{p_a}+1\right)^{k_3} \left(\frac{1}{\frac{\theta}{3\psi}+\chi}+1\right)^{k_4} \quad (5\text{-}8.2)$$

Different from equations based on the universal model of MEDPG, Heath et al. (2004) proposed a similar predictive model as shown in Equation 5-9, utilizing mean principal stress $\theta/3$ and deviator stress σ_d instead of bulk stress θ and octahedral shear stress τ_{oct}, respectively. To verify the applicability of the predictive models, Equations 5-7, 5-8, and 5-9 are selected to fit the results of U tests and compared in the later section.

$$M_r = k_1 p_a \left(\frac{\theta/3+\chi\psi}{p_a}\right)^{k_2} \left(\frac{\sigma_d}{p_a}\right)^{k_3} \quad (5\text{-}9)$$

5.4 Applicability and Comparison of M_r Predictive Models

To improve the fitting efficiency and verify the validity and reliability, the M_r obtained from the U tests for Toyoura sand and Tomakomai soil are divided into two groups: M_r along the drying path as the fitting group to obtain the regression parameters; M_r along the wetting path as the verification group to check the fitting validity and reliability. Figure 5-4 to Figure 5-6 show the comparison of the tested and predicted M_r by different M_r predictive models combined with different χ estimation models. It can be found that compared with the modified MEPDG model and Heath model shown in Figure 5-4 and Figure 5-5, the plots of the modified Ng model in Figure 5-6 are closer to the 1:1 line, indicating that the modified Ng model shows the highest fitting accuracy. On the one hand, the modified Ng model can capture the effect of matric suction and water content simultaneously and reflect the difference in M_r along drying and wetting paths. On the other hand, the modified Ng model utilizes an independent parameter k_4 to capture the effect of matric suction as a supplement to the overfitting by k_2. By comparing the χ estimation models utilized in the M_r predictive models, it can be found that the plots of the Karube model significantly deviate from the 1:1 line, especially in

Figure 5-4 (b) and Figure 5-5 (b), indicating that the Karube model has the lowest fitting accuracy. As shown in Figure 5-2, since the relationship between χ and S_r is linear by estimating with the Karube model, while the practical relationship was proved to be nonlinear (Bishop and Blight 1963), it is easy to understand that the Karube model has lower accuracy than the other two nonlinear χ models.

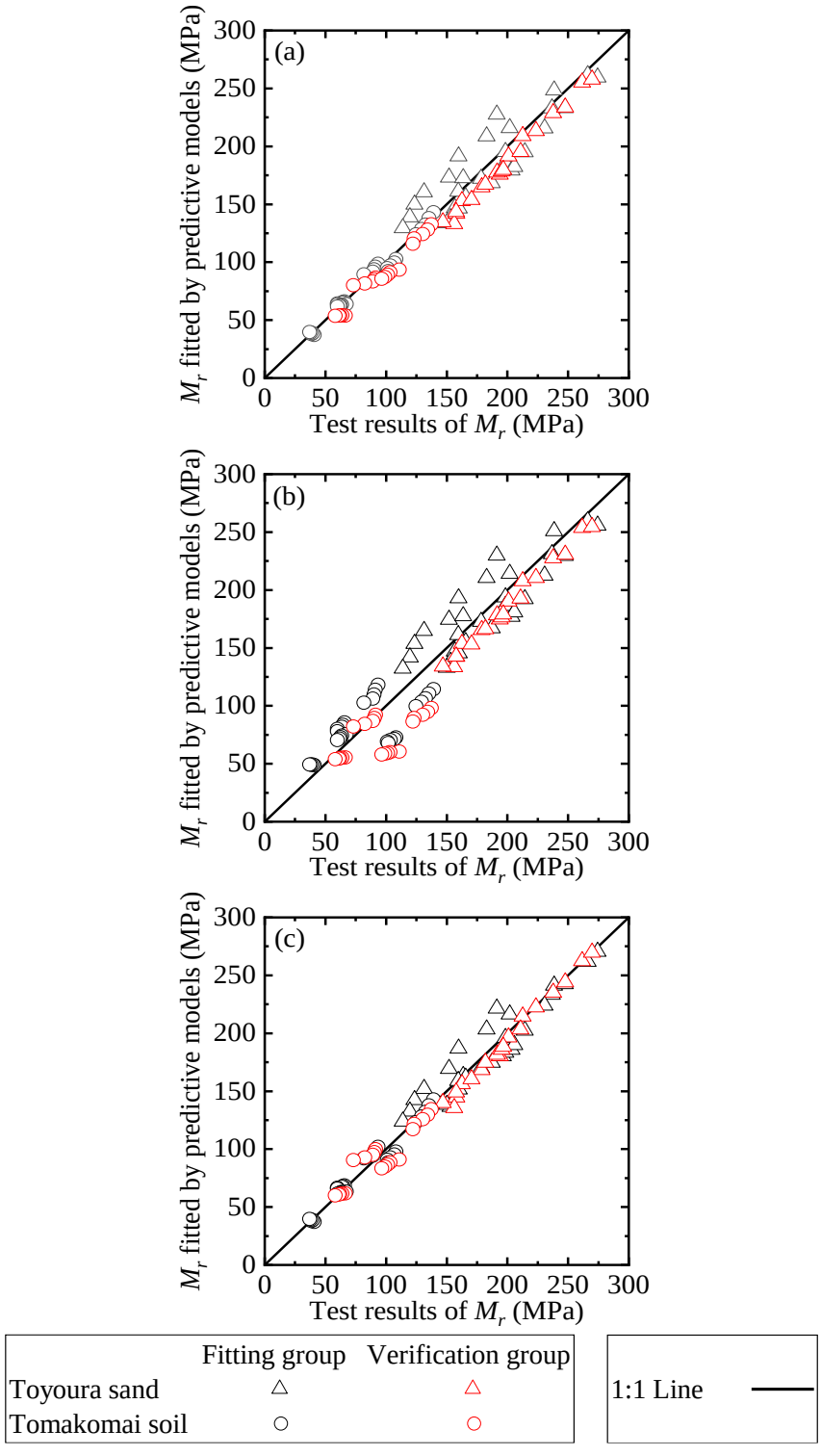


Figure 5-4 Comparison between tested and fitted M_r by different combinations with the modified MEPDG model: (a) Vanapalli model; (b) Karube model; (c) K&K model

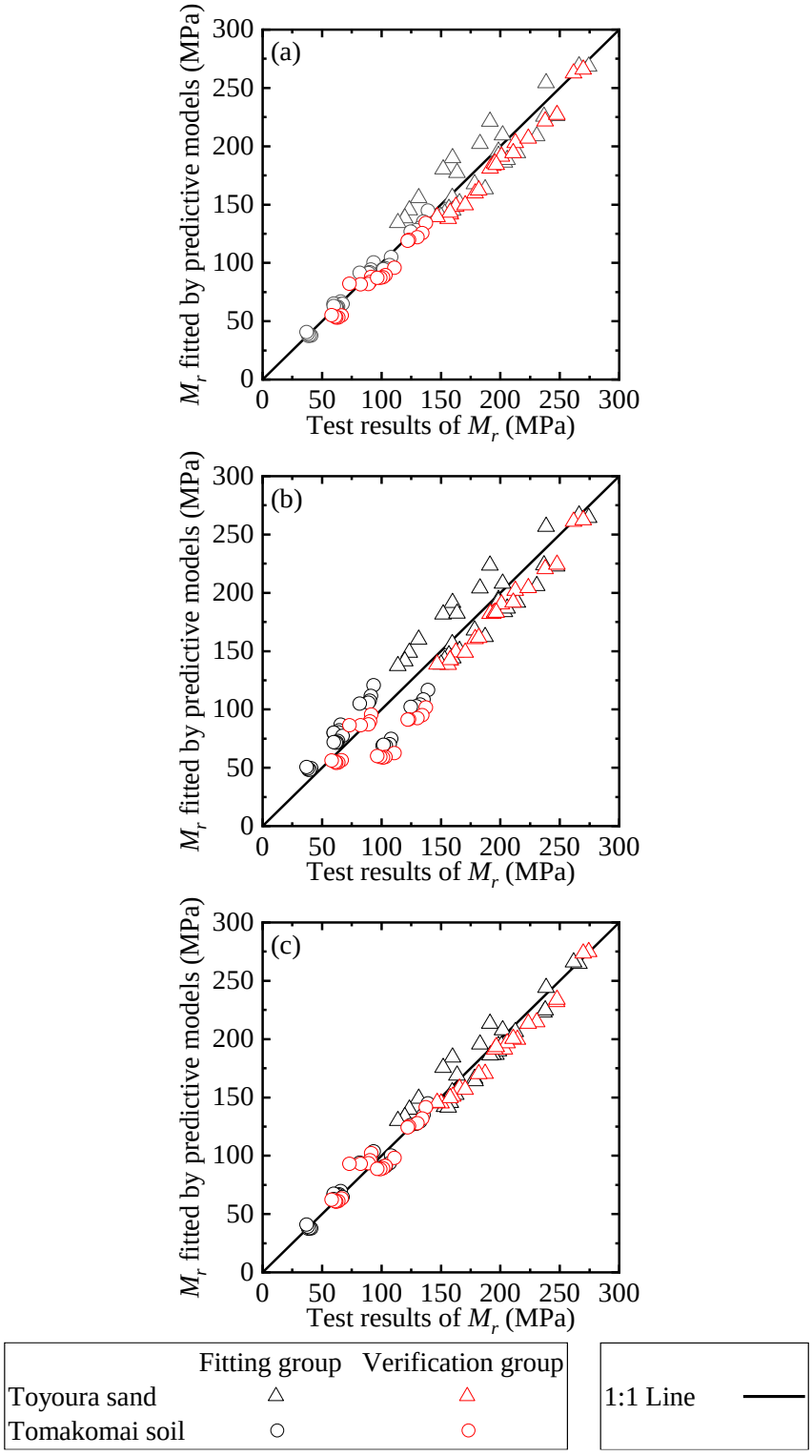


Figure 5-5 Comparison between tested and fitted M_r by different combinations with the Heath model with: (a) Vanapalli model; (b) Karube model; (c) K&K model

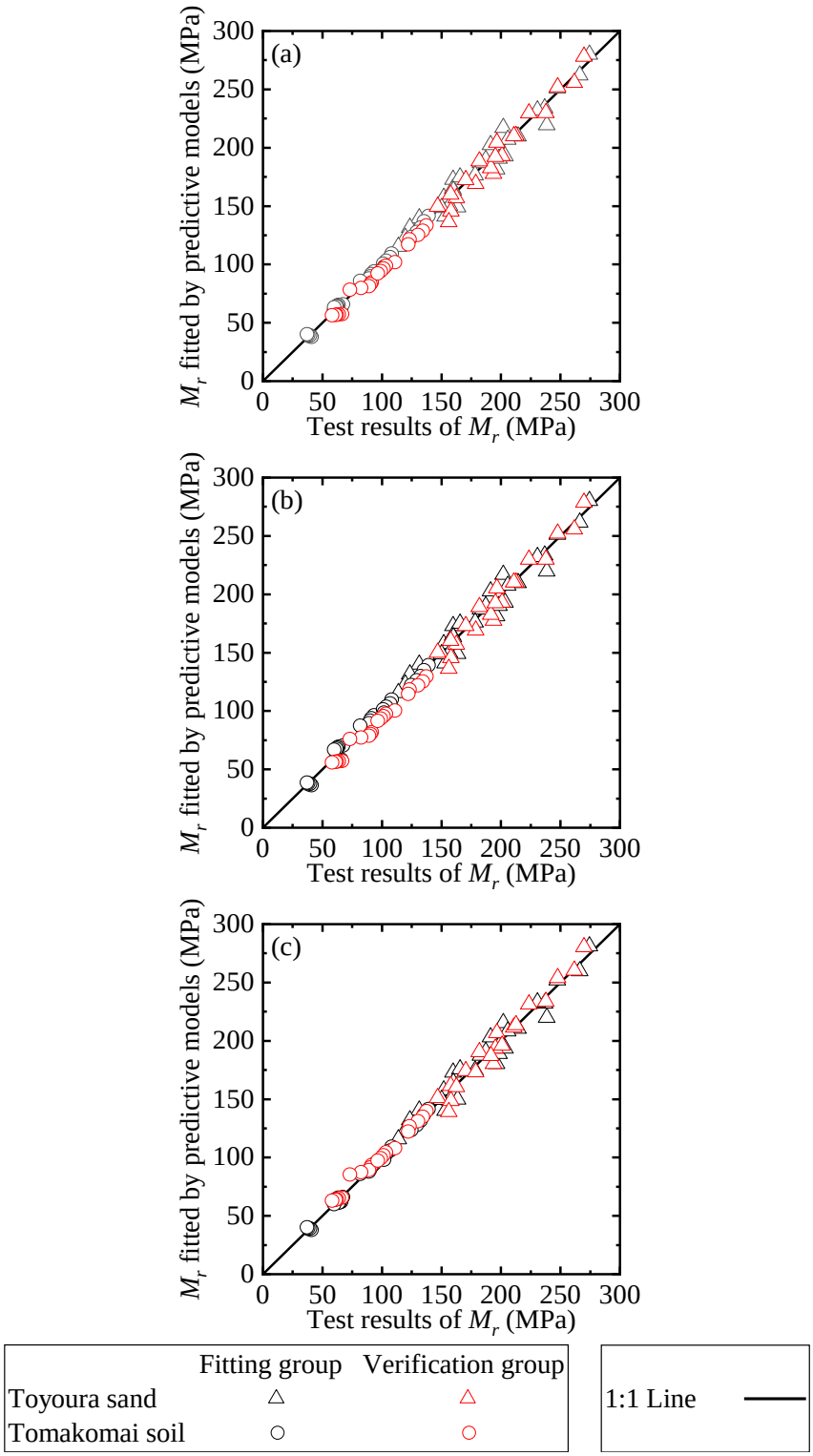


Figure 5-6 Comparison between tested and fitted M_r by different combinations with the modified Ng model: (a) Vanapalli model; (b) Karube model; (c) K&K model

Table 5-1 and Table 5-2 show the fitting parameters, R-square, and Mean-square error (MSE) values of different combinations of models. The R-square reflects the

correlation of the predicted and tested results, while the mean-square error reflects the fitting error. Figure 5-7 and Figure 5-8 show the comparison of the R-square and MSE of different combinations of models, where the bars are values of fitting groups, and the scatters are the verification groups. It can be observed that in the case of Tomakomai soil, the modified Ng model combined with the K&K model shows the highest R-square in both the fitting group and verification group and the MSE values are relatively low. In the case of Toyoura sand, the modified Ng model combined with three χ estimation models all show high R-square values and low MSE values, but the modified Ng model combined with the K&K model shows higher fitting accuracy in the verification group. Additionally, by horizontally comparing the χ estimation models, it can be found that the K&K and Vanapalli models both show high accuracy compared to the Karube model. On the other hand, the modified Ng model shows significantly higher accuracy in all cases than the other two models by vertically comparing the M_r predictive models. It is noted that the traditional Ng model can get high R-squares only if the M_r of drying and wetting paths are close. However, in cases of significantly different drying and wetting paths, the modified Ng model may show better accuracy. Therefore, the modified Ng model combined with the K&K or Vanapalli model has the best fit for the MR tests and has potential value in predicting the M_r of subgrade soil under different moisture conditions.

Table 5-1 Fitting parameters of different models

M_r predictive model	χ estimation model	Material	k_1	k_2	k_3	k_4
Modified MEPDG	Vanapalli	Toyoura sand	2.403	1.024	-4.783	-
		Tomakomai soil	0.474	1.620	-2.943	-
	Karube	Toyoura sand	2.456	0.974	-4.726	-
		Tomakomai soil	0.639	1.582	-3.378	-
	K&K	Toyoura sand	2.287	1.100	-4.842	-
		Tomakomai soil	0.483	1.733	-3.179	-
Heath	Vanapalli	Toyoura sand	2.161	1.024	-0.479	-
		Tomakomai soil	1.329	1.615	-0.288	-
	Karube	Toyoura sand	2.123	0.976	-0.474	-
		Tomakomai soil	1.525	1.575	-0.334	-

	K&K	Toyoura sand	2.147	1.044	-0.470	-
		Tomakomai soil	1.440	1.727	-0.312	-
Modified Ng	Vanapalli	Toyoura sand	2.062	1.090	-4.642	1.630
		Tomakomai soil	0.466	1.396	-2.532	0.305
	Karube	Toyoura sand	2.063	1.091	-4.643	1.802
		Tomakomai soil	0.442	1.337	-2.389	0.968
	K&K	Toyoura sand	2.073	1.081	-4.636	1.164
		Tomakomai soil	0.466	1.390	-2.527	0.442

Table 5-2 Fitting errors of different models

M_r predictive model	χ estimation model	Material	R^2_{fit}	MSE_{fit}	R^2_{veri}	MSE_{veri}
Modified MEPDG	Vanapalli	Toyoura sand	0.794	197.24	0.841	78.20
		Tomakomai soil	0.982	9.73	0.877	30.85
	Karube	Toyoura sand	0.750	239.21	0.819	88.91
		Tomakomai soil	0.470	282.57	-0.331	334.56
	K&K	Toyoura sand	0.879	116.13	0.937	30.89
		Tomakomai soil	0.958	22.64	0.850	37.81
Heath	Vanapalli	Toyoura sand	0.812	180.10	0.830	83.60
		Tomakomai soil	0.979	11.21	0.872	32.15
	Karube	Toyoura sand	0.769	221.39	0.809	93.87
		Tomakomai soil	0.470	282.87	-0.254	315.11
	K&K	Toyoura sand	0.888	94.99	0.919	45.11
		Tomakomai soil	0.955	24.17	0.890	27.70
Modified Ng	Vanapalli	Toyoura sand	0.955	41.74	0.942	28.54
		Tomakomai soil	0.995	2.51	0.949	12.86
	Karube	Toyoura sand	0.954	42.44	0.940	29.61
		Tomakomai soil	0.983	8.59	0.915	21.34
	K&K	Toyoura sand	0.951	44.96	0.955	21.97
		Tomakomai soil	0.995	2.64	0.980	5.00

Note: R^2_{fit}, MSE_{fit}: R-square and mean square error of fitting group; R^2_{veri}, MSE_{veri}: R-square and mean square error of verification group.

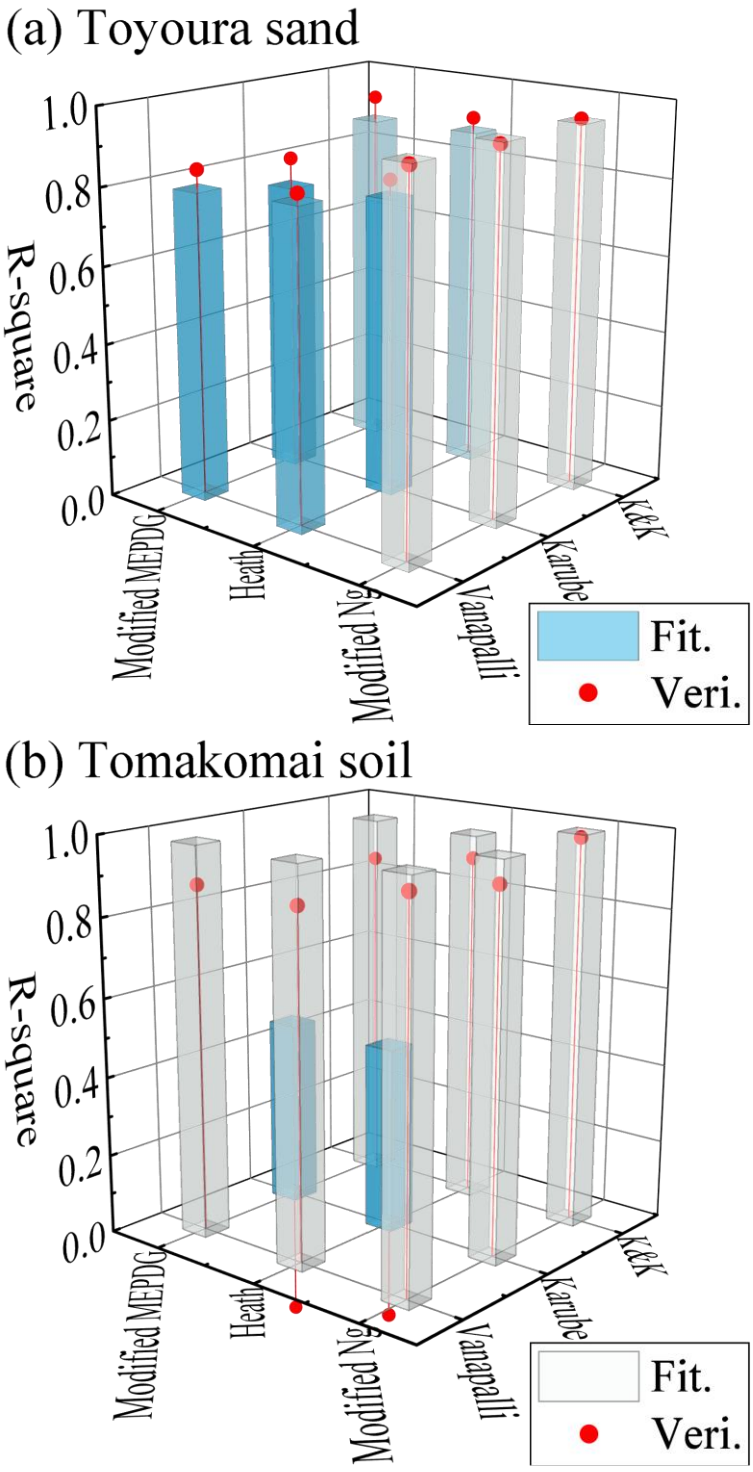


Figure 5-7 R-square values by different combinations of models: (a) Toyoura sand; (b) Tomakomai soil

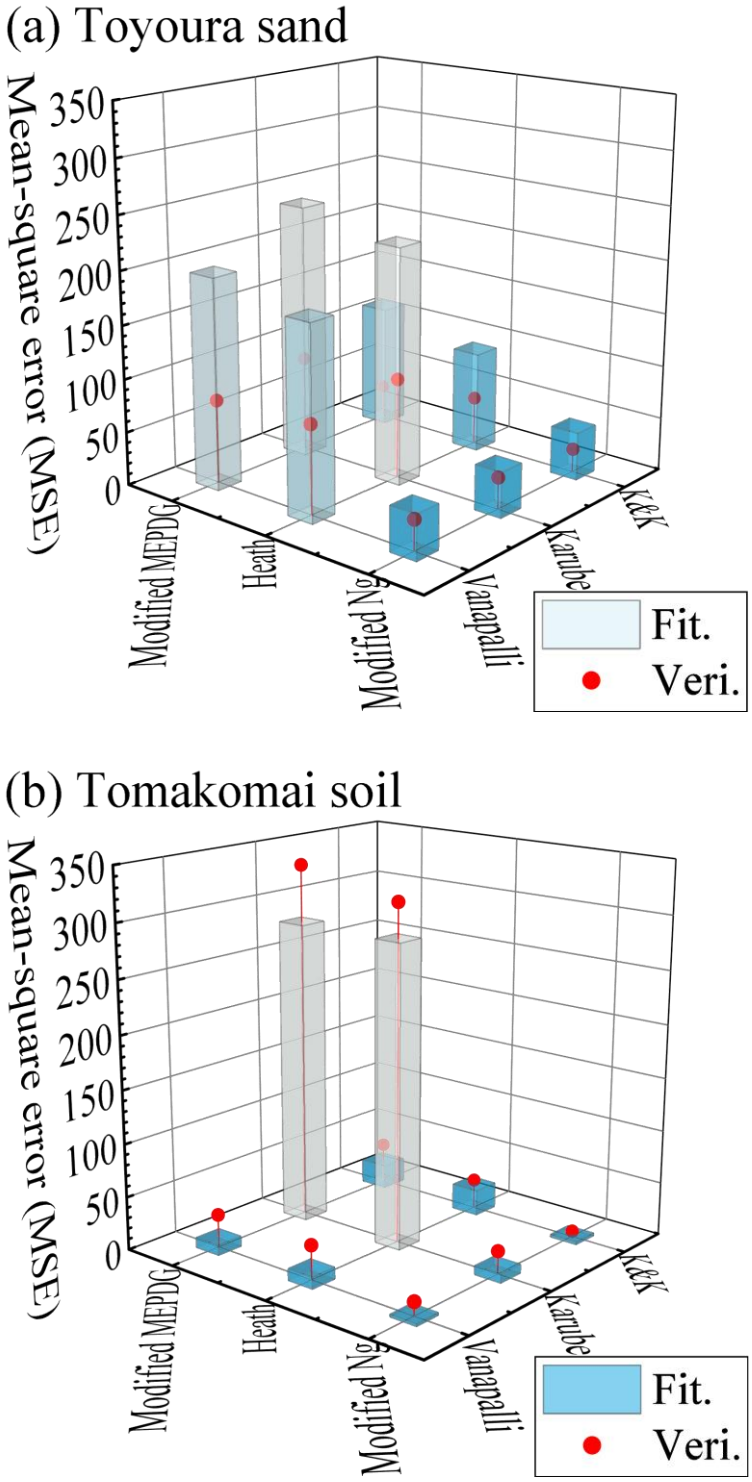


Figure 5-8 MSE values by different combinations of models: (a) Toyoura sand; (b) Tomakomai soil

5.5 Summary

The M_r of unsaturated soils is not only affected by matric suction but also affected by moisture content, which is presented as Bishop's effective stress factor χ. By incorporating the factor χ into the M_r predictive models and further determining χ with different estimation models, some combinations of predictive models can be obtained and compared to investigate their applicability in predicting unsaturated M_r under various moisture conditions, especially under the effect of suction hysteresis of SWCC.

1. Three different χ estimation models respectively based on normalized volumetric water content, effective degree of saturation, and suction ratio are employed to determine the χ values. All the estimated results indicate that the χ and σ_s are significantly affected by the degree of saturation. Furthermore, since the degree of saturation differs along different drying and wetting paths even if the suction is the same, the M_r also differs along different drying and wetting paths.

2. The existing M_r predictive models considering Bishop's effective stress rarely discuss their applicability to the wetting path of SWCC, and there are also some disputes about the factors in the equations or the determination method of χ. Some modified models are obtained by incorporating χ into the MEPDG-based M_r predictive models in this study. By using some χ estimation models, the χ values are determined by the degree of saturation or suction ratio and further combined with the predictive models to compare the applicability and fitting efficiency of different χ estimation models and M_r predictive models.

3. The M_r obtained from the U tests for both Toyoura sand and Tomakomai soil are divided into the fitting group and verification group to improve the fitting efficiency and verify the validity and reliability. The M_r results along the drying path are used as the fitting group to obtain the fitting parameters, and the M_r results along the wetting path are used as the verification group to verify the validity and reliability of the fitting. For the χ estimation models, the Vanapalli model and K&K model both show high fitting accuracy compared to the Karube model because the relationship between χ and S_r was proved to be nonlinear. On the other hand, the modified Ng model shows significantly higher accuracy in all cases than the other two models by vertically comparing the M_r predictive models. Therefore, the modified Ng model combined with the K&K or Vanapalli model has the best fit

for the MR tests and has potential value in predicting the M_r of subgrade soil under different moisture conditions.

6 EFFECTS OF PRINCIPAL STRESS AXIS ROTATION ON PERMANENT STRAIN

6.1 Materials and Method

This chapter utilizes the test results obtained by Inam et al. (2012) to examine the behavior of resilient and permanent axial strains under the effect of PSAR. Two types of unbound aggregate materials including natural crusher-run gravel and recycled concrete crusher-run gravel with maximum grain sizes of 40 mm, abbreviated as C-40 and RC-40, were used in this study. However, according to the AASHTO standard of T-307 (AASHTO 2017), the minimum diameter of the selected mold size to fabricate specimens should be equal to five times the maximum particle size. Therefore, the particles exceeding 9.5 mm were removed in this study due to the limitation of the test apparatus. The C-40 and RC-40 after removing the larger particles were named as C-9.5 and RC-9.5, respectively. Additionally, as the fine fraction may enter the gaps between the shear rings of the test apparatus, the materials were washed inside a 0.075 mm sieve to remove the fine fraction and oven-dried for at least 24 hours. To compare the two materials under the same condition, the grain sizes were controlled to be parallel. Detailed properties of the materials including the physical properties, grain size distribution curves, and soil-water characteristic curves are shown by Inam et al. (2012). Similar tests of subgrade materials such as Toyoura sand and various types of soil mixtures using the multi-ring shear apparatus were also conducted in the past (Dareeju et al. 2017; Ishikawa et al. 2021; Seto et al. 2017). According to the test results of subgrade materials, it was proved that the permanent axial strain is significantly affected by PSAR, and the effect of PSAR can be estimated by the $(R_s)_{ave}$. Therefore, for subgrade materials, the MEPDG rutting model with consideration of PSAR is reasonable.

As shown in Figure 6-1, a multi-ring shear apparatus for laboratory element tests that can apply cyclic axial and shear stress to simulate the effect of PSAR developed by Ishikawa et al. (2007) was utilized in this study. The specimen is 60 mm in width and 60 mm in height, with an external diameter of 240 mm and an internal diameter of 120 mm. Inam et al. (2012) conducted a series of cyclic axial loading and cyclic axial-shear loading tests under different degrees of saturation based on the field data obtained

from the Tomakomai field measurement site near Sapporo, Japan. According to the Japanese standard (Japan Road Association 2019), the degree of compaction was determined as 95%, corresponding to dry densities of 1.58 g/cm^3 and 1.47 g/cm^3 for C-9.5 and RC-9.5. The stress conditions were determined based on the stress analysis by the General Analysis Multi Layered Elastic Systems (GAMES) (Maina and Matsui 2004) under a standard 49 kN traffic load in the Japanese highway standard (Japan Road Association 2019). The pavement structure and the traffic load conditions are shown in Figure 6-2.

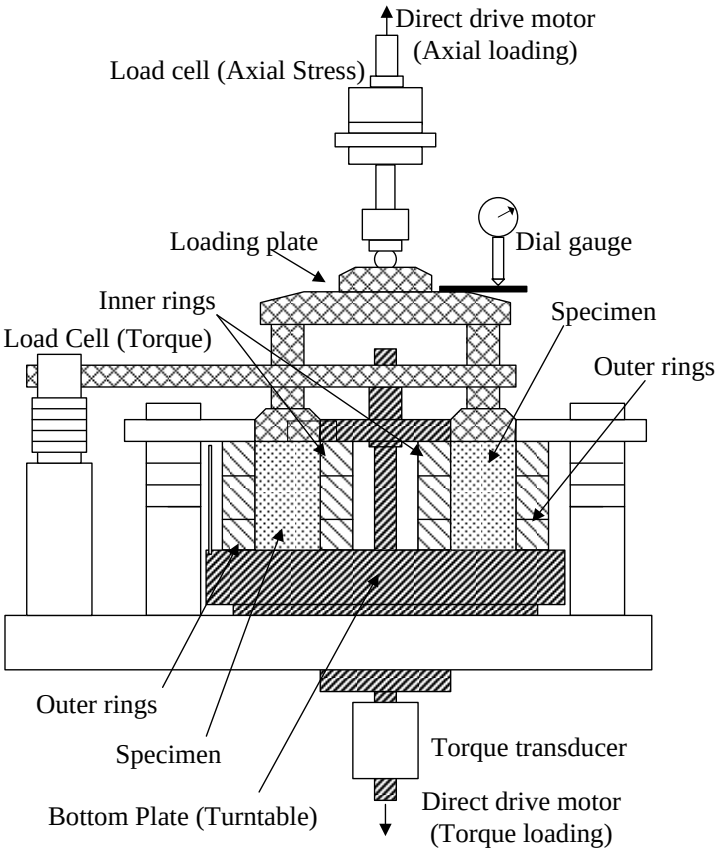


Figure 6-1 Schematic diagram of the multi-ring shear apparatus (Ishikawa et al. 2011)

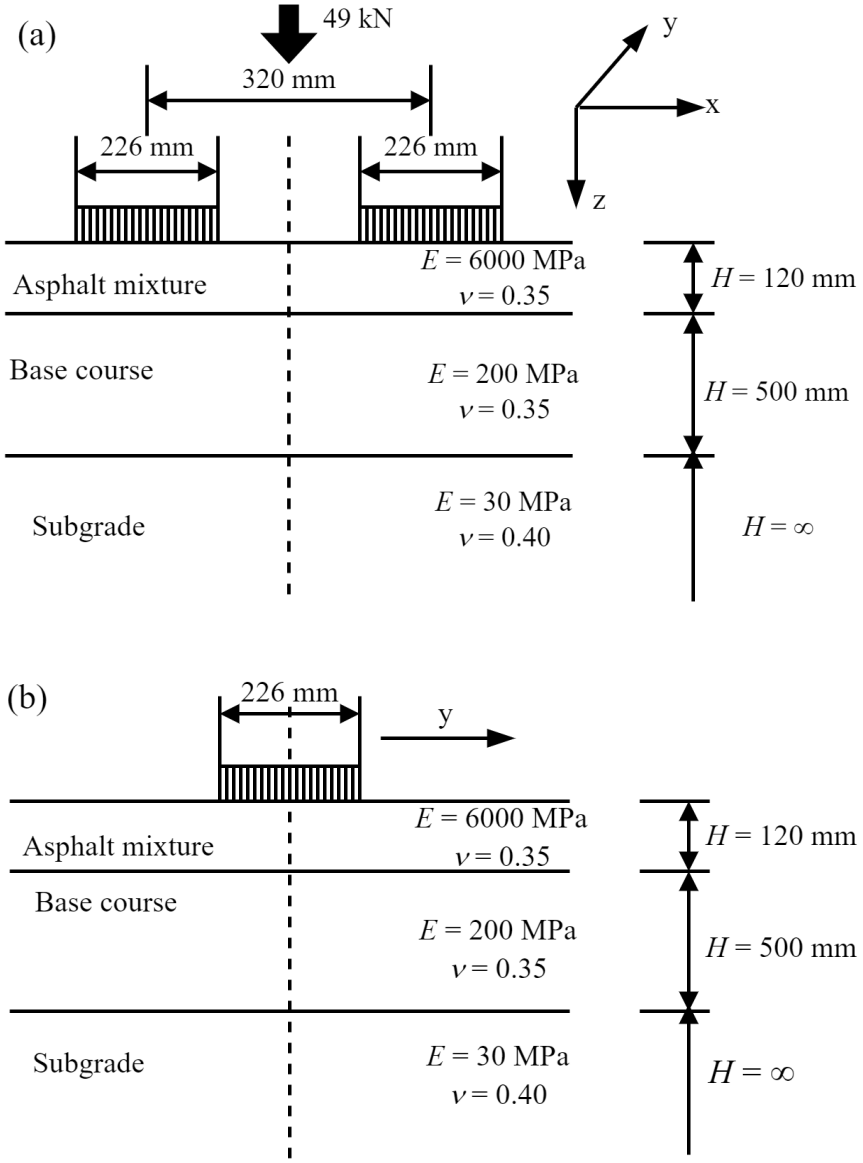


Figure 6-2 Pavement structure and traffic load conditions of multi-ring shear tests: (a) cross section; (b) longitudinal section

After analyzing the stress conditions by GAMES, a maximum axial stress of 114.2 kPa and a maximum shear stress of 30 kPa on the base course surface were obtained. In this study, the existence of PSAR depends on the application of cyclic shear stress. As a result, there are two types of tests based on whether the shear stress exists or not. The test with only cyclic axial loading is defined as the Fixed-Place Loading Test (FL test), while the test with cyclic axial and shear loading is defined as the Moving-Wheel Loading Test (ML test). The detailed test conditions for C-9.5 and RC-9.5 are shown in Table 6-1. The maximum shear stresses in the ML tests for C-9.5 and RC-9.5 both include 30 kPa, but a maximum shear stress of 15 kPa is also adopted in the ML test

for C-9.5 in order to further investigate and validate the behavior of the PSAR under different maximum shear stresses. To simulate the stress change under the moving wheel load in the field, the multi-ring shear apparatus adopts sinusoidal loading waveforms when applying cyclic axial and shear stresses. Additionally, as shown in Figure 6-3, the cyclic axial loading waveform is semi-sinusoidal because the axial stress only has one direction, while the cyclic shear loading waveform is full-sinusoidal because the shear stress changes the direction when the moving wheel load passes the force-bearing point in the center.

Table 6-1 Test conditions for multi-ring shear tests (FL/ML)

Test material	Degree of saturation, S_r (%)	Dry density, ρ_d (g/cm^3)	Maximum axial stress, $(\sigma_a)_{max}$ (kPa)	Maximum shear stress, $(\tau_{a\theta})_{max}$ (kPa)
C-9.5	Oven-dried	1.58	114.2	30/15
	19	1.58	114.2	30/15
	33	1.58	114.2	30/15
	48	1.58	114.2	30/15
RC-9.5	Oven-dried	1.47	114.2	30
	19	1.47	114.2	30
	33	1.47	114.2	30
	48	1.47	114.2	30

Note: there is no shear stress applied in the FL tests.

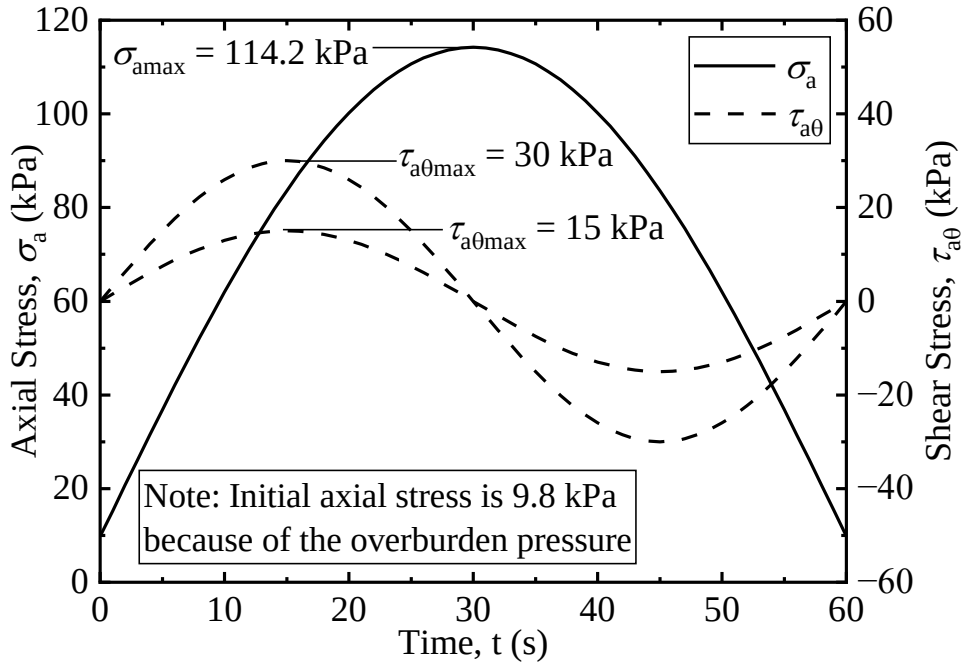


Figure 6-3 Loading waveforms of each cycle in multi-ring shear tests

6.2 Test Results and Discussions

6.2.1 Resilient strain under PSAR

Figure 6-4 shows the resilient axial strain under different degrees of saturation for C-9.5 and RC-9.5, respectively. It can be found that the resilient axial strain is nearly constant during the loading process, although it varies in the initial stage with the increment of the number of loading cycles, especially as can be observed in Figure 6-4 (b). The possible reason for that is the restructuring of the soil skeleton. However, in all cases, the resilient axial strain tends to be stable after 100 loading cycles. For both C-9.5 and RC-9.5 with various degrees of saturation, the oven-dried specimens have the largest resilient axial strain, and the specimens with a 19% degree of saturation have the smallest resilient axial strain. The reason for this phenomenon is that the specimen with a relatively lower degree of saturation (undried) has greater matric suction, which leads to greater strength and smaller strain.

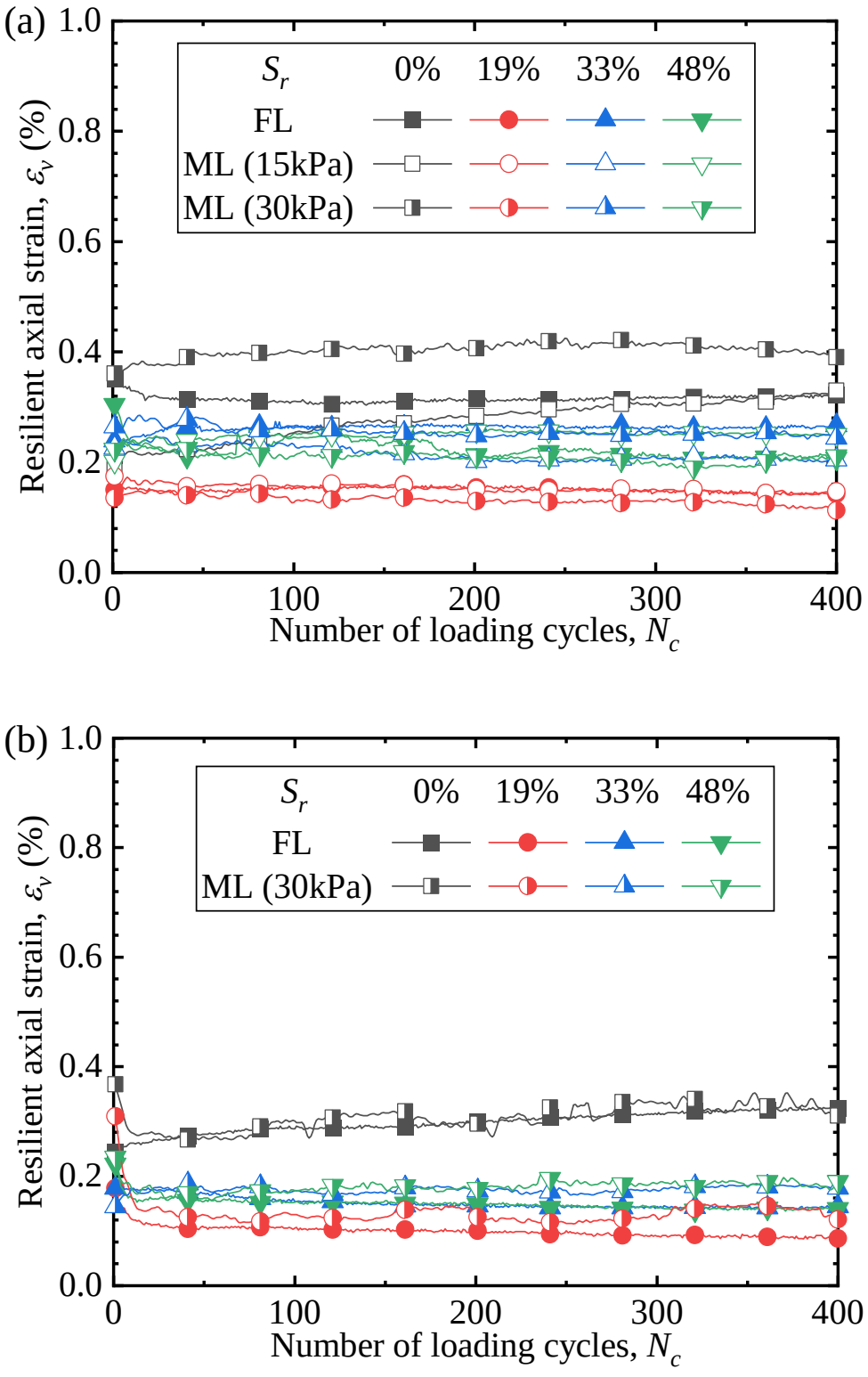


Figure 6-4 Resilient strain under different degrees of saturation: (a) C-9.5, (b) RC-9.5

Since the resilient strain becomes stable in the later stage of the test, the average value of the last 100 loading cycles is regarded as the resilient axial strain. By comparing the resilient axial strain in the FL test and ML test, Figure 6-5 is obtained.

Here, the vertical lines between the plots and the 1:1 line reflect the error between the ratio of ML/FL and 1:1. It can be found that the ratio of resilient axial strain in the FL test to the ML test is close to the 1:1 line and slightly greater than 1, which indicates that the PSAR may slightly increase the resilient axial strain. Furthermore, the results in Figure 6-5 include test conditions under different water contents, which indicates that the test results show this trend despite the water content.

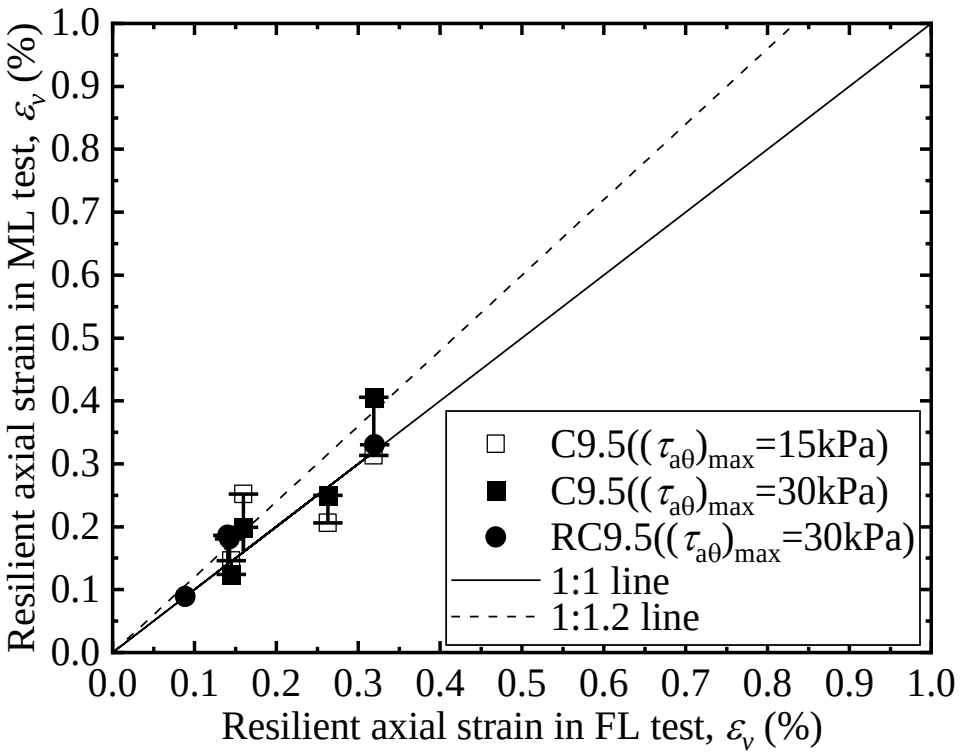


Figure 6-5 Relationship between resilient axial strains in FL and ML tests

Figure 6-6 shows the change of resilient axial strain with S_r for C-9.5 and RC-9.5, respectively. It can be found that the resilient axial strain under the oven-dried condition is significantly different from other unsaturated conditions. This is because the strength of unsaturated soil is mainly affected by the matric suction, but the matric suction does not exist when S_r = 0%. Therefore, the soil strength under the oven-dried condition is significantly lower than under other unsaturated conditions, which leads to a higher resilient axial strain. Except for the oven-dried condition, the resilient axial strain under other unsaturated conditions increases with the increment of S_r. This is because the matric suction decreases with the increment of S_r, which leads to lower soil strength and higher resilient axial strain. For C-9.5, the resilient axial strain of the FL test, ML test (15 kPa), and ML (30 kPa) are nearly equal, which indicates that the effect of shear strength level on the resilient axial strain of C-9.5 is small. On the other hand, for RC-

9.5, the resilient axial strain of the ML test (30 kPa) is slightly greater than that of the FL test, which indicates that the cyclic shear stress may increase the resilient axial strain of RC-9.5.

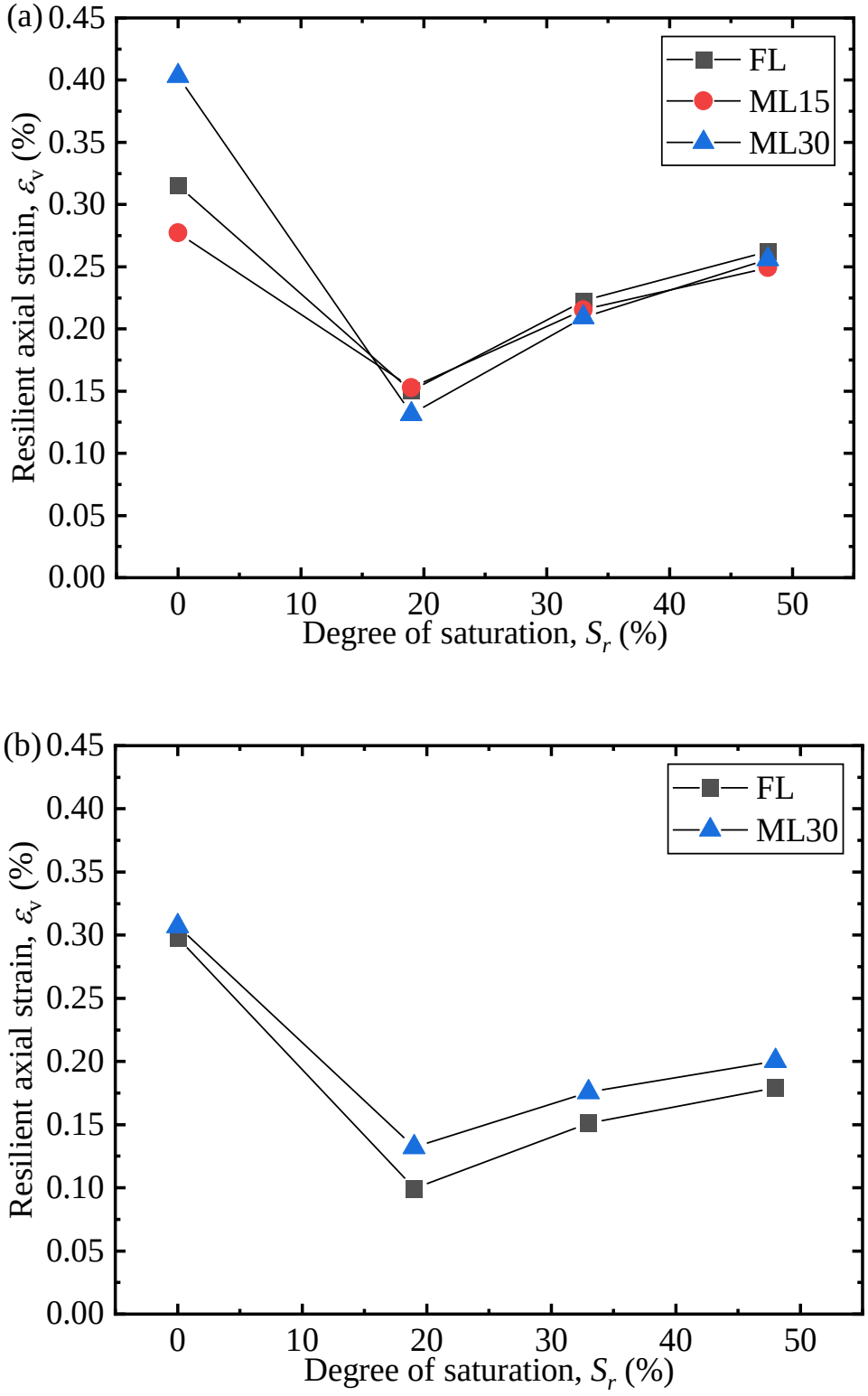
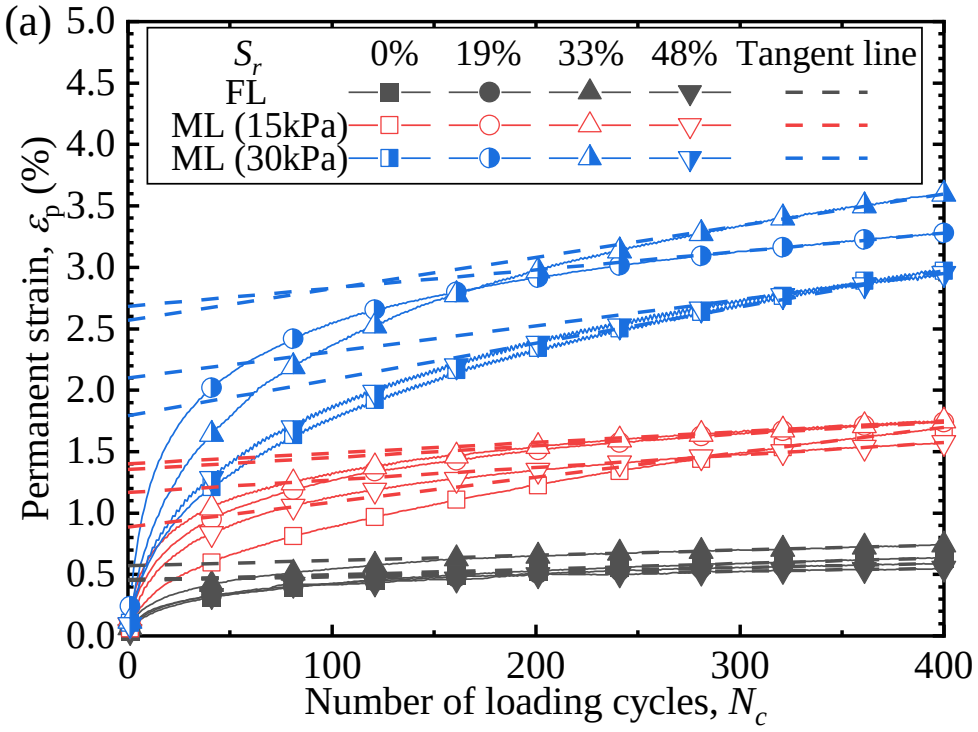


Figure 6-6 Effect of degree of saturation on resilient axial strain: (a) C-9.5, (b) RC-9.5

6.2.2 Permanent strain under PSAR

Figure 6-7 shows the permanent axial strain under different degrees of saturation for C-9.5 and RC-9.5, respectively. It can be found that the permanent axial strain in the ML test is greater than that in the FL test. Meanwhile, the permanent axial strain increases with the increment of maximum applied shear stress $(\tau_{a\theta})_{max}$, which indicates that the PSAR greatly affects the permanent axial strain.



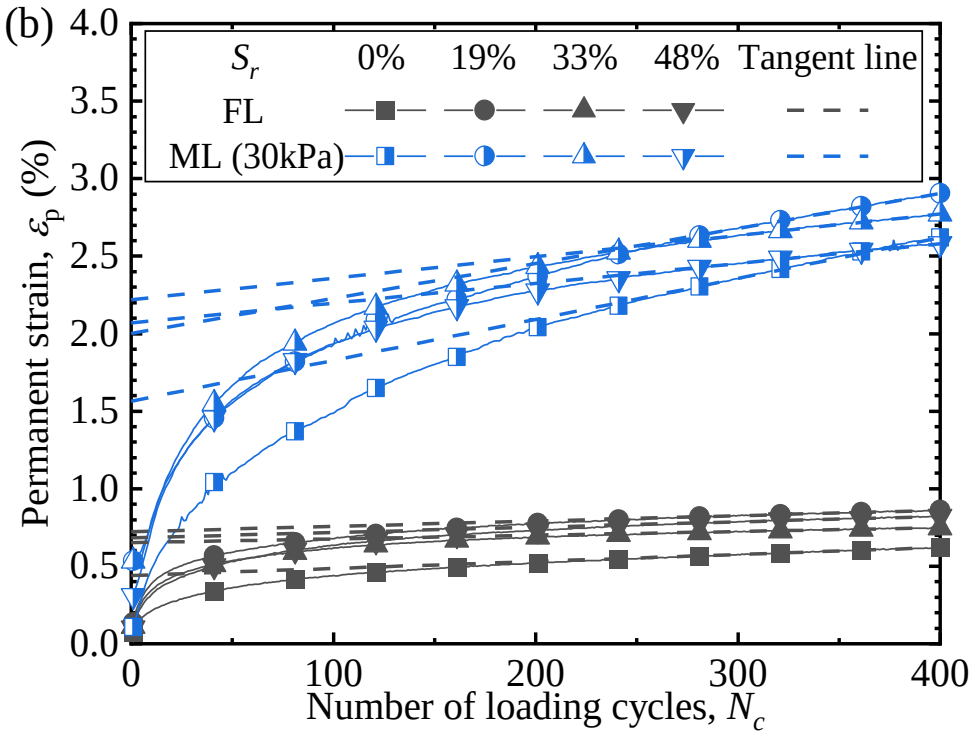


Figure 6-7 Permanent strain under different degrees of saturation: (a) C-9.5, (b) RC-9.5

Moreover, although the permanent axial strain increases with the increment of the number of loading cycles, the increasing rate converges to a constant in the later stage of the test. By taking the tangent line of the permanent strain curve in the last 100 loading cycles, the increasing rate δ of each curve can be obtained, which is defined as the slope of the tangent line. Figure 6-8 shows the comparison of the increasing rate of the permanent axial strain in the FL test and ML test. By conducting the regression analysis on test results under different conditions, the regression lines can be obtained. From Figure 6-8, it can be found that obviously, the increasing rate of the permanent axial strain in the ML test is greater than that in the FL test. Moreover, the increasing rate of the permanent axial strain also increases with the increment of the maximum applied shear stress.

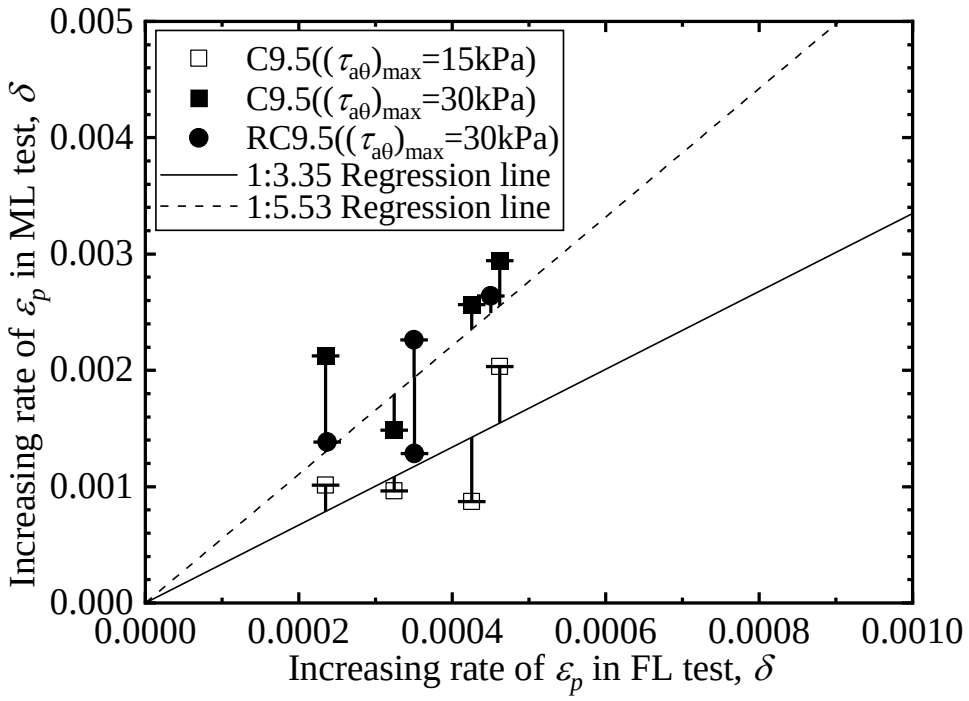


Figure 6-8 Relationship between the increasing rate of permanent axial strain in FL and ML tests

Figure 6-9 shows the change of increasing rate of ε_p with S_r for C-9.5 and RC-9.5, respectively. It can be found that for both C-9.5 and RC-9.5, the increasing rate of ε_p decreases with the increment of S_r and increases with the increment of shear stress level. It indicates that the cyclic shear stress increases the permanent strain, that is, the PSAR has a significant effect on the permanent strain.

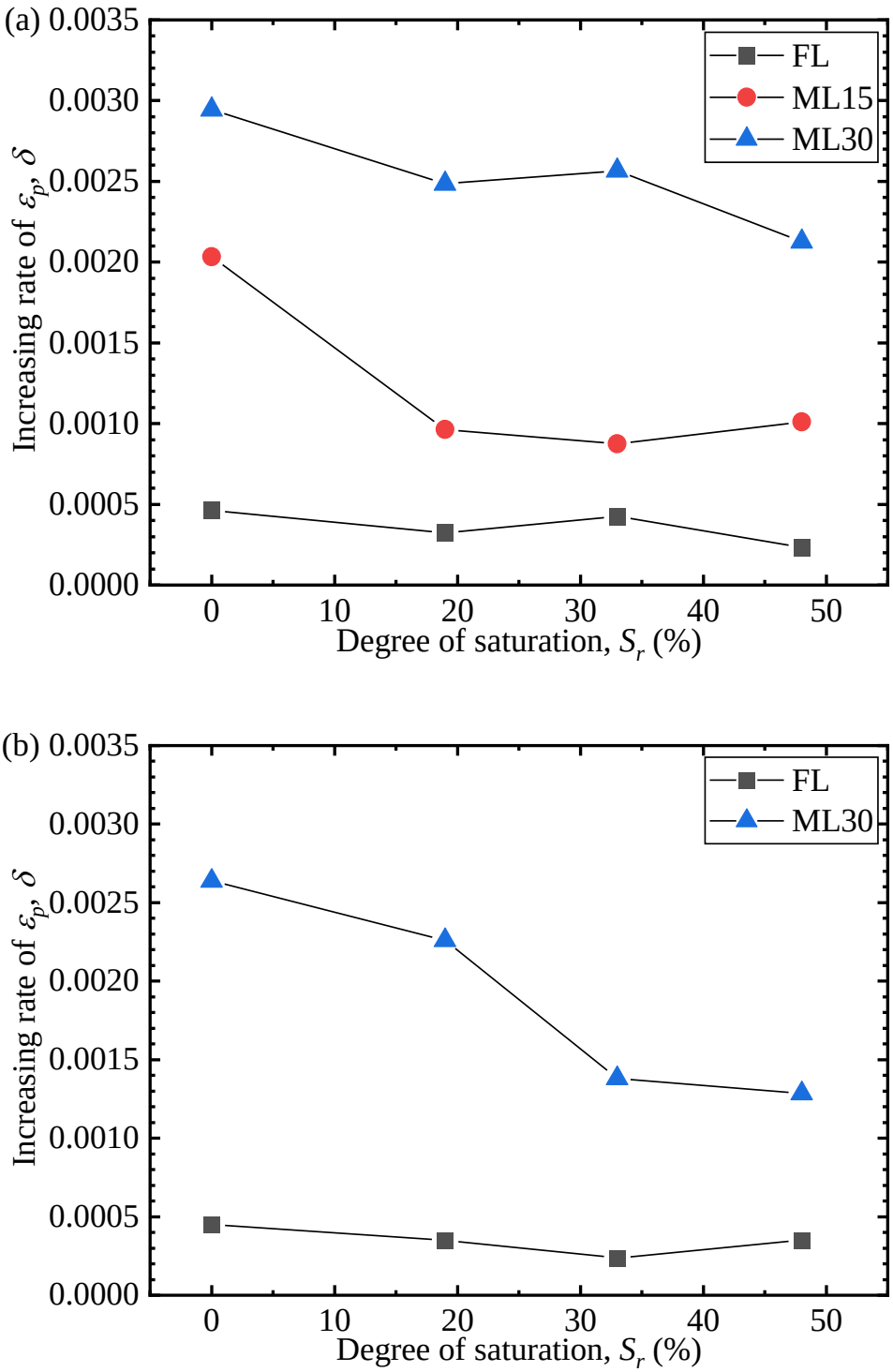
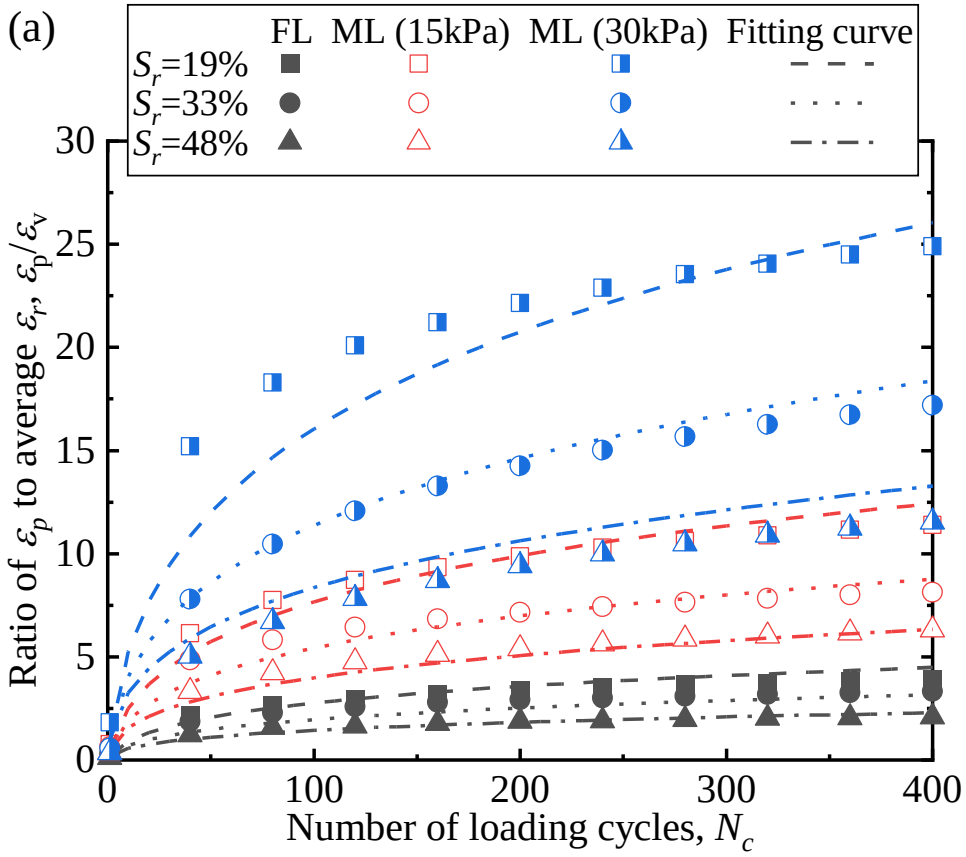


Figure 6-9 Effect of degree of saturation on the increasing rate of ε_p: (a) C-9.5, (b) RC-9.5

6.2.3 Relation between resilient and permanent strains

Figure 6-10 shows the ratio of permanent strain to resilient strain for C-9.5 and RC-9.5, respectively. It is noted that the test results under the oven-dried condition are not considered in the following parts because of two reasons. On the one hand, the

results under the oven-dried condition are significantly different from other unsaturated conditions because matric suction does not exist when S_r = 0%. On the other hand, the water content of in-site subgrade soil is generally greater than 0. From Figure 6-10, it can be inferred that there is a certain relation between permanent strain and resilient strain. The ratio of $\varepsilon_p/\varepsilon_v$ increases with the increment of the shear stress level and decreases with the increment of the S_r.



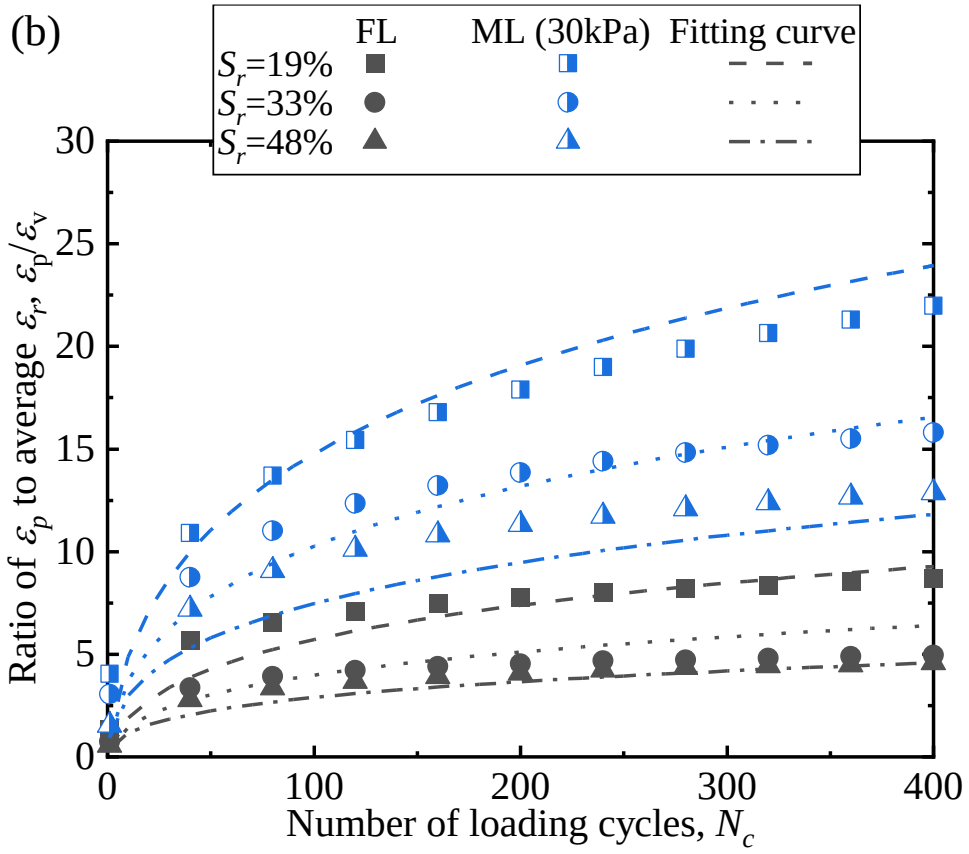


Figure 6-10 Ratio of permanent strain to resilient strain and fitting curves by Equation 6-1: (a) C-9.5, (b) RC-9.5

To analyze the dependency of the ratio of permanent strain to resilient strain on shear stress level and S_r, Eq. 1 is transformed into Equation 6-1:

$$\frac{\varepsilon_p}{\varepsilon_v} = \beta_1 k_{s1} \left(\frac{\varepsilon_0}{\varepsilon_r}\right) exp\left(-\left(\frac{\rho}{N_c}\right)^{\beta}\right) \quad (6\text{-}1)$$

The ratio of permanent strain to average resilient strain, $\varepsilon_p/\varepsilon_v$, in Equation 6-1 is a function of the material properties and the number of loading cycles. ε_v can be calculated from Figure 6-4 by taking the average as shown in Table 6-2. The parameters β, ρ and ($\varepsilon_0/\varepsilon_r$) can be calculated from W_c by Equation 1-7 as shown in Table 6-3, and substituted into Equation 6-1. k_{s1} as the global calibration coefficient is 1.673 for granular materials. β_1 as the local calibration coefficient can be calculated by regression analysis. MEPDG considers the effect of water content by the parameters related to water content such as β, ρ, and ($\varepsilon_0/\varepsilon_r$), which are calibrated based on field data. This study conducts the regression analysis of the test results for the same test sample under the same loading conditions with various water content. Therefore, the regression analysis of test samples under different water contents can be conducted together to

obtain the best fit of the local calibration coefficient β_1. Figure 6-10 and Table 6-4 show the fitting curves and regression results, respectively. It can be found that the local calibration coefficient β_1 increases with the increment of maximum applied shear stress, which indicates that the PSAR strongly affects the value of the local calibration coefficient. However, although the MEPDG model can reflect the trend of the test data to some extent, the R-square values are relatively small as shown in Table 6-4. This is because the prediction of permanent strain of unsaturated specimens under PSAR conditions is affected by the synergistic effects of water content and shear stress level (Inam et al. 2012; Lin et al. 2019). To get more precise fitting results, the effect of shear stress level should also be considered and fitted together with the effect of water content.

Table 6-2 Average resilient axial strain under different test conditions

	Material	S_r (%)	ε_v (%)
FL	C-9.5	19	0.150
		33	0.223
		48	0.262
	RC-9.5	19	0.099
		33	0.151
		48	0.179
ML ($(\tau_{a\theta})_{max}$=15kPa)	C-9.5	19	0.153
		33	0.215
		48	0.249
ML($(\tau_{\theta})_{max}$=30kPa)	C-9.5	19	0.132
		33	0.209
		48	0.256
	RC-9.5	19	0.132
		33	0.175
		48	0.201

Table 6-3 Parameters related to water content in Equation 6-1

S_r (%)	Material	W_c (%)	β	ρ	$\varepsilon_0/\varepsilon_r$
19	C-9.5	7.98	0.177	9088	22.733
	RC-9.5	8.59	0.173	11577	23.015

33	C-9.5	13.86	0.139	133015	26.678
	RC-9.5	14.92	0.134	236165	27.757
48	C-9.5	20.16	0.108	6949415	35.894
	RC-9.5	21.70	0.101	22758867	39.531

Table 6-4 Regression parameters and results by Equation 6-1

	Material	β_1	R-square
FL	C-9.5	0.671	0.866
	RC-9.5	1.441	0.835
ML ($(\tau_{a\theta})_{max}$=15kPa)	C-9.5	1.858	0.951
ML($(\tau_{a\theta})_{max}$=30kPa)	C-9.5	3.893	0.939
	RC-9.5	3.718	0.896

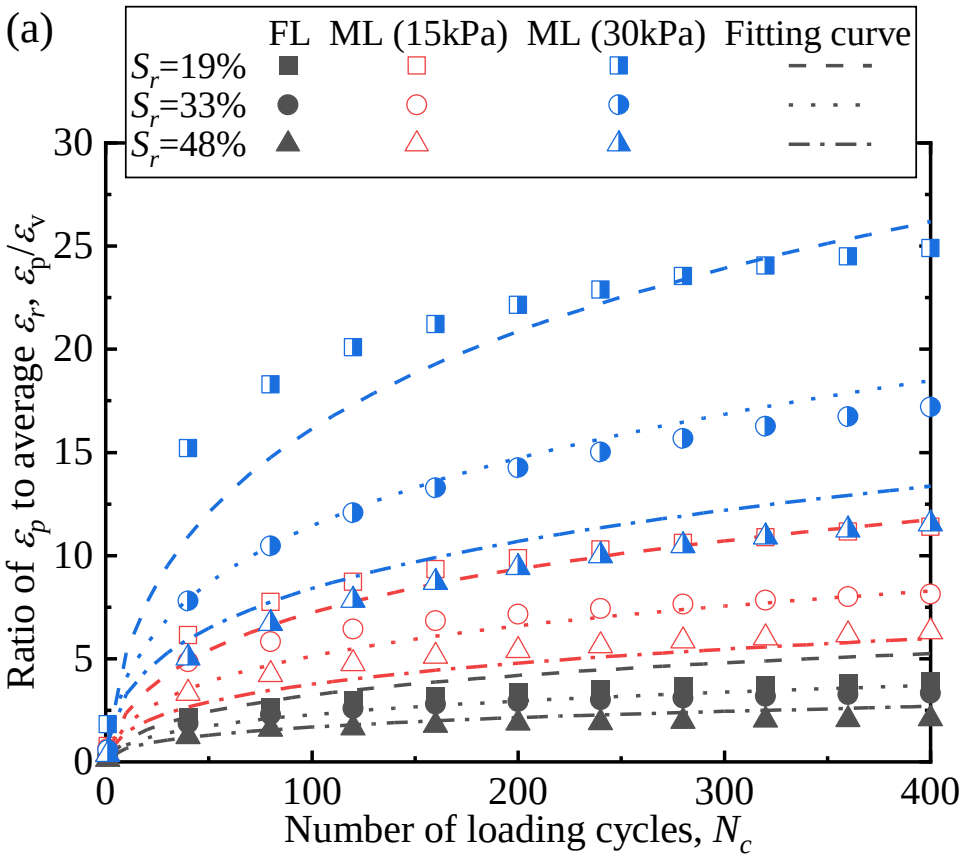
According to Ishikawa et al. (2011), the effect of PSAR on permanent strain can be reflected by a parameter $(R_s)_{ave}$. $(R_s)_{ave}$ means the average ratio of axial strain between specimens with and without PSAR, which can be expressed as Equation 6-2:

$$(R_s)_{ave} = exp\left(A\frac{(\tau_{a\theta})_{max}}{(\sigma_a)_{max}}\right) \tag{6-2}$$

where $(\tau_{a\theta})_{max}$ is the maximum applied shear stress, $(\sigma_a)_{max}$ is the maximum applied axial stress, and A is a regression parameter. By combining Equation 6-2 and Equation 6-1, the following form of fitting equation considering the effect of shear stress level can be obtained as shown in Equation 6-3:

$$\frac{\varepsilon_p}{\varepsilon_v} = \beta_{s1}k_{s1}\left(\frac{\varepsilon_0}{\varepsilon_r}\right)exp\left(A\frac{(\tau_{a\theta})_{max}}{(\sigma_a)_{max}} - \left(\frac{\rho}{N_c}\right)^{\beta}\right) \tag{6-3}$$

In Equation 6-3, the effect of PSAR can be incorporated into the prediction of $\varepsilon_p/\varepsilon_v$ in addition to the effect of water content. The fitting results of C-9.5 and RC-9.5 by Equation 6-3 are shown in Figure 6-11 (a) and (b), respectively. Table 6-5 shows the regression parameters and the R-square values. It can be found that the regression results fit well with the data, and the R-square values of both C-9.5 and RC-9.5 are higher than when using Equation 6-1. Therefore, it seems reasonable to conclude that Equation 6-3 can be employed for the prediction of permanent strain for unbound aggregate materials with different water content under PSAR conditions. In this way, the relationship between resilient strain, permanent strain, and allowable loading number for rutting can be established.


(a)
FL
ML (15kPa)
ML (30kPa)
Fitting curve
S_r=19%
S_r=33%
S_r=48%
Ratio of ε_p to average ε_r, $\varepsilon_p/\varepsilon_v$
Number of loading cycles, N_c
0
5
10
15
20
25
30
0
100
200
300
400

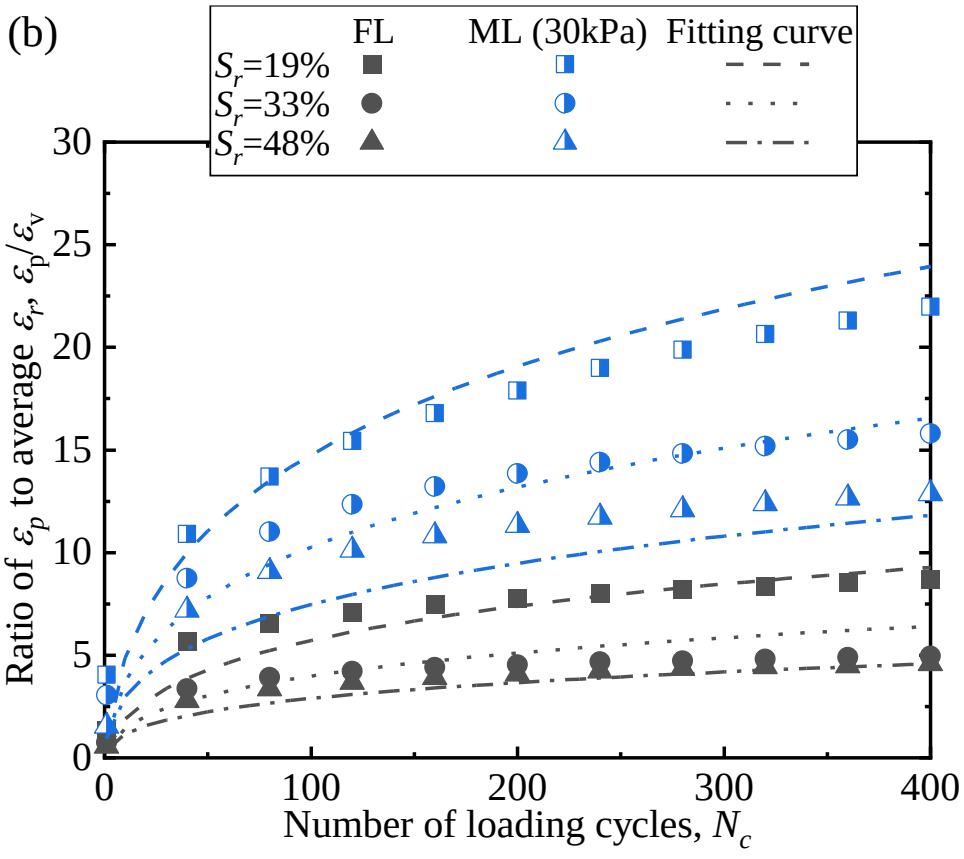

(b)
FL
ML (30kPa)
Fitting curve
S_r=19%
S_r=33%
S_r=48%
Ratio of ε_p to average ε_r, $\varepsilon_p/\varepsilon_v$
Number of loading cycles, N_c
0
5
10
15
20
25
30
0
100
200
300
400

Figure 6-11 Ratio of permanent strain to resilient strain fitted by Equation 6-3: (a) C-9.5, (b) RC-9.5

Table 6-5 Regression parameters and results by Equation 6-3

Material	A	β_1	R-square
C-9.5	6.114	0.786	0.972
RC-9.5	3.609	1.441	0.955

6.3 Summary

This chapter evaluated the effect of PSAR on the resilient axial strain and permanent axial strain of two types of unbound aggregate material. It is noted that since the PSAR is closely related to the cyclic shear stress caused by the moving wheel loads in the multi-ring shear tests, the existence of PSAR corresponds to whether the shear stress exists or not, and that the maximum shear stress during a loading cycle affects the rotational angle of PSAR. Then, the test results with and without considering PSAR are compared, and fitted by the MEPDG model to verify and discuss the applicability in predicting the permanent strain under the effect of PSAR.

1. The resilient axial strain tends to be constant with the increment in the number of loading cycles, and the converged value increases with the increment of the water content, but does not change or slightly increase under the effect of PSAR.
2. The increasing rate of the permanent strain tends to converge to a constant at the end of the test, and the converged value increases with the increment of the water content and the shear stress.
3. The MEPDG model shows relatively good applicability in the prediction of the permanent strain, while the PSAR may increase the permanent strain and strongly affect the local calibration coefficient β_1.
4. For a more precise prediction of the permanent strain under PSAR conditions, it is necessary to incorporate the $(R_s)_{ave}$ into the original MEPDG model in order to simultaneously consider the resilient strain and PSAR. Compared with the current design guide, the predicted N_{fs} by the MEPDG model with consideration of PSAR decreases by 86.86% on average, which is much closer to the actual failure number.

7 FINDINGS AND ASSIGNMENTS

7.1 Findings

In this study, M_r tests under different moisture, wheel loading, and temperature conditions are conducted to investigate the effect of complex environmental conditions on the resilient modulus of both non-frost-susceptible and frost-susceptible subgrade soils. Furthermore, the effect of PSAR on the resilient axial strain and permanent axial strain of two types of unbound aggregate material is also evaluated. Based on the test results and discussions from this study, the following findings can be mainly drawn:

(1) M_r affected by complex climatic and wheel loading conditions:

- Generally, M_r increases with the increment of the confining pressure and the matric suction but decreases with the increment of the deviator stress and can be captured by the climatic Ng model. Although the degrees of saturation under the same matric suction differ along the drying and wetting paths, the measured resilient moduli are very close. That is, the resilient moduli along the drying and wetting paths can be fitted together for the same matric suction for most of the unsaturated conditions during the normal season unsaturated conditions during the normal season because the range of changes in matric suction is relatively small. However, since the moisture content also affects the strength of unsaturated soils, especially when the moisture content is significantly low, the modified Ng model may show better accuracy.
- During the normal season, the effect of wheel load may differ in different materials. The UW test results indicate that the wheel loading process may increase the M_r of the Tomakomai soil by 3.74% ~ 7.47% but decrease that of the Toyoura sand by 9.30% ~ 18.86%. In the case of Tomakomai soil, the decrement of the resilient strain increases the soil strength, which leads to an increment in the M_r. However, the resilient strain of Toyoura sand during the wheel loading process increases, which indicates that the wheel loads lead to a decrement in the M_r. Furthermore, since Toyoura sand is much more poorly graded, the soil skeleton may be disturbed by the wheel loading process due to the lack of fine fraction, which leads to a decrement of the M_r.

- During the thawing season, since although the matric suction is the same, different moisture contents will cause different freeze-thaw effects, the M_r along the drying and wetting paths are significantly different. The freeze-thaw process generally decreases the M_r by 0.50% ~ 26.35% in the case of Tomakomai soil and by 0.28% ~ 18.78% in the case of Toyoura sand, which is obvious because the formation of ice disturbs the original soil skeleton. Furthermore, the effect of freeze-thaw action on resilient modulus is positively correlated with moisture content. Although the frost heave differs a lot, the average decreasing rates of M_r of Toyoura sand and Tomakomai soil are 6.8% and 5.6%, respectively, with no significant difference. It also indicates that the greatest harm of the freeze-thaw action to frost-susceptible soils is the structural damage to the pavement due to the significant frost heave.
- The effect of combinations of freeze-thaw action and wheel load is more complicated, which comprehensively depends on the wheel loading sequence and material properties. On the one hand, the results of FTW tests are close to the UW tests. The possible reason is similar to the UW test: the consolidation plays a leading role in increasing the resilient modulus after freeze-thaw in the case of Tomakomai soil, but the disturbance of the soil skeleton plays a leading role in decreasing the resilient modulus in the case of Toyoura sand. On the other hand, the results of FWT and FT tests are similar. It can be inferred that the effect of the wheel loading process during the frozen season may be minimal because of the extremely high stiffness of the soil compared to normal seasons due to the freezing of water. Therefore, using the same predicting parameters as the UW tests for FTW tests and the same predicting parameters as the FT tests for FWT tests is reasonable.

(2) M_r affected by suctions stress:

- Three different χ estimation models respectively based on normalized volumetric water content, effective degree of saturation, and suction ratio are employed to determine the χ values. All the estimated results indicate that the χ and σ_s are significantly affected by the degree of saturation. Furthermore, since the degree of saturation differs along different drying and wetting paths even if the suction is the same, the M_r also differs along different drying and wetting paths.
- The existing M_r predictive models considering Bishop's effective stress rarely discuss their applicability to the wetting path of SWCC, and there are also some disputes about the factors in the equations or the determination method of χ. Some

modified models are obtained by incorporating χ into the MEPDG-based M_r predictive models in this study. By using some χ estimation models, the χ values are determined by the degree of saturation or suction ratio and further combined with the predictive models to compare the applicability and fitting efficiency of different χ estimation models and M_r predictive models.

- The M_r obtained from the U tests for both Toyoura sand and Tomakomai soil are divided into the fitting group and verification group to improve the fitting efficiency and verify the validity and reliability. The M_r results along the drying path are used as the fitting group to obtain the fitting parameters, and the M_r results along the wetting path are used as the verification group to verify the validity and reliability of the fitting. For the χ estimation models, the Vanapalli model and K&K model both show high fitting accuracy compared to the Karube model because the relationship between χ and S_r was proved to be nonlinear. On the other hand, the modified Ng model shows significantly higher accuracy in all cases than the other two models by vertically comparing the M_r predictive models. Therefore, the modified Ng model combined with the K&K or Vanapalli model has the best fit for the MR tests and has potential value in predicting the M_r of subgrade soil under different moisture conditions.

(3) Resilient and permanent strains in rutting affected by PSAR:

- In multi-ring shear tests, the resilient axial strain tends to be constant with the increment in the number of loading cycles, and the converged value increases with the increment of the water content but does not change or slightly increase under the effect of PSAR.
- The increasing rate of the permanent strain tends to converge to a constant at the end of the test, and the converged value increases with the increment of the water content and the shear stress.
- The MEPDG model shows relatively good applicability in the prediction of the permanent strain, while the PSAR may increase the permanent strain and strongly affect the local calibration coefficient β_1.
- For a more precise prediction of the permanent strain under PSAR conditions, it is necessary to incorporate the $(R_s)_{ave}$ into the original MEPDG model in order to simultaneously consider the resilient strain and PSAR. Compared with the current

design guide, the predicted N_{fs} by the MEPDG model with consideration of PSAR decreases by 86.86% on average, which is much closer to the actual failure number.

Finally, by incorporating the M_r predictive model with consideration of different moisture, temperature, and wheel loading conditions, and further incorporating the effect of PSAR on permanent strain, this study contributes to improving the current pavement design guide.

7.2 Future Assignments

- This study examined the effects of complex climatic and wheel load conditions on resilient modulus and completed some gaps in the dynamic mechanical properties of subgrade soil in cold regions on the fatigue life of road pavement. However, this study only considers the single freeze-thaw action, that is, the tests in this study only experience one freeze-thaw cycle. To approach field conditions more, further studies on the effect of multiple freeze-thaw actions are required.
- This study examined the resilient moduli of two types of sandy soils under different drying and wetting paths of SWCCs and fitted them with some predictive models. However, the difference of M_r between the drying and wetting paths is not significant because of the relatively large particle sizes. To investigate the effect of suction hysteresis on M_r more in-depth, further studies on different drying and wetting paths and more soil types are required.
- This study examined the resilient and permanent strains in rutting of two types of crusher-run materials under different water contents and PSAR. However, the effect of freeze-thaw action and its interaction with water contents and PSAR is not considered. To reflect the climatic effect in cold regions in rutting failure criterion, further studies on the effect of freeze-thaw action on rutting with consideration of PSAR are required.

LIST OF REFERENCES

[1] AASHTO. 1986. AASHTO Guide for Design of Pavement Structures. AASHTO, Washington, D.C.

[2] AASHTO. 2017. Standard method of test for determining the resilient modulus of soils and aggregate materials. AASHTO, Washington, D.C., USA.

[3] AASHTO. 2020. Mechanistic-empirical pavement design guide: A manual of practice. 3rd ed. AASHTO, USA.

[4] Alowaisy, A., Yasufuku, N., Ishikura, R., Hatakeyama, M., and Kyono, S. 2020. Continuous pressurization method for a rapid determination of the soil water characteristics curve for remolded and undisturbed cohesionless soils [Article]. Soils and Foundations, 60(3): 634-647. doi:10.1016/j.sandf.2020.03.014.

[5] Arthur, J.R.F., C., J.I.R.d., Dunstan, T., and Chua, K.S. 1980. Principal Stress Rotation: A Missing Parameter. Journal of the Geotechnical Engineering Division, 106(4): 419-433. doi:10.1061/AJGEB6.0000946.

[6] Asphalt Institute. 1982. Research and Development of Asphalt Institute's Thickness Design Manual. 9th ed. Asphalt Institute, College Park, Md., USA.

[7] ASTM. 2017. Standard practice for classification of soils for engineering purposes (unified soil classification system). ASTM Int'l.

[8] Berg, R.L., Bigl, S.R., Stark, J.A., and Durell, G.D. 1996. Resilient Modulus Testing of Materials from Mn/Road, Phase 1 [Tech Report]. doi:https://doi.org/10.21949/1404573.

[9] Bishop, A.W. 1959. The Principle of Effective Stress. Teknisk Ukeblad, 39: 859-863.

[10] Bishop, A.W., and Blight, G.E. 1963. Some Aspects of Effective Stress in Saturated and Partly Saturated Soils. Geotechnique, 13(3): 177-197. doi:10.1680/geot.1963.13.3.177.

[11] Brown, S. 1996. Soil mechanics in pavement engineering [Review]. Geotechnique, 46(3): 383-425. doi:10.1680/geot.1996.46.3.383.

[12] Chow, L., Mishra, D., and Tutumluer, E. 2014. Framework for Development of an Improved Unbound Aggregate Base Rutting Model for Mechanistic-Empirical Pavement Design [Article]. Transportation Research Record,(2401): 11-21. doi:10.3141/2401-02.

[13] Cole, D.M., Irwin, L.H., and Johnson, T.C. 1981. EFFECT OF FREEZING AND THAWING ON RESILIENT MODULUS OF A GRANULAR SOIL EXHIBITING NONLINEAR BEHAVIOR. Transportation Research Record.

[14] Dareeju, B., Gallage, C., Ishikawa, T., and Dhanasekar, M. 2017. Effects of principal stress axis rotation on cyclic deformation characteristics of rail track subgrade materials. Soils and Foundations, 57(3): 423-438. doi:https://doi.org/10.1016/j.sandf.2017.05.009.

[15] Elkady, T., Al-Mahbashi, A., and Al-Shamrani, M. 2017. Effect of Moisture Hysteresis on the Resilient Modulus of Lime-Treated Expansive Clay [Article]. Journal of Testing and Evaluation, 45(6): 2039-2049. doi:10.1520/JTE20160225.

[16] Fredlund, D.G., Rahardjo, H., and Fredlund, M.D. 2012. Unsaturated soil mechanics in engineering practice. John Wiley & Sons, Hoboken, N.J.

[17] Garven, E.A., and Vanapalli, S.K. Evaluation of Empirical Procedures for Predicting the Shear Strength of Unsaturated Soils. *In* Fourth International Conference on Unsaturated Soils. Carefree, Arizona, USA 2006. American Society of Civil Engineers. pp. 2570-2592.

[18] Gupta, S., Ranaivoson, A., Edil, T., Benson, C., and Sawangsuriya, A. 2007. Pavement design using unsaturated soil technology. M.D.o. Transportation, St. Paul, Minnesota.

[19] Han, Z., and Vanapalli, S. 2016. State-of-the-Art: Prediction of Resilient Modulus of Unsaturated Subgrade Soils [Article]. International Journal of Geomechanics, 16(4). doi:10.1061/(ASCE)GM.1943-5622.0000631.

[20] Hatakeyama, M., Kyono, S., and Kawahara, T. 2015. Development of Water Retention Test Apparatus According to The Continuous Pressurization Method. Oyo technical report,(34): 23-54. Available from https://cir.nii.ac.jp/crid/1523669555973608064 [accessed.

[21] Heath, A., Pestana, J., Harvey, J., and Bejerano, M. 2004. Normalizing behaviour of unsaturated granular pavement materials [Article]. Journal of Geotechnical and Geoenvironmental Engineering, 130(9): 896-904. doi:10.1061/(ASCE)1090-0241(2004)130:9(896).

[22] Hilf, J.W. 1956. AN INVESTIGATION OF PORE-WATER PRESSURE IN COMPACTED COHESIVE SOILS. Ph.D., University of Colorado at Boulder, United States -- Colorado.

[23] Inam, A., Ishikawa, T., and Miura, S. 2012. Effect of principal stress axis rotation on cyclic plastic deformation characteristics of unsaturated base course material [Article]. Soils and Foundations, 52(3): 465-480. doi:10.1016/j.sandf.2012.05.006.

[24] Ishikawa, T., Miura, S., and Sekine, E. Development and Performance Evaluation of Multi-Ring Shear Apparatus. *In* Proc., International Workshop on Geotechnical Aspects and Processed Material. 2007. *Edited by* A.G. Correia and Y. Momoya and F. Tatsuoka. pp. 53-64.

[25] Ishikawa, T., Sekine, E., and Miura, S. 2011. Cyclic deformation of granular material subjected to moving-wheel loads [Article]. Canadian Geotechnical Journal, 48(5): 691-703. doi:10.1139/T10-099.

[26] Ishikawa, T., Dareeju, B., Gallage, C., and Tianshu, L. 2021. Resilient Deformation Characteristics of Unsaturated Subgrade Materials of Rail Tracks under Cyclic Moving Wheel Loads. The Geotechnical Engineering Journal of the SEAGS & AGSSEA, 52(4): 23-32. doi:https://doi.nrct.go.th//ListDoi/listDetail?Resolve_DOI=10.14456/seagj.2021.4.

[27] Ishikawa, T., Lin, T., Kawabata, S., Kameyama, S., and Tokoro, T. 2019. Effect evaluation of freeze-thaw on resilient modulus of unsaturated granular base course material in pavement [Article]. Transportation Geotechnics, 21. doi:10.1016/j.trgeo.2019.100284.

[28] Japan Road Association. 2006. Pavement Design Manual. Maruzen Publishing, Tokyo, Japan.

[29] Japan Road Association. 2019. Handbook for asphalt pavement. Maruzen Publishing, Tokyo, Japan.

[30] Japanese Geotechnical Society. 2018. Laboratory Testing Standards of Geomaterials. Maruzen Publishing, Tokyo, Japan.

[31] Johnson, T.C., Cole, D.M., Chamberlain, E.J., United States. Army. Corps of Engineers. Directorate of Military, C., and Cold Regions Research and Engineering, L. 1978. Influence of Freezing and Thawing on the Resilient Properties of a Silt Soil Beneath an Asphalt Concrete Pavement. CRREL report. The Laboratory.

[32] Karube, D., Kato, S., Hamada, K., and Honda, M. 1996. The Relationship Between the Mechanical Behavior and the State of Porewater in Unsaturated Soil. Doboku Gakkai Ronbunshu, 535: 83-92. doi:10.2208/jscej.1996.535_83.

[33] Kato, S., Hatakeyama, M., Abe, H., Kim, B., and Takeshita, Y. Measurement of Soil-Water Characteristic Curve with a continuous pressurization method. *In* Unsaturated Soil Mechanics-from Theory to Practice: Proceedings of the 6th Asia Pacific Conference on Unsaturated Soils (Guilin, China, 23-26 October 2015). 2015. CRC Press. p. 379.

[34] Khalili, N., and Khabbaz, M. 1998. A unique relationship for chi for the determination of the shear strength of unsaturated soils [Article]. Geotechnique, 48(5): 681-687. doi:10.1680/geot.1998.48.5.681.

[35] Khoury, C., Khoury, N., and Miller, G. 2011. Effect of Cyclic Suction History (Hydraulic Hysteresis) on Resilient Modulus of Unsaturated Fine-Grained Soil [Article]. Transportation Research Record,(2232): 68-75. doi:10.3141/2232-07.

[36] Khoury, N., Brooks, R., and Khoury, C. 2009. Environmental influences on the engineering behavior of unsaturated undisturbed subgrade soils: effect of soil suctions on

resilient modulus. International Journal of Geotechnical Engineering, 3(2): 303-311. doi:10.3328/IJGE.2009.03.02.303-311.

[37] Kim, B., Hatakeyama, M., Park, S., Park, H., Takeshita, Y., and Kato, S. 2021. Assessment of Water Retention Test by Continuous Pressurization Method [Article]. Geotechnical Testing Journal, 44(2): 274-289. doi:10.1520/GTJ20190410.

[38] Kim, D., and Kim, J. 2007. Resilient behavior of compacted subgrade soils under the repeated triaxial test [Article]. Construction and Building Materials, 21(7): 1470-1479. doi:10.1016/j.conbuildmat.2006.07.006.

[39] Kishikawa, T., Otgonjargal, D., Kawaguchi, T., Nakamura, D., and Yamashita, S. Influence of freeze-thaw on stress propagation in the ground. *In* 57th Technical Report of the Annual Meeting of the JGS Hokkaido Branch. Kitami, Japan 2017. pp. 27-34.

[40] Korkiala-Tanttu, L. 2009. Verification of rutting calculation for unbound road materials. Proceedings of the Institution of Civil Engineers - Transport, 162(2): 107-114. doi:10.1680/tran.2009.162.2.107.

[41] Lekarp, F., Isacsson, U., and Dawson, A. 2000a. State of the art. I: Resilient response of unbound aggregates [Article]. Journal of Transportation Engineering-Asce, 126(1): 66-75. doi:10.1061/(ASCE)0733-947X(2000)126:1(66).

[42] Lekarp, F., Isacsson, U., and Dawson, A. 2000b. State of the art. II: Permanent strain response of unbound aggregates [Article]. Journal of Transportation Engineering-Asce, 126(1): 76-83. doi:10.1061/(ASCE)0733-947X(2000)126:1(76).

[43] Leuther, F., and Schlüter, S. 2021. Impact of freeze–thaw cycles on soil structure and soil hydraulic properties. SOIL, 7(1): 179-191. doi:10.5194/soil-7-179-2021.

[44] Li, D., and Selig, E. 1994. RESILIENT MODULUS FOR FINE-GRAINED SUBGRADE SOILS [Article]. Journal of Geotechnical Engineering-Asce, 120(6): 939-957. doi:10.1061/(ASCE)0733-9410(1994)120:6(939).

[45] Liang, R., Rabab'ah, S., and Khasawneh, M. 2008. Predicting moisture-dependent resilient modulus of cohesive soils using soil suction concept [Article]. Journal of Transportation Engineering, 134(1): 34-40. doi:10.1061/(ASCE)0733-947X(2008)134:1(34).

[46] Lin, T., Ishikawa, T., and Luo, B. 2019. Applicability of Modified University of Illinois at Urbana-Champaign Model for Unbound Aggregate Material with Different Water Content [Article]. Transportation Research Record, 2673(3): 439-449. doi:10.1177/0361198119827530.

[47] Lin, T., Ishikawa, T., Maruyama, K., and Tokoro, T. 2021. Pavement design method in Japan with consideration of climate effect and principal stress axis rotation. Transportation Geotechnics, 28. doi:10.1016/j.trgeo.2021.100552.

[48] Lin, T., Ishikawa, T., Yang, J., and Tokoro, T. 2022. Evaluation of climate effect on resilient modulus of granular subgrade material [Article]. Cold Regions Science and Technology, 194. doi:10.1016/j.coldregions.2021.103452.

[49] Lu, N., and Griffiths, D. 2004. Profiles of steady-state suction stress in unsaturated soils [Article]. Journal of Geotechnical and Geoenvironmental Engineering, 130(10): 1063-1076. doi:10.1061/(ASCE)1090-0241(2004)130:10(1063).

[50] Lu, N., and Likos, W.J. 2004. Unsaturated soil mechanics. J. Wiley, Hoboken, N.J.

[51] Lu, N., and Likos, W. 2006. Suction stress characteristic curve for unsaturated soil [Article]. Journal of Geotechnical and Geoenvironmental Engineering, 132(2): 131-142. doi:10.1061/(ASCE)1090-0241(2006)132:2(131).

[52] Lytton, R.L. Foundations and pavements on unsaturated soils. *In* Proceedings of the 1st International Conference on Unsaturated Soils, UNSAT 95. Paris, France, 1996 1995. pp. 1201-1220.

[53] Maina, J., and Matsui, K. 2004. Developing software for elastic analysis of pavement structure responses to vertical and horizontal surface loadings [Article|Proceedings Paper]. Transportation Research Record, 1896(1): 107-118. doi:https://doi.org/10.3141/1896-11.

[54] NCHRP. 2004. Final report. NCHRP.

[55] Ng, C., Zhou, C., Yuan, Q., and Xu, J. 2013. Resilient modulus of unsaturated subgrade soil: experimental and theoretical investigations [Article]. Canadian Geotechnical Journal, 50(2): 223-232. doi:10.1139/cgj-2012-0052.

[56] Oh, J., Fernando, E., Holzschuher, C., and Horhota, D. 2012. Comparison of resilient modulus values for Florida flexible mechanistic-empirical pavement design [Article]. International Journal of Pavement Engineering, 13(5): 472-484. doi:10.1080/10298436.2011.633170.

[57] Sahin, H., Gu, F., Tong, Y., Luo, R., and Lytton, R. 2013. Unsaturated soil mechanics in the design and performance of pavements. Advances in Unsaturated Soils - Proceedings of the 1st Pan-American Conference on Unsaturated Soils, PanAmUNSAT 2013: 87-99. doi:10.1201/b14393-8.

[58] Seed, H.B., Chan, C.K., and Monismith, C.L. Effects of repeated loading on the strength and deformation of compacted clay. *In* Thirty-Fourth Annual Meeting of the Highway Research Board. Washington, D.C. 1955. Highway Research Board. pp. 541-558.

[59] Seto, S., Ishikawa, T., Dareeju, B., and Gallage, C. Effect evaluation of cyclic plastic deformation of unsaturated railway roadbed under moving wheel loading. *In* 57th Technical Report of the Annual Meeting of the JGS Hokkaido Branch. Kitami, Japan 2017. pp. 201-210.

[60] Simonsen, E., and Isacsson, U. 2001. Soil behavior during freezing and thawing using variable and constant confining pressure triaxial tests [Article]. Canadian Geotechnical Journal, 38(4): 863-875. doi:10.1139/t01-007.

[61] Simonsen, E., Janoo, V., and Isacsson, U. 2002. Resilient properties of unbound road materials during seasonal frost conditions [Article]. Journal of Cold Regions Engineering, 16(1): 28-50. doi:10.1061/(ASCE)0887-381X(2002)16:1(28).

[62] Starkloff, T., Larsbo, M., Stolte, J., Hessel, R., and Ritsema, C. 2017. Quantifying the impact of a succession of freezing-thawing cycles on the pore network of a silty clay loam and a loamy sand topsoil using X-ray tomography [Article]. Catena, 156: 365-374. doi:10.1016/j.catena.2017.04.026.

[63] Tseng, K.H., and Lytton, R.L. Prediction of Permanent Deformation in Flexible Pavement Materials. *In* Implication of Aggregates in the Design, Construction, and Performance of Flexible Pavements. 1989. pp. 154–172.

[64] Vanapalli, S., Fredlund, D., Pufahl, D., and Clifton, A. 1996. Model for the prediction of shear strength with respect to soil suction [Article]. Canadian Geotechnical Journal, 33(3): 379-392. doi:10.1139/t96-060.

[65] VanGenuchten, M. 1980. A Closed-form equation for predicting the hydraulic conductivity of unsaturated soils [Article]. Soil Science Society of America Journal, 44(5): 892-898. doi:10.2136/sssaj1980.03615995004400050002x.

[66] Wang, S., Yang, P., and Yang, Z. 2018. Characterization of freeze-thaw effects within clay by 3D X-ray Computed Tomography [Article]. Cold Regions Science and Technology, 148: 13-21. doi:10.1016/j.coldregions.2018.01.001.

[67] Yang, S., Huang, W., Tai, Y., and TRB. 2005. Variation of resilient modulus with soil suction for compacted subgrade soils [Article|Proceedings Paper]. Geology and Properties of Earth Materials 2005,(1913): 99-106. doi:10.3141/1913-10.

[68] Yasuoka, T., Ishikawa, T., Wu, Y., Tokoro, T., Maruyama, K., and Ueno, C. Proposal of installation method of geosynthetics drainage material for frost heave depression of road pavement. *In* Japanese Geotechnical Society Hokkaido Branch Technical Report Collection. Hokkaido, Japan 2021. pp. 155-164.

LIST OF NOTATIONS

Description	Symbol
Resilient modulus	M_r
Allowable loading number of equivalent 49-kN wheel loads against cracking calculated in current Japanese design guide	N_{fa}
Allowable loading number of equivalent 49-kN wheel loads against rutting calculated in current Japanese design guide	N_{fs}
The compensation rates for AI rutting failure criteria based on the actual situation of Japanese pavement	β_{s1}, β_{s2}
The compensation rates for AI cracking failure criteria based on the actual situation of Japanese pavement	β_{a1}, β_{a2}, β_{a3}
The asphalt mixture parameter	C_a
Correction factor, which relates to the thickness of asphalt mixture	K_a
Thickness of asphalt mixture	H_1
Thickness of base layer	H_2
The compressive strain on the top surface of the subgrade layer	ε_a
The tensile strain on the lower surface of the asphalt mixture layer	ε_t
Poisson's ratio	v
Elastic moduli of asphalt mixture layer	E_1
Elastic moduli of base layer	E_2
Elastic moduli of subgrade layer	E_3
The adjusting parameter used in AI model	β_m
Regression parameters used in M_r predictive models	k_1, k_2, k_3, k_4
Bulk stress	θ
Major principal stress	σ_1
Intermediate principal stress	σ_2
Minor principal stress	σ_3
Atmospheric pressure	p_a

Octahedral stress	τ_{oct}
Resilient modulus at optimum moisture content	M_{ropt}
Degree of saturation in decimals	S
Degree of saturation at optimum moisture content in decimals	S_{opt}
Minimum of *log* (M_r/M_{ropt})	a
Maximum of *log* (M_r/M_{ropt})	b
Regression constant	k_m
Net mean stress	σ_{net}
Matric suction	ψ
Climatic factor	F_{clim}
Permanent or plastic deformation for the base course or subgrade layer	$\Delta_{p(soil)}$
Number of axle-loading cycles	N_c
Intercept determined from laboratory repeated load permanent deformation tests	ε_0
Resilient strain imposed in laboratory repeated load permanent deformation tests to obtain material properties ε_0, β, and ρ	ε_r
Average vertical resilient or elastic strain in the base course or subgrade layer	ε_v
Thickness of the unbound base course or subgrade layer	h_{soil}
Global calibration coefficients	k_{s1}
Local calibration constant for the rutting in the unbound layers	β_1
Regression constants	a_1, a_9, b_1, b_9
Water content	W_c
Average ratio between the axial strains with and without PSAR	$(R_S)_{ave}$
Permanent axial strain	ε_p
Applied deviator stress	σ_d
Mobilized shearing resistance acting on failure plane	τ_f
Normal stress acting on failure plane	σ_f
Applied axial stress	σ_a

Applied shear stress	$\tau_{a\theta}$
Available shear strength obtained through Mohr-Coulomb failure criteria	τ_{max}
Regression parameters	A, B, C, D, E
Maximum deviator stress applied in M_r tests	q_{max}
Contact deviator stress to maintain positive contact between the specimen cap and the specimen	q_{cont}
Difference between q_{max} and q_{cont}	q_{cyclic}
Confining pressure	σ_c
Degree of saturation	S_r
R-square value	R^2
Elapsed time	t
Water drainage	ΔV_m
Effective stress	σ'
Total stress	σ
Pore air pressure	u_a
Pore water pressure	u_w
Coefficient of effective stress	χ
Normalized volumetric water content	Θ
Volumetric water content	θ_w
Volumetric water content at a saturation of 100%	θ_s
Fitting parameter	κ
Plastic index	I_p
Suction stress	σ_s
Residual volumetric water content	θ_r
Residual degree of saturation	S_0
Air entry value of the SWCC	$(u_a\text{-}u_w)_b$
R-square of fitting group	R^2_{fit}

Mean square error of fitting group	MSE_{fit}
R-square of verification group	R^2_{veri}
Mean square error of verification group	MSE_{veri}
Dry density	ρ_d
Maximum applied axial stress	$(\sigma_a)_{max}$
Maximum applied shear stress	$(\tau_{a\theta})_{max}$
Increasing rate of ε_p	δ
Regression parameter	A